SCUOLA
NORMALE
SUPERIORE

Classe di Scienze

Corso di perfezionamento in
Nanoscienze

XXXVI ciclo

Energy transfer in individual high aspect-ratio nanostructures via all-optical techniques

Settore Scientifico Disciplinare FIS/03

Candidata
dr.ssa Alessia COLOSIMO

Relatori

Prof. Francesco Rossella

Prof. Francesco Banfi

Prof. Natalia Del Fatti

Supervisione interna

Prof. Fabio BELTRAM

SCUOLA
NORMALE
SUPERIORE

Anno accademico 2024/2025

SCUOLA NORMALE SUPERIORE

UNIVERSITÉ DE LYON

Lyon 1

DOCTORAL THESIS

Energy transfer in individual high aspect-ratio nanostructures via all-optical techniques

---

Candidate:

Alessia Colosimo

Thesis supervisors:

Prof. Francesco Rossella

Prof. Francesco Banfi

Prof. Fabio Beltram

Prof. Natalia Del Fatti

A thesis submitted in fulfillment of the requirements for the degree of Doctor of Philosophy in Nanoscience

Academic year 2024/2025

Abstract

High aspect-ratio nanostructures are catching the attention of the micro- and nano-science and technology community because of their potential in manifold applications, ranging from energy harvesting and sensing to nanoelectronics and optoelectronics. This is driving the development of dedicated synthesis techniques for nanostructures with different materials and shapes as well as innovative nanofabrication protocols for their integration into actual devices. Current research is steering to nanoscale energy transfer, both mechanical and thermal. In fact, knowledge of the mechanical properties is crucial to engineer any reliable nanostructure-based device, whereas its frequency response is at the core of mass sensing devices. Besides, understanding heat transport involving such nanostructures is key in view of their deployment in nanoelectronics, where heat management is among the limiting factors towards further device downscaling. The prominent aspect of nanoscale energy transfer stands in its characteristic ultrafast time and micro- to nano-length scales. Moreover, it involves small energy fluxes and is adversely perturbed by contact probes. These issues require devising appropriate ultrafast, low-perturbing and sensitive techniques applicable on the ultrashort time scales.

The thesis targets energy transfer (mechanical and thermal) within and out of individual nanostructures on the relevant time and length scales by means of all-optical microscopy, fulfilling the above-mentioned requirements. The work addresses the photo-thermo-mechanics of MoS_2 nanotubes and of InAs nanowires, to access the mechanical and/or thermal pathways within the system and/or from the system to its environment (i.e. targeting either isolated or substrate-supported nanostructures). Both linear and time-resolved all-optical techniques are implemented to investigate aspects of the energy dynamics. In a nutshell, the cascade of events of relevance here is as follows. First, the energy from a laser pulse is delivered to the system, the amount of energy absorbed by the sample being ruled by the optical absorption cross-section. Second, the absorbed energy triggers the mechanical and thermal transients within the nanostructure and is ultimately dissipated towards the environment. Measurements are performed on individual nanostructures, filtering out inhomogeneous broadening effects due to geometrical dispersion and enabling a one-to-one correlation between the nano-object's dimensions

and environment.

A nanofabrication protocol is developed to suspend single nanostructures over a trench while matching the requirements dictated by the microscopy setup. In order to address the role of the environment, two other configurations are investigated in which the nanostructure is supported on polymethyl methacrylate (PMMA), paradigmatic of soft insulating supports, and on a sapphire substrate, paradigmatic of hard, thermally conductive dielectrics.

Energy transfer is investigated in recently synthesized - individual multiwall MoS_2 nanotubes. Despite its relevance in view of any optical application, the MoS_2 nanotubes optical cross-sections (both absorption and scattering) are not known, thus hindering knowledge of the energy absorbed by the nanotube. To this aim, the single MoS_2 nanotube absolute extinction cross-section per unit length is experimentally retrieved over a wide range of wavelengths and for light polarizations both perpendicular and orthogonal to the nanotube main axis. Additionally, the impact of the nanotube diameters and its environment is investigated. Both analytical calculations and numerical simulations are implemented to disentangle the absorption and scattering contributions to the extinction cross-section. The mechanical properties of MoS_2 nanotubes are then investigated, allowing for the identification of their breathing and thickness modes. Knowledge of these modes periods, together with analytical modeling, allows accessing the thickness of the MoS_2 nanotube shell. The latter is found to be constant with respect to the nanotube external radius. This information could not be accessed with other techniques (TEM and μ-Raman), demonstrating time-resolved optical spectroscopy as an effective non-destructive tool, in this case yielding information on the nano-object morphology, namely a nanotube shell thickness of 16 nm.

Time-resolved ultrafast spectroscopy is also used to access the mechanics of and the thermal dynamics out of an individual InAs nanowire. The mechanical response of individual InAs nanowires is investigated, giving access to their breathing and longitudinal modes, rationalized both by analytical models and Finite Element Method simulations. Calculations, performed adopting the stiffness matrix theoretically proposed for wurtzite InAs nanowires grown along the [111] direction (bulk wurtzite InAs does not exist in nature), yield the correct (i.e. experimentally retrieved) radial and longitudinal eigenmodes and eigenvectors. The attenuation of the nanowire acoustic modes is also addressed. The extrinsic and intrinsic attenuation times are retrieved for the breathing mode in the hypersonic frequency range. The extrinsic dissipation channel prevails by far over the intrinsic one. The results of this study are significant not only for their scientific value but also for showcasing the potential of time-resolved nanoscopy as a non-destructive tool

for characterizing the mechanical behavior of nanoobjects at the individual level. On the thermal side, a novel method for analyzing heat dissipation out of the nanowires starting from time-resolved optical traces, affected by reproducibility issues, is devised. The extent of the nanowire-to-substrate contact correlates with the rate of heat dissipation out of the individual nanowire. These results widen the range of applicability of time-resolved optical techniques to non-destructive testing of a nano-object contact with its surroundings. The thermal conductance at the InAs-PMMA interface is also retrieved, its value being $G \sim 83$ MW/m$^2\cdot$ K.

There are two angles to this thesis. From a methodological perspective, it shows how static and ultrafast all-optical spectro-microscopy techniques may be exploited as an effective non-destructive nanometrology tool to inspect *individual* high aspect-ratio nanostructures. On the material side, it provides optical, mechanical and thermal properties of high aspect-ratio nanostructures composed of two emerging classes of nanomaterials: MoS_2 nanotubes and InAs nanowires. These stand at the foundation of a variety of potential applications ranging from optoelectronics to NEMS.

Résumé

Les nanostructures à rapport d'aspect élevé attirent l'attention de la communauté des micro- et nano-sciences et technologies en raison de leur potentiel dans de nombreuses applications, allant de la collecte d'énergie et de la détection à la nanoélectronique et à l'optoélectronique. Cela stimule le développement de techniques de synthèse dédiées pour des nanostructures avec différents matériaux et formes, ainsi que des protocoles de nanofabrication innovants pour leur intégration dans des dispositifs réels. La recherche actuelle s'oriente vers le transfert d'énergie à l'échelle nanométrique, tant mécanique que thermique. En effet, la connaissance des propriétés mécaniques est cruciale pour concevoir tout dispositif basé sur des nanostructures fiable, tandis que sa réponse en fréquence est au cœur des dispositifs de détection de masse. De plus, comprendre le transport de la chaleur impliquant de telles nanostructures est essentiel en vue de leur déploiement en nanoélectronique, où la gestion de la chaleur est l'un des facteurs limitants pour une réduction supplémentaire de la taille des dispositifs. L'aspect prédominant du transfert d'énergie à l'échelle nanométrique réside dans son temps caractéristique ultrarapide et ses échelles de longueur allant du micro au nano. De plus, il implique de faibles flux d'énergie et est perturbé de manière défavorable par des sondes de contact. Ces problèmes nécessitent la mise au point de techniques appropriées, ultrarapides, peu perturbatrices et sensibles, applicables sur des échelles de temps ultracourtes.

La thèse vise l'étude du transfert d'énergie (mécanique et thermique) à l'intérieur et à l'extérieur des nanostructures individuelles sur les échelles de temps et de longueur pertinentes, en utilisant la spectro-microscopie optique résolue en temps, répondant ainsi aux exigences mentionnées ci-dessus. Le travail aborde la photo-thermo-mécanique de nanotubes de MoS_2 et de nanofils d'InAs, afin d'explorer la mécanique et la thermiques au sein du système et/ou du système vers son environnement (notamment en ciblant soit des nanostructures isolées, soit des nanostructures supportées par un substrat). Des techniques entièrement optiques, à la fois linéaires et résolues dans le temps, sont mises en œuvre pour étudier les aspects de la dynamique énergétique. En résumé, la cascade d'événements pertinente ici est la suivante: tout d'abord, l'énergie d'une impulsion laser est délivrée au système, la quantité d'énergie absorbée par l'échantillon étant déterminée

par la section efficace d'absorption optique. Deuxièmement, l'énergie absorbée déclenche les transitoires mécaniques et thermiques au sein de la nanostructure et est finalement dissipée vers l'environnement. Les mesures sont effectuées sur des nanostructures individuelles, filtrant les effets d'élargissement inhomogène dus à la dispersion géométrique et permettant une corrélation directe entre les dimensions du nano-objet et son environnement.

Un protocole de nanofabrication est développé pour suspendre des nanostructures individuelles au-dessus d'une tranchée tout en respectant les exigences dictées par le dispositif de microscopie. Afin d'explorer le rôle de l'environnement, deux autres configurations sont étudiées dans lesquelles la nanostructure est supportée sur du polyméthacrylate de méthyle (PMMA), représentatif des supports isolants souples, et sur un substrat en saphir, représentatif des diélectriques durs et thermiquement conducteurs.

Le transfert d'énergie est étudié dans des nanotubes de MoS_2 multiparois récemment synthétisés. Malgré son importance pour toute application optique, les sections efficaces optiques des nanotubes de MoS_2 (à la fois pour l'absorption et la diffusion) ne sont pas connues, ce qui entrave la compréhension de l'énergie absorbée par le nanotube. À cette fin, la section efficace d'extinction absolue par unité de longueur d'un seul nanotube de MoS_2 est retrouvée expérimentalement sur une large gamme de longueurs d'onde et pour des polarizations de lumière à la fois perpendiculaires et orthogonales à l'axe principal du nanotube. De plus, l'impact des diamètres des nanotubes et de leur environnement est étudié. Des calculs analytiques et des simulations numériques sont mis en œuvre pour dissocier les contributions d'absorption et de diffusion à la section efficace d'extinction. Les propriétés mécaniques des nanotubes de MoS_2 sont ensuite étudiées, permettant d'identifier leurs modes de respiration et d'épaisseur. La connaissance des périodes de ces modes, associée à une modélisation analytique, permet d'accéder à l'épaisseur de la coque du nanotube de MoS_2. Cette dernière s'avère constante par rapport au rayon externe du nanotube. Cette information n'a pas pu être obtenue par d'autres techniques (TEM et μ-Raman), démontrant que la spectroscopie optique résolue dans le temps est un outil non destructif efficace, fournissant dans ce cas des informations sur la morphologie du nano-objet, à savoir une épaisseur de coque de nanotube de 16 nm.

La spectroscopie ultrarapide résolue dans le temps est également utilisée pour accéder à la mécanique et à la dynamique thermique d'un nanofil d'InAs individuel. La réponse mécanique des nanofils d'InAs individuels est étudiée, permettant d'accéder à leurs modes de respiration et longitudinaux, rationalisés à la fois par des modèles analytiques et des simulations par la méthode des éléments finis. Les calculs, réalisés en adoptant la matrice de rigidité théoriquement proposée pour les nanofils d'InAs en wurtzite croissant le

long de la direction [111] (le wurtzite d'InAs massif n'existe pas dans la nature), permettent de retrouver les modes propres et les vecteurs propres radiaux et et longitudinaux expérimentalement observés.

L'étude de l'atténuation des modes acoustiques des nanofils est également abordée. Les temps d'atténuation extrinsèques et intrinsèques sont déterminés pour le mode de respiration dans la plage de fréquences hypersoniques. Le canal de dissipation extrinsèque prévaut de loin sur le canal intrinsèque. Les résultats de cette étude sont significatifs non seulement pour leur valeur scientifique, mais également pour démontrer le potentiel de la nanoscopie résolue en temps comme outil non invasif pour étudier le comportement mécanique des nano-objets à l'échelle individuelle. Du côté thermique, une nouvelle méthode d'analyse de la dissipation de chaleur des nanofils, à partir de traces optiques résolues dans le temps et affectées par des problèmes de reproductibilité, est conçue. L'étendue du contact entre le nanofil et le substrat est corrélée au taux de dissipation de chaleur du nanofil individuel. Ces résultats élargissent le champ d'application des techniques optiques résolues dans le temps pour les tests non destructifs du contact d'un nanoobjet avec son environnement. Enfin, la conductance thermique à l'interface InAs-PMMA est également déterminée, sa valeur étant $G \sim 83$ MW/m$^2\cdot$ K.

Cette thèse aborde deux aspects. D'un point de vue méthodologique, elle montre comment les techniques de spectromicroscopie optique statique et ultrarapide peuvent être exploitées comme un outil de nanométrologie non destructif efficace pour inspecter des nanostructures individuelles à rapport d'aspect élevé. Sur le plan des matériaux, elle fournit des propriétés optiques, mécaniques et thermiques de nanostructures à rapport d'aspect élevé composées de deux classes émergentes de nanomatériaux : les nanotubes de MoS_2 et les nanofils d'InAs. Ces matériaux constituent la base d'une variété d'applications potentielles allant de l'optoélectronique aux NEMS.

Contents

List of Abbreviations

- NW: Nanowire
- NT: Nanotube
- InAs: Indium arsenide
- MoS_2: Molybdenum disulfide
- TBR: Thermal Boundary Resistance
- VdW: Van der Waals
- MD: Molecular Dynamics
- FEM: Finite Element Modeling
- SMS: Spatial Modulation Spectroscopy
- ES: Extinction Spectroscopy
- US: Ultrafast Time-Resolved Spectroscopy
- FWHM: Full Width Half Maximum
- VIS: Visible
- UV: Ultraviolet
- OPO: Optical Parametric Oscillator
- BBO: Barium beta-borate crystal
- SHG: Second-Harmonic Generation
- LIA: Lock-in Amplifier
- DMM: Digital Multimeter

- PD: Photodiode
- CBE: Chemical Beam Epitaxy
- VLS: Vapour Liquid Solid
- TBAs: tert-butylarsine
- TMIn: trimethylindium
- HR-TEM: High-Resolution Transmission Electron Microscope
- ED: Electron Diffraction
- SEM: Scanning Electron Microscope
- EBL: Electron Beam Lithography
- EHT: Electron High Tension
- PVD: Physical Vapour Deposition
- CAD: Computer-Aided Design
- ACE: Acetone
- IPA: Isopropyl alcohol
- PMMA: Polymethyl methacrylate
- WZ: Wurtzite
- ZB: Zincoblende
- ASOPS: Asynchronous Optical Sampling

Introduction

Nanoscale energy transfer is a key phenomenon in various scientific and technological disciplines. It plays a crucial role in nanotechnology and nanomaterials, particularly in engineering materials with tailored thermal and mechanical properties. It is of importance in fundamental science, e.g., affecting heat transfer in quantum systems [1–3]. Its applicative relevance extends from electronics and optoelectronics (where minimizing heat losses is essential) to nano-mechanic (design of micro- and nano-electromechanical systems, MEMS and NEMS), from energy harvesting technologies to medicine, where nanoscale energy transfer is critical for targeted treatments and diagnostics [4–8].

Nanoscale energy transfer is particularly relevant in the case of **semiconducting nanostructures**. The semiconductor industry has driven miniaturization [9], developing ever-smaller devices while reducing costs. As integrated circuits pack increasing numbers of devices on a single chip, the challenge of **heat dissipation** becomes more pressing. Efficient heat management is crucial for maintaining proper device operation, necessitating materials and strategies that can efficiently dissipate heat, providing thermal baths. Nanoscale heat management is thus one of the most urgent issues toward further device down-scaling.

On the **nano-mechanics** side, the development of nanoscale systems calls for a deeper understanding of their mechanical properties, which often differ significantly from their bulk counterparts. This knowledge is vital in the development of electromechanical systems, where the efficiency of mechanical vibrations must be optimized against energy dissipation [10–15], and for mass sensing devices, whose working principle relies on the resonance frequency of the nanostructure [16–19].

Molybdenum disulfide (MoS_2), a transition metal dichalcogenide that belongs to the class of **Van der Waals materials** [20], is a nanomaterial that has recently gained significant attention. As a 2D material with good charge carrier transport properties and tunable energy bandgap, and being relatively low-cost and abundant in nature, MoS_2 is relevant in the field of flexible devices for nanoelectronics [21] and energy applications [22], while its high wear resistance and mechanical strength and friction [23, 24] make it advantageous for prospective mechanical engineering applications. The technologically

relevant properties of MoS_2 have motivated research into the growth of nanotubes (NTs) [25, 26], and recent advancements have enabled the reliable synthesis of NTs in a pure crystal phase [27–29]. However, the current growth methods still lead to NTs with wide dispersion in diameters and morphology, thus calling for investigations to be performed on individual nanostructures [30]. Multiwalled NTs have been proposed for applications in various fields including optoelectronics [31–33] and exciton coupling with cavity modes [30, 34–36], often exploiting their nonlinear optical properties [37–40]. However, the actual knowledge of the optical and mechanical properties of MoS_2 NTs remains limited. For instance, notwithstanding its importance, the optical extinction cross-section, which governs the attenuation of an optical beam upon interaction with a MoS_2 NT, remains unresolved. On the mechanics side, the acoustic response of MoS_2 NT in the sub-GHz to GHz range, where the fundamental longitudinal and radial modes stand, remains unknown, together with the possibility to actively trigger them.

Over the last decades, the discovery of new nanomaterials has fueled the growth of nanotechnologies. Epitaxial growth techniques [41] have enabled the development of high aspect-ratio nanostructures, such as **III-V semiconductor nanowires** [42, 43], among which **Indium arsenide (InAs) nanowires (NWs)** have demonstrated a wide range of applications [22, 42, 44–47]. Due to their small energy band gap and low effective electron mass, they are particularly attractive for high electron mobility applications in nanodevices, including the development of nanoscale field-effect transistors (FETs). High-performance InAs NW-based FETs have been extensively studied, showcasing exceptional mobility and ultra-high frequency response [48–53]. In addition, the realization of NW-based electronic devices on flexible substrate [22, 54] highlights their potential for flexible nanoelectronics applications [55, 56], while their mechanical strain was predicted to efficiently modulate electrical properties [57–59]. Besides, NW-based devices have been demonstrated for gas sensing applications [60–62] as well as for the realization of new platforms for quantum electron transport [63–65], while their narrow band gap makes them especially promising for optoelectronics [42, 66–69]. Finally, these systems have also been proven highly efficient in iontronic [53, 70–72] and thermoelectric applications [47, 73, 74].

The broad applicability of InAs NWs, particularly in flexible and electromechanical devices, underscores the fundamental importance of understanding their **mechanical properties** [75]. Significant research has focused on the mechanical behaviour of NWs [76–78] with a few critical studies on Young's modulus and mechanical strength of InAs NWs [79–81], and limited theoretical calculations [82, 83]. A comprehensive understanding of the mechanical behaviour of wurtzite (WZ) InAs NWs, particularly in relation

to their morphological characteristics, is still lacking. Most analyses rely on simplified analytical models that do not account for the detailed morphological features of these nanostructures. In addition, the efficiency of InAs NWs in electronic devices is also affected by the temperature dependence of electron mobility [84], which has motivated the investigation of the **thermal properties** [84, 85]. In this context, InAs NW thermal conductivity [46, 86, 87], quantum effects related to phonon transport [88, 89] and interactions with the surrounding environment [90, 91] were the subject of several investigations.

Regarding both MoS_2 NTs and InAs NWs, and particularly regarding individual nanostructures of these two material classes, as a matter of fact the mechanical and thermal transfer properties are still poorly investigated. This is due to the inherent challenges involved. The energy dynamics in these nanostructures occurs on an ultrafast timescale, ranging from ten picoseconds to tens of nanoseconds (depending on the nanostructure dimensions and its environment), and on length scales ranging from a micrometer to a few nanometers, involving small energy fluxes. These aspects call jointly for ultra-fast, low-perturbing, non-contact, high-sensitivity techniques with mesoscale to nanoscale resolution. **Ultrafast spectro-nanoscopy techniques** have recently demonstrated their effectiveness for contactless investigations of high-frequency mechanical responses [92–102] and thermal transfer processes [103–111] at the nanoscale. These techniques, supported by nanoscale spatially-resolved imaging methods [112–116], allow the precise detection and time-resolved optical characterization of energy transfer processes down to individual nanostructures.

This thesis focuses on different aspects of mechanical and thermal energy transfer in individual MoS_2 NTs and individual InAs NWs, employing ultrafast all-optical techniques. Depending on the system, the focus is on the mechanics/thermics taking place within the nanostructure or between the nanostructure and its environment.

The as-grown NTs and NWs samples being affected by dispersion in their shape, size and morphology, a key aspect of the present thesis is the investigation of individual nano-objects. On one side, this allows to avoid inhomogeneous broadening effects which would hinder the detection of the acoustic vibrations, while on the other side it allows a one-to-one correlation between the measured thermo-mechanical response and the nano-object morphology.

In order to measure an individual nano-object, while inspecting the potential impact of the environment, a fabrication protocol is developed for the positioning of individual nanostructures either suspended over a trench (isolated nano-object) or supported on a substrate. In particular, Polymethyl Methacrylate (PMMA) and sapphire are used as

paradigmatic supporting substrates, transparent in the visible range (a technical requirement since the optical measurements are performed in transmission). PMMA is a polymer with low acoustic impedance (3×10^6 Kg/m^{2}s) and thermal conductivity (0.19 W/m·K). It is thus paradigmatic of mechanically soft and thermally insulating materials. Sapphire is instead a rigid crystalline dielectric with high acoustic impedance (45×10^6 Kg/m^{2}s) and thermal conductivity (27.21 W/m·K), thus being representative of rigid mechanical systems at the nanoscale. Furthermore, these materials are commonly employed in a variety of applications ranging from optomechanical sensors [117] to nanoresonators [96] and nanoscale thermal management [118].

Specifically, the topics addressed in this thesis, and their organization into chapters, are as follows.

Chapter 1 provides the theoretical background and models relevant to the discussion. The first part introduces the optical properties of semiconducting nanostructures relevant to this work. The chapter then describes an adaptation of Mie theory for modelling light scattering by infinite cylinders, a pertinent approximation for high aspect-ratio nanostructures such as the NTs and NWs here investigated. The key equations of continuum mechanics and heat transfer are summarized. The vibrational eigenmodes of cylinders and cylindrical shells are presented. The thermal boundary (or Kapitza) conductance and its relevance in nanoscale-heat transfer are revised. Finally, the chapter outlines the methodologies employed for the analysis of signals obtained from pump-probe experiments.

Chapter 2 describes the optical techniques deployed to study individual high aspect ratio nanostructures. Spatial Modulation Spectroscopy (SMS), a method for detecting nanostructures with sub-wavelength dimensions and exiguous optical cross-section, is introduced. Next, Extinction Spectroscopy (ES) is described, both as a means to measure the absolute extinction cross-section of MoS_2 NTs and as a tool for detecting and imaging larger nanostructures. The chapter concludes with a description of Ultrafast Time-Resolved Spectroscopy (US), the primary technique used in this work to investigate time-resolved energy transfer processes.

Chapter 3 focuses on the synthesis and nanofabrication methods exploited to obtain the samples. First, it details the growth of multiwall MoS_2 NTs and WZ InAs NWs. Then, it outlines the fabrication protocols to obtain individual suspended nanostructures, as well as PMMA- and sapphire-supported ones. Finally, post-processing characterization (electron microscopy and Raman spectroscopy) is briefly addressed.

Chapter 4 reports on the optical and mechanical properties of MoS_2 NTs. On the optics side, the experimentally retrieved value of the optical extinction cross section per unit

length, $\sigma_{L,ext}^{NT}$, of individual MoS_2 multiwall NTs is reported over the 440 - 940 nm wavelength range, for light polarization both parallel and perpendicular to the NT longitudinal axis. The impact of NT diameter and environment on $\sigma_{L,ext}^{NT}$ is addressed for individual NTs with diameters of 120 and 220 nm, in suspended, sapphire-supported, and PMMA-supported configurations. The findings are interpreted in conjunction with finite element method simulations, informed by morphological input parameters obtained from electron microscopy, offering insight into the contributions of absorption and scattering cross sections per unit length to the overall $\sigma_{L,ext}^{NT}$. These quantitative results are of relevance in view of potential optoelectronic applications involving MoS_2 NTs, while providing benchmark values for theoretical investigations of their nano-optical response. Regarding the mechanics, impulsively excited ultra-high frequency (GHz range) acoustic oscillations are addressed in individual MoS_2 NTs, by means of time-resolved optical nanoscopy. Measuring NTs with two distinctive diameters, in conjunction with simple all-analytical models, allows for resolving the NTs radial and breathing modes. The assessment of these modes, together with analytical models, is exploited to retrieve the thickness of the NT shell, a key morphological parameter not accessible via other non-destructive techniques. This shows that the technique enables access to sub-surface morphological information on hollow nanostructures.

Chapter 5 is devoted to the study of InAs NWs. Their radial and longitudinal vibrational modes are identified and modeled using both analytical and numerical approaches, providing insights into InAs NW elastic tensor and mode attenuation. On the thermal side, preliminary qualitative results are presented. A new metric is introduced allowing to investigate heat transfer from the NW to the PMMA substrate, starting from noisy time-resolved optical traces. The figure of merit correlates well with the extent of the NW-substrate contact, showing that the technique is apt to retrieve morphological information on the contact. The thermal conductance at the NW-PMMA interface is retrieved.

Finally, the scientific outcome is summarized and perspectives are discussed.

The research presented in this thesis was conducted at the NEST Laboratory of Scuola Normale Superiore (SNS) in Pisa, Italy, and the Institute Lumière Matière (iLM) at Universitè Lyon 1 - Claude Bernard in Villeurbanne, France. At the NEST laboratory, I developed the fabrication protocol for producing samples suitable for investigation via ultrafast optical techniques, as detailed in Section 3.2, and I fabricated all the samples reported in this work. Additionally, I characterized both the starting nanomaterials and the final devices, resorting to a multi-technique approach involving, among other techniques, electronic (TEM/SEM) and Raman studies, as described in Sections 3.3 and 3.4.

During my time at iLM, I performed all the optical measurements reported in the thesis (Chapters 4 and 5) and developed the experimental setup for ES, as described in Section 2.2. I was also responsible for all data analysis and interpretation, including analytical simulations based on the existing Mie Theory model for infinite cylinders (Section 4.2.1). Finally, I have been involved in the FEM modeling of the sample response, contributing to the identification of relevant parameters and the interpretation of numerical results.

Chapter 1

Theoretical aspects

1.1 Absorption and scattering in semiconductor nanostructures

The optical properties of semiconductors are fundamentally determined by their electronic band structure. At zero temperature ($T = 0$ K) and for intrinsic (undoped) materials, the valence band is completely filled, while the conduction band remains empty, with the chemical potential situated in the middle of the energy bandgap, E_g. When light interacts with a semiconductor, various **optical linear processes** can occur [119]: light may be reflected or transmitted across the medium, where it can be absorbed, scattered or re-emitted at a different frequency. Figure 1.1 provides a schematic overview of these primary processes. Reflection and absorption, representing the lowest order of light-matter interaction, are the strongest processes.

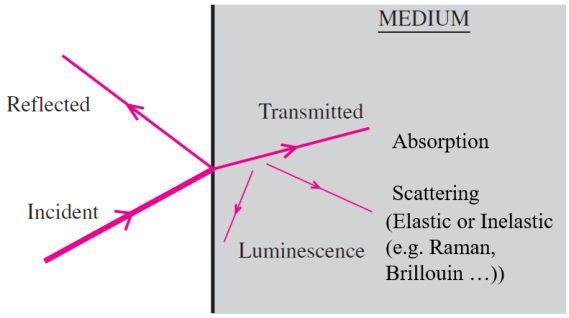

Figure 1.1: Schematic representation of the main linear optical processes occurring in a semiconductor. [119]

Section 1.1.1 introduces the optical constants that describe the interaction of light with semiconductors, along with key concepts governing the optical absorption. Section 1.1.2

presents the essentials of Mie theory at the nanoscale, as applied to light extinction in high aspect-ratio systems.

1.1.1 Optical constants and absorption in semiconductors

The linear optical properties of materials are typically described by the **dielectric tensor** $\varepsilon(\mathbf{q},\omega)$, a second-rank tensor defining the relationship between the Fourier transforms of the electric displacement vector $D(\mathbf{r},t) = \varepsilon_0 E(\mathbf{r},t) + P(\mathbf{r},t)$, and the electric field $E(\mathbf{r},t)$:

$$D_i(\mathbf{q},\omega) = \varepsilon_0 \varepsilon_{ij}(\mathbf{q},\omega) E_j(\mathbf{q},\omega).$$

In most cases, the photon wavelength, λ, is much larger than the lattice constant, a: $\lambda >> a$, consequently, the photon momentum can be assumed $\mathbf{q} \sim 0$, simplifying the dielectric tensor to $\varepsilon(\mathbf{q},\omega) \sim \varepsilon(\omega)$. In isotropic media or cubic crystals, only three diagonal elements exist, allowing $\varepsilon(\omega)$ to be reduced to the scalar **dielectric function** $\varepsilon(\omega)$.

The dielectric function is closely linked to the **complex refractive index** $\tilde{n}$, which typically characterizes the macroscopic optical behaviour of isotropic media:

$$\varepsilon(\omega) = \tilde{n}^2.$$

Here, the real part $n = Re(\tilde{n})$ is related to the phase velocity, and the imaginary part, know as the **extinction coefficient** $\kappa = Im(\tilde{n})$, relates to the **absorption coefficient** α as:

$$\alpha = \frac{4\pi\kappa}{\lambda_0},$$

where λ_0 is the wavelength of light in vacuum. The absorption coefficient α quantifies **optical absorption** through the relation:

$$I(x) = I_0 e^{-\alpha x}$$

where $I(x)$ is the intensity after traveling a distance x in the medium, with initial intensity I_0.

The absorption coefficient can alternatively be expressed in terms of the imaginary part of the dielectric function $Im(\varepsilon(\omega))$:

$$\alpha(\omega) = \frac{\omega}{cn(\omega)} Im(\varepsilon(\omega)).$$

Optical absorption is primarily influenced by the characteristics of the bandgap through **interband electronic transitions**, as illustrated in Figure 1.2 [120]. When the photon energy E_p exceeds the gap energy E_g, electrons may be excited from the valence to the

conduction band. If the semiconductor or insulator has the extrema of the conduction and valence bands at the same point of the Brillouin zone, i.e. it is characterized by a **direct bandgap**, a direct interband transition can take place (Figure 1.2a). Photons usually carry small momentum, so these *vertical transitions* are the most probable. However several crystals have misaligned conduction and valence band extrema (**indirect bandgap**). In this case, *non-vertical transitions*, although less efficient, may occur if there is a source of momentum *assisting* the transition (Figure 1.2b). This is usually provided by phonons, and phonon-assisted optical transitions are of most relevance for this work because they affect the thermal and mechanical energy of the system (see Section 1.2).

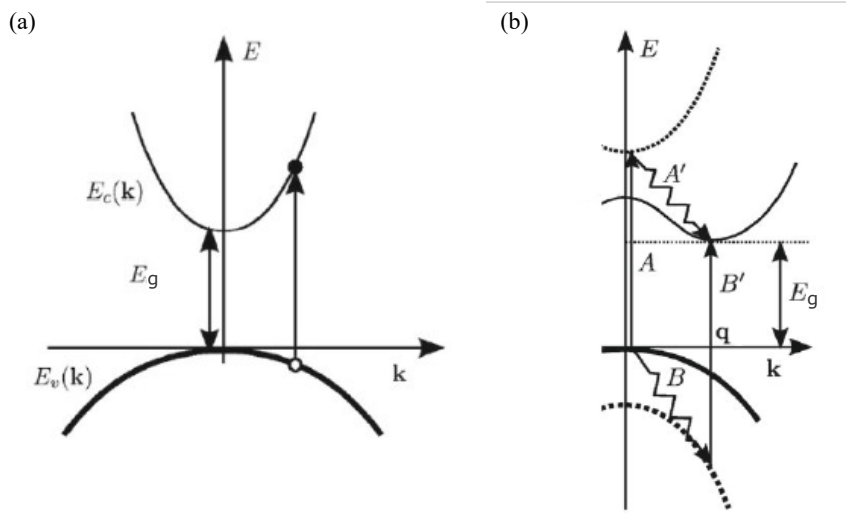

Figure 1.2: Schematic representation of the optical transitions across the bandgap of a semiconductor with direct (a) and indirect (b) bandgap. [120]

Figure 1.2b shows the schematic of a phonon-assisted transition in an indirect band structure, in the textbook case in which the top of valence band is at the centre of the Brillouin zone $q = 0$ and the bottom of the conduction band is at $q \neq 0$, and both bands are parabolic near the extrema, with isotropic effective mass. A second-order perturbation theory which considers both electromagnetic and phononic perturbations can be used to specifically evaluate the transition probability [120]. Generally, the transition can be considered as a vertical transition (A in the Figure) from the top of the valence band to a virtual state with energy higher than the bandgap, happening with nearly zero momentum, followed by a phonon-assisted scattering (A') to the bottom of the conduction band.

A microscopic formulation of the imaginary dielectric constant, which is related to the absorption coefficient, can be derived from quantum mechanical treatments of optical

transitions. The imaginary dielectric constant is proportional to the transition rate, which is affected by the *joint density of states*. In nanostructures, the density of states might be affected by quantum confinement effects, consequently altering the optical absorption.

1.1.2 Mie Theory for an infinite cylinder

Mie theory provides an analytical framework for modeling **absorption** and elastic **scattering** of plane electromagnetic waves by spherical particles whose dimensions are comparable to the wavelength of light $r \sim \lambda$ and whose optical constants are known [121]. Maxwell's equations for a linear, isotropic and homogeneous medium are solved using Bessel functions of the first and second type (J_n and Y_n) and Hankel functions ($H_n^{(1)} = J_n + iY_n$) to expand plane waves in vector spherical harmonics. The scattered electromagnetic field is written as a superposition of normal modes weighted by appropriate *scattering coefficients*, which are explicitly obtained from the electromagnetic boundary conditions. The solution to this problem yields the *absorption, scattering and extinction cross-sections*, indicating how the particle affects light beam propagation, a topic further discussed in Chapter 2.

This theory extends to **infinitely long cylinders** with radius r and complex refractive index n_c, immersed in a homogeneous medium of refractive index n_m [121]. This model applies to high-aspect-ratio nanostructures, such as the MoS_2 NTs analyzed in Chapter 4, with diameter-to-length ratio $\frac{D}{L} \simeq 0.05$. In a cylindrical coordinate system with the cylinder axis along the z-axis, scattering coefficients a_n and b_n are derived for incident electric field polarized *parallel* and *perpendicular* to the cylinder axis, respectively.

The cross-sections per unit length for **perpendicular polarization** are:

$$\sigma_{ext\perp}^{L} = \frac{4r}{u} Re[a_0 + 2\sum_{n=1}^{\infty} a_n]$$

$$\sigma_{sc\perp}^{L} = \frac{4r}{u}[|a_0|^2 + 2\sum_{n=1}^{\infty} |a_n|^2]$$

$$\sigma_{abs\perp}^{L} = \sigma_{ext\perp}^{L} - \sigma_{sc\perp}^{L}$$

with scattering coefficients defined as:

$$a_n = \frac{mJ_n'(u)J_n(mu) - J_n(u)J_n'(mu)}{mJ_n(mu)H_n^{(1)'}(u) - J_n'(mu)H_n^{(1)'}(u)}$$

$$b_n = 0$$

where $u = kr$, with wavevector $k = n_m \frac{2\pi}{\lambda}$ and $m = \frac{n_c}{n_m}$ refractive index ratio. For **parallel polarization**, similar expressions hold:

$$\sigma^L_{ext\parallel} = \frac{4r}{u} Re[b_0 + 2\sum_{n=1}^{\infty} b_n]$$

$$\sigma^L_{sc\parallel} = \frac{4r}{u}[|b_0|^2 + 2\sum_{n=1}^{\infty} |b_n|^2]$$

$$\sigma^L_{abs\parallel} = \sigma^L_{ext\parallel} - \sigma^L_{sc\parallel}$$

involving the corresponding scattering coefficients:

$$a_n = 0$$

$$b_n = \frac{J_n(mu)J'_n(u) - mJ'_n(mu)J_n(u)}{J_n(mu)H_n^{(1)'}(u) - mJ'_n(mu)H_n^{(1)'}(u)}.$$

The expansion of multipolar modes converges efficiently up to $n = 50$, permitting practical approximations of the extinction, scattering, and absorption cross-sections.

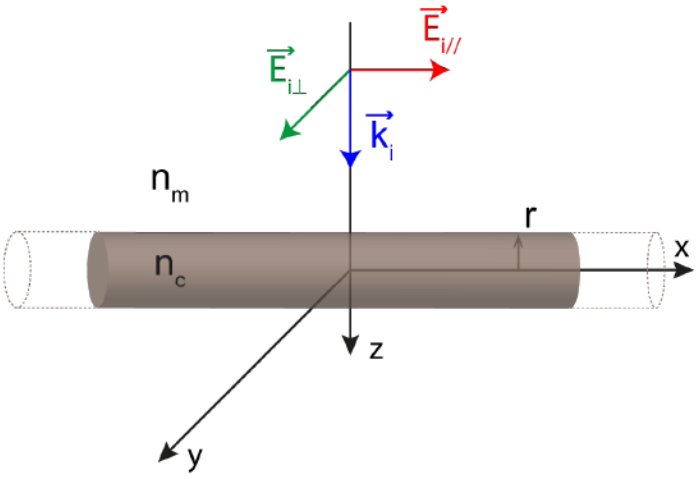

Figure 1.3: Schematic representation of a plane wave impinging on an infinite cylinder of radius r and refractive index n_c, situated in a medium with refractive index n_m. The incident plane wave is normal to the cylinder axis, with orthogonal electric field components represented in red and green. [122]

1.2 Energy transfer at the nanoscale

This PhD work aims to investigate the ultrafast response of nanoscale systems using optical techniques. The internal energy, ΔU, of a system can be transformed and transferred as heat, ΔQ, or work, ΔW, as described by the first principle of thermodynamics,

$\Delta U = \Delta Q + \Delta W$. This work focuses on the microscopic processes governing the mechanical (Section 1.2.1) and thermal (Section 1.2.2) energy transfer in single high aspect-ratio semiconducting nanostructures.

1.2.1 Mechanics

Small displacements of atoms around their equilibrium positions in a crystal lead to the formation of normal propagating vibrational modes, which, in a classical description, correspond to solutions of the elastic wave equation.
In nanostructures, where the system dimensions are comparable to the wavelengths of these vibrations, the geometry and boundary conditions impose constraints on the vibrational spectrum. These constraints determine the frequencies and shapes of the resulting confined vibrational modes. This work investigates the confined vibrational modes in InAs NWs and MoS_2 NTs, with a particular focus on breathing, thickness and extensional modes.

Origin of the oscillations

Ultrafast optical excitation of nanostructures can induce vibrational modes. In semiconductors, an ultra-short laser pump pulse with photon energy exceeding the material's energy bandgap initiates the generation of electron-hole pairs, and induces external mechanical stress on the lattice. This stress can be driven by two main mechanisms [123]: displacive excitation and lattice thermal expansion.

In the **displacive excitation** process, the creation of electron-hole pairs leads to a modification in the semiconductor's energy band structure, expressed as a change in electronic energy δU (as illustrated in Figure 1.4). This alteration prompts the atoms within the crystal lattice to adopt a new, temporary equilibrium position, resulting in strain within the material. The term *displacive* indicates this temporary *shift* in the atoms' equilibrium positions. The motion of the atoms is closely associated with phonon dynamics. Compression and expansion stresses within the lattice during this process correspond to the creation and annihilation of acoustic phonons, respectively. The strain in the lattice related to these acoustic phonons, denoted by $\frac{\delta V}{V}$, is proportional to the change in electronic energy δU and can be described by the following relation [119]:

$$\frac{\delta V}{V} = \frac{\delta U}{d_{eh}}$$

where δV represents the change in the crystal volume V, and d_{eh} is the *deformation potential coefficient* (eV), which characterizes the sensitivity of the electronic energy to variations in the lattice spacing induced by atomic displacement.

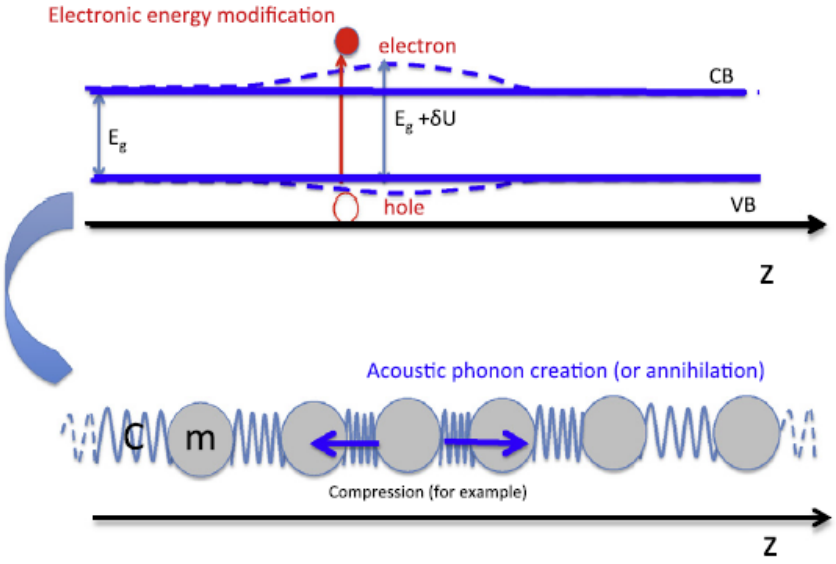

Figure 1.4: Schematic representation of the displacive excitation mechanism in terms of the band structure of a semiconductor. The solid lines represent the conduction and valence bands of the semiconductor at thermodynamic equilibrium, while the dashed lines illustrate the perturbed electronic levels following electron-hole pair generation. [123]

The **thermal expansion** mechanism [124], also known as *thermoelastic effect*, is another common process in photoacoustic wave generation [125]. In semiconductors, lattice heating due to an ultrafast laser pulse is primarily associated with the intraband relaxation of electrons and holes within the conduction and valence bands, respectively. As illustrated in Figure 1.5, electrons in the valence band are excited to high-energy states in the conduction band via absorption of photons with energy significantly exceeding the band gap. These *hot* electrons then relax to the conduction band bottom through intraband transitions, predominantly emitting phonons as a result of electron-phonon scattering. The energy excess is transferred from electrons to phonons, consequently increasing the lattice temperature. Due to the anharmonicity of the lattice potential energy, the increase of the phonon population at high vibrational energy levels leads to a modification of the lattice parameter relative to its low-energy configuration. In addition, carriers accumulation at the bottom of the conduction band (top of the valence band) supports the deformation potential mechanism, as discussed previously. From these states, carriers can undergo radiative interband recombination, emitting photons, or non-radiative recombination through phonon interactions, further contributing to lattice heating.

The relationship between the strain induced by thermal expansion ($\frac{\delta V}{V}$) and the in-

crease in lattice temperature (δT_L), is given by:

$$\frac{\delta V}{V} = 3\beta\delta T_L,$$

where β is the linear thermal expansion coefficient.

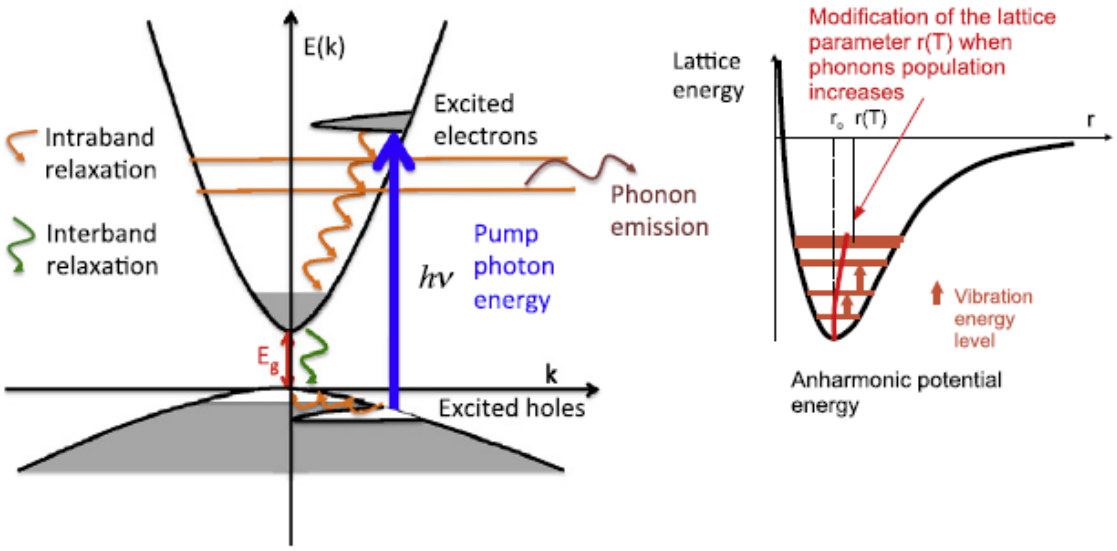

Figure 1.5: Schematic representation of the microscopic mechanism leading to the lattice thermal expansion in a semiconductor heated by ultrafast excitation. On the left, the intraband and interband relaxation processes are represented with red and green arrows, respectively. The intraband relaxation triggers the emission of incoherent phonons and contributes to the local increase of phonon pressure. On the right, the schematic shows a lattice anharmonic potential and the variation of the lattice parameter (i.e. the mean interatomic distance) r(T) that is produced when the vibrational energy increases. [123]

Concepts of acoustics and elastic theory

Vibrational modes in NWs and NTs can be described within the framework of classical acoustic theory, which treats vibrations as macroscopic phenomena. When atoms are displaced from their equilibrium positions, elastic restoring forces arise: combined with the system inertia, they might lead to oscillatory behaviors. Some key definitions and concepts inherent to continuum mechanics are here recalled [126].

The **displacement field** $\vec{u}$ describes the motion of a particle (intended as an infinitesimal volume) relative to its equilibrium position $\vec{l_0}$:

$$\vec{u}(\vec{l_0}, t) = \vec{l} - \vec{l_0} \tag{1.1}$$

The **strain tensor** ε is defined as the symmetric part of the gradient of the displacement field:

$$\varepsilon = \nabla_s \vec{u} \tag{1.2}$$

This tensor quantifies the deformation of the material. The elastic restoring forces that develop between neighbouring particles are described by the **stress tensor** σ.

The relationship between these forces and the system's inertia is governed by the **equation of motion**:

$$\rho \frac{\partial^2 \vec{u}}{\partial t^2} = \nabla \cdot \sigma \tag{1.3}$$

where ρ is the material density. If the vibration is externally driven, additional forces need to be considered.

The relation between elastic restoring forces and material deformation is expressed by **Hooke's Law**:

$$\sigma = C \cdot \varepsilon \tag{1.4}$$

where C is the **elastic stiffness matrix**, which describes the response of a system under stress. To account for external excitation sources, an external stress term σ_{ext} can be added. Inserting Hooke's Law in the right-hand side of the equation of motion yields to **Navier equation**.

Hooke's Law defines the linear proportionality between applied stress and the resulting strain, and it holds in the regime of **elastic deformation**, where the material can return to its original state once the stress is removed. Beyond this regime, permanent (plastic) deformation occurs, eventually leading to mechanical failure of the system.

In isotropic media, the mechanical response to compressive stresses is identical along any of the principal axes (x, y, or z). This symmetry reduces the complexity of the stiffness matrix, such that $C_{11} = C_{22} = C_{33}$ and $C_{12} = C_{13} = C_{23}$. For such materials, two fundamental mechanical properties can be defined: Young's modulus E and Poisson's ratio ν. **Young's modulus** quantifies the resistance of the material to deformation in a specific direction (iii) under uniaxial stress, neglecting the effects in other directions. It is expressed as:

$$E = \frac{\sigma_i}{\varepsilon_i}, \tag{1.5}$$

where σ_i is the applied normal stress and ε_i is the resulting normal strain in the same direction. **Poisson's ratio** describes the material's tendency to deform in the directions (j) orthogonal to the direction of the applied stress (i). It is defined as:

$$\nu = -\frac{\varepsilon_j}{\varepsilon_i}, \tag{1.6}$$

where ε_j is the transverse strain and ε_i is the axial strain. These parameters allow for a straightforward relationship between the elastic constants and the material properties (E, ν) in isotropic media:

$$C_{11} = \frac{E(1-\nu)}{(1+\nu)(1-2\nu)}, \quad C_{12} = \frac{E\nu}{(1+\nu)(1-2\nu)}, \tag{1.7}$$

highlighting the advantage of using isotropic materials in mechanical modeling.

Equations 1.3 and 1.4 describe the dynamics of a continuum body in the linear elastic response regime. The above-mentioned equations have to be complemented with appropriate boundary conditions. Solving these equations (together with the boundary conditions) in the frequency domain provides the vibrational eigenfrequencies and eigenvectors (i.e. displacement field) of the system under test. The above equations can also be solved in the time domain, provided the initial conditions are known. In this case, one obtains the displacement field in the time domain.

In general, the mechanisms contributing to the attenuation of an acoustic oscillation can be distinguished as intrinsic or extrinsic. For the case of a nanoresonator, *extrinsic* attenuation refers to the energy loss out of a nanoresonator mode via radiation of acoustic waves in the surrounding environment. This can be modeled by considering the resonator mode as composed of two counter-propagating plane waves to form a stationary wave. Across the interface between the nanoresonator and its surroundings, the plane wave loses some energy towards the substrate. The acoustic problem is energetically open, and solutions are described as quasi-stationary states [99]. Conversely, *intrinsic* attenuation accounts for energy dissipation within the nanoresonator itself, where mechanical energy is ultimately converted into thermal energy. To incorporate intrinsic losses, a modified form of Hooke's Law can be introduced, which includes an elastic damping term that depends on both temperature and frequency. At room temperature, it can be described as a viscous damping:

$$\sigma = C \cdot \varepsilon + \eta \cdot \frac{\partial \varepsilon}{\partial t} \tag{1.8}$$

where η is the **viscosity tensor**.

The **attenuation time** τ arises as a term in the exponential function outlining the displacement, describing the rate at which the amplitude of the acoustic wave decreases due to energy dissipation (both within the system and/or to its surroundings):

$$\vec{u} = \hat{x} e^{i(\omega t - ky)} e^{-\frac{t}{\tau}} \tag{1.9}$$

A useful parameter for characterizing the system's performance as a resonator is the **quality factor** Q, defined as:

$$Q = \frac{\pi f}{\Gamma} \tag{1.10}$$

where $f = \frac{\omega}{2\pi}$ and $\Gamma = \frac{1}{\tau}$ is the decay rate of the oscillation.

Vibrational eigenmodes of cylinders and cylindrical shells

Depending on the geometry of the system, the nanomaterial properties, and the light coupling, some eigenmodes are more likely to be optically excited in nanostructures than others. They are found solving Equation 1.3 in cylindrical symmetry, with appropriate boundary conditions.

From symmetry considerations, within the laser excitation adopted in this thesis, two classes of modes are likely to be excited:

- *axial modes* in which the vibration occurs along the cylinder's axis, such as the **extensional mode** represented in Figure 1.6, top panel,
- *radial modes* which describe a vibration that occurs predominantly in the radial direction, such as the **breathing mode** which can take place both in full cylinder and cylindrical shell. The latter involves uniform expansions and contractions of the structure's cross-section, creating major displacements along the radius (shown in Figure 1.6, bottom panel). In presence of a shell as occurs for nanotubes, the breathing mode can be visualized as the synchronized movement of the internal and external surfaces of the shell, leading to a uniform deformation of the *average radius* of the tube. Differently, in the **thickness mode**, during the vibration the main deformations occur just in the direction of the *shell thickness*, i.e. the internal and external surfaces move oppositely.

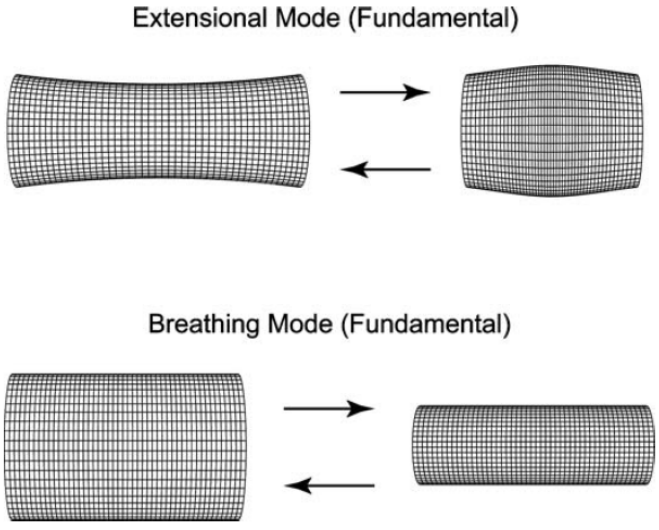

Figure 1.6: Schematic representation of some vibrational modes of nanostructures with cylindrical symmetry. [127]

The analytical models adopted in this work for extensional and breathing modes in InAs

NWs and for breathing and thickness modes in MoS_2 NTs are detailed in the following sections.

Analytical derivation of extensional and breathing modes for a high aspect-ratio cylinder

The analytical calculation of the vibrational periods associated with the breathing and extensional modes InAs NWs is performed in Chapter 5 using the model developed in [128], to obtain a basic understanding. This model applies to high aspect-ratio cylinders, where the length L significantly exceeds the radius R, and assumes the material (with density ρ) to be linearly elastic, isotropic with Young's modulus E, and remaining at a constant temperature after excitation. Consequently, an initial uniform strain can be applied in both the radial and longitudinal directions:

$$\vec{U}(t=0) = \varepsilon(r\hat{r} + z\hat{z})$$

where $\vec{U}$ represents the displacement vector, r and z the radial and longitudinal components of the system in cylindrical coordinates, $\hat{r}$ and $\hat{z}$ are their corresponding unit vectors, ε denotes the magnitude of the initial strain, and t is the time. The Navier equation (Equation 1.3) is solved for the extensional and breathing modes by considering solutions of the form:

$$\begin{aligned} \vec{U}_{\text{ext}} &= \varepsilon \vec{u}_{\text{ext}}(r,z)\, e^{-i\omega_{\text{ext}}t}, \\ \vec{U}_{\text{br}} &= \varepsilon \vec{u}_{\text{br}}(r)\, e^{-i\omega_{\text{br}}t} \end{aligned} \tag{1.11}$$

The frequency of these modes is determined considering zero normal stress at the surface of the cylinder ($r = R$), resulting in the following expressions for the resonant angular frequencies:

$$\omega_{\text{ext}}(n) = \frac{2n+1}{L}\pi\sqrt{\frac{E}{\rho}},$$

$$\omega_{\text{br}}(n) = \frac{\tau_n}{R}\sqrt{\frac{E}{\rho}\frac{(1-\nu)}{(1+\nu)(1-2\nu)}},$$

where n represents the mode number and τ_n corresponds to the n-rooth of the eigenvalue equation:

$$\tau J_0(\tau) = \frac{1-2\nu}{1-\nu} J_1(\tau), \tag{1.12}$$

with J_0 and J_1 Bessel functions of the first kind.

For the fundamental mode ($n = 0$), the corresponding vibrational periods are given by:

$$T_{ext} = \frac{2L}{\sqrt{\frac{E}{\rho}}}, \tag{1.13}$$

$$T_{br} = \frac{2\pi R}{\tau_0 \sqrt{\frac{E}{\rho} \frac{(1-\nu)}{(1+\nu)(1-2\nu)}}}. \tag{1.14}$$

Analytical models for breathing and thickness modes applied to cylindrical shells.

To model the radial modes identified in US experiments on multi-wall MoS_2 NTs, two analytical approaches are employed. The breathing mode period is determined by adapting an analytical model developed for single-wall NTs (Figure 1.7a and b) [129]. The thickness mode period is determined by mapping the MoS_2 NT on an effective thin film and calculating the thickness mode for the latter (Figure 1.7c and d).

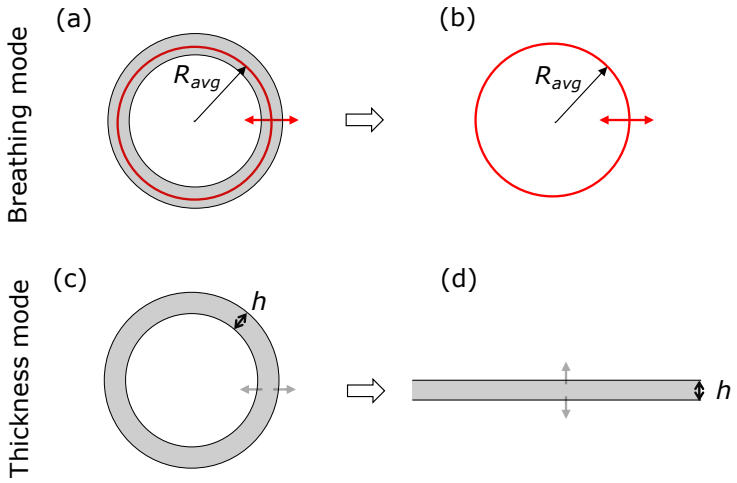

Figure 1.7: Schematic of the cylindrical shell section with average radius R_{avg} and thickness h. The average radius dominates displacement in the breathing mode (a), modeled for the case of a single wall NT of radius corresponding to the average radius of the multiwall MoS_2 NT. (b) The thickness dominates displacement in the thickness mode (c), derived from a model for an infinite thin film of the same thickness as the MoS_2 NT shell, h (d).

Although both derivations assume isotropic material behaviour, the anisotropic nature of MoS_2 is incorporated by employing different Young's moduli during the analysis of the modes. Considering that different stiffness coefficients dominate the displacement in the two cases, the tangential Young's modulus of MoS_2 is inserted for the breathing mode, while a Young modulus $E \sim C_{33}$ is adopted for the thickness mode, this stiffness coefficient relating the stress to strain along the out-of-plane direction.
These two analytical approaches allow capturing the relevant physics, without hindering it under the precise yet physics-obscuring brute force approach inherent to FEM simulations. Despite their inherent simplifications, our approaches enable a comprehensive

characterization of the radial modes observed in the experiments.

Breathing mode frequency for a cylindrical shell of infinitesimal thickness. The analytical expression for the breathing mode frequency of a cylindrical shell with infinitesimal thickness was derived by mimicking a single-wall NT with radius R [129], where R is taken as the average radius of the actual MoS_2 NT, R_{avg}, under the assumption that the NT is infinitely long. The physical rationale behind adopting this model is that the primary forces responsible for the breathing mode are the tangential ones, rather than the van der Waals (VdW) interactions between adjacent MoS_2 layers, which are relatively weak (i.e., in VdW structures, $C_{33} < C_{11}$). The NT is assumed to experience negligible axial movements. Under these conditions, deformation is constrained to the tangential direction ϕ. Figure 1.8 illustrates the tangential forces acting on an infinitesimal segment of the cylindrical shell, providing a visual understanding of the derivation process. The material is assumed to be homogeneous and isotropic with a defined Young's modulus.

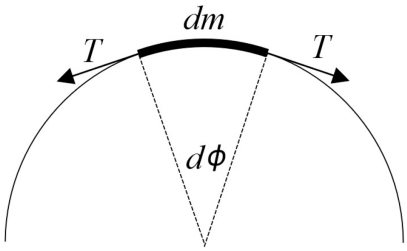

Figure 1.8: Schematic representation of tension acting on the infinitesimal segment of the cylindrical shell. [129]

Since the tangential forces can be assumed to dominate the breathing vibration also for multi-wall NTs, in this thesis the same formulation is applied to the case of multi-wall MoS_2 NTs. They are approximated as single-wall NTs with an effective radius equal to the average radius, $R = R_{avg}$. This approach aligns with the observation that the breathing mode corresponds to a uniform displacement of the average radius.
A schematic representation of this concept is provided in Figure 1.7a and b.

To account for the cylindrical geometry, the equations of motion are expressed in cylindrical coordinates. Simplifications are introduced by assuming no axial movements ($\varepsilon_{zz} = \varepsilon_{z\phi} = 0$), meaning the shell deforms only tangentially. The tangential strain is therefore defined as:

$$\varepsilon_{\phi\phi} = \Delta R / R_{avg}, \tag{1.15}$$

where ΔR is the radial displacement from the average radius R_{avg}.
An infinitesimal segment of the shell is considered, with dimensions dz along the axis and

$Rd\phi$ in the azimuthal direction. The tangential tension acting along the edges of this segment is given by:

$$T = \sigma_{\phi\phi} dz,$$

where $\sigma_{\phi\phi}$ is the tangential stress. This results in a recovery force:

$$dF = T \cdot 2sin(d\phi/2) \simeq \sigma_{\phi\phi} d\phi dz$$

where the small-angle approximation, $sin(d\phi/2) \simeq d\phi/2$, has been applied.
The mass of the infinitesimal shell segment is $dm = \rho^{2D} R d\phi dz$, where ρ^{2D} is the mass density per unit area. The radial force opposing expansion is given by:

$$dm \frac{d^2R}{dt^2} = -dF$$

Substituting for dm and dF, and dividing through by $d\phi dz$, the radial equation of motion becomes:

$$\rho^{2D} \frac{d^2R}{dt^2} = -\frac{\sigma_{\phi\phi}}{R}.$$

Assuming $R \simeq R_{avg}$, the equation can be rewritten using the tangential strain definition 1.15 and the constitutive relation for stress and strain 1.5:

$$\rho^{2D} \frac{d^2}{dt^2}(R_{avg} + \Delta R) = \rho^{2D} \frac{d^2}{dt^2} \Delta R = -\frac{\sigma_{\phi\phi}}{R_{avg}} = -\frac{E^{2D} \Delta R}{R_{avg}^2}.$$

This simplifies to the harmonic oscillator equation, where the angular frequency ω is given by:

$$\omega = \sqrt{\frac{E^{2D}}{\rho^{2D} R_{avg}^2}}. \tag{1.16}$$

The corresponding period is:

$$T = \frac{2\pi}{\omega} = \frac{2\pi R_{avg}}{v} \tag{1.17}$$

where the tangential sound velocity v is:

$$v = \sqrt{\frac{E^{2D}}{\rho^{2D}}}. \tag{1.18}$$

For a multilayer shell, the effective Young's modulus E^{2D} and density per unit area ρ^{2D} are related to their 3D counterparts by the shell thickness h:

$$E_{2D} = E_{3D} \cdot h \ , \quad \rho_{2D} = \rho_{3D} \cdot h$$

Thus, the tangential sound velocity reads:

$$v = \sqrt{\frac{E^{3D}}{\rho^{3D}}}.$$

This analytical framework allows for the estimate of the breathing mode period in cylindrical shell structures, facilitating the analysis of the experimental results presented in Chapter 4.

Thickness mode in a thin film. The thickness mode represents a type of oscillation that can typically be excited in thin films. In a thickness mode the film's displacement is perpendicular to its free surfaces. To simulate the thickness mode of the MoS_2 NT, the NT is modeled as an isotropic and homogeneous film of thickness h and Young modulus $E \sim C_{33}$ of MoS_2, see schematics in Figure 1.7c and d. To visualize the idea, imagine to cut the NT along it's length and unfold it in a flat sheet. The unfolded NT is hence tantamount to a film of thickness h. The physical idea behind the adoption of this model is that the main forces responsible for the thickness mode are due to the interactions between adjacent MoS_2 multilayers, which are accounted for by the stiffness tensor component C_{33} of MoS_2.

Starting from the general Equation 1.3 for an elastic medium, the problem simplifies for a longitudinal wave with motion only along z (orthogonal to the film surface). Using the relation $\sigma_{zz} = E\frac{\partial u_z}{\partial z}$ from the definition of stress in terms of Young's modulus E, the Equation 1.3 reduces to a 1D wave equation:

$$\frac{\partial^2 u_z}{\partial t^2} = v^2 \frac{\partial^2 u_z}{\partial z^2}.$$

Here, v is the sound velocity in the material, defined as:

$$v = \sqrt{\frac{E}{\rho}}, \tag{1.19}$$

where ρ is the material density. For anisotropic materials (as the one considered in this work), the Young's modulus appearing in this formula differs from the one used for the breathing mode.

A solution for a longitudinal wave propagating in the z-direction is searched in the form:

$$u_z(z,t) = e^{-i(kz+\omega t)}$$

where $\omega = \frac{2\pi}{T}$ is the angular frequency and $k = \frac{\omega}{v}$ is the wave vector. The boundary conditions arise from the assumption that the surfaces at $z = 0$ and $z = h$ are free, meaning the stress must vanish at these points ($\sigma_{zz} = 0$). These conditions imply that u_z must be a standing wave solution with antinode at the boundaries and imply the discretization of the wave vector:

$$k = \frac{n\pi}{h},$$

where n is a positive integer representing the mode number ($n = 1, 2, 3, \dots$). The angular frequency for a given mode is:

$$\omega = kv = \frac{n\pi v}{h}.$$

From this, the oscillation period T is:

$$T = \frac{2h}{nv}. \tag{1.20}$$

Here, n corresponds to the harmonic number, with $n = 1$ representing the fundamental thickness mode, which will be used in Chapter 4 for the estimate of the shell thickness of MoS_2 NTs.

1.2.2 Thermics

In this thesis, high aspect ratio semiconductor nanostructures are optically excited at room temperature and investigated using an ultrafast pump-probe technique, detailed in Chapter 2. The unique opportunity to examine these nanostructures in distinct configurations (described in the introduction of this thesis) allows for a comprehensive study of heat transport within the nanostructure and across the interface with solid materials. This enables insights into the predominant heat transfer mechanisms under different conditions. This section introduces fundamental concepts of thermal transport within the material's bulk and across the interface between two materials.

Thermal transport in nanostructure

When thermal transport is primarily governed by phonons, the relationship between the nanostructure's characteristic length (e.g. diameter D for high aspect ratio structures) and the phonon mean free path (l_{ph}) determines the transport regime. In bulk materials or in any case in which $l_{ph} << D$, heat transfer is typically described by the classical diffusive transport based on the Fourier's law. However, when $l_{ph} >> D$, ballistic transport can dominate, meaning all phonons transfer heat propagating without collisions.

In the semiconductor nanostructures investigated in this thesis, the phononic transport likely follows a diffusive regime [130] and the thermal transport can generally be characterized by Fourier law:

$$\mathbf{q}(\mathbf{r}, t) = -k\nabla T(\mathbf{r}, t) \tag{1.21}$$

where $\mathbf{q}(\mathbf{r}, t)$ represents the heat flux vector (in W/m^2), which denotes the energy transfer per unit time and unit area of an isothermal surface in the direction of decreasing temperature, with the gradient (in K/m) being normal to the isothermal surface. Here, k (in W/ m $\cdot$ K) is the material's thermal conductivity, governing the rate of heat flow in the system.

The differential heat conduction equation, which dictates temperature distribution in solids and incorporates Equation 1.21 as the heat conduction constitutive equation, models heat transport in high aspect ratio semiconductor nanostructures under appropriate

boundary conditions. For a stationary, homogeneous, isotropic medium with an internal heat source $g(\mathbf{r}, t)$ (in W/m^3), it is given by:

$$\rho C \frac{\partial T}{\partial t} - k\nabla^2 T = g(\mathbf{r}, t) \tag{1.22}$$

where ρ denotes mass density (in kg/m^3), C specific heat per unit mass (in J/kg·K), and k thermal conductivity (assumed constant). These parameters define the **thermal diffusivity** (in m^2/s):

$$\alpha = \frac{k}{\rho C}. \tag{1.23}$$

When a semiconductor is illuminated by a laser, the source term represents the absorbed electromagnetic power density converted into heat through intraband relaxation of carriers (electrons and holes), as explained in Section 1.2.1 [131]:

$$g(\mathbf{r}, t) = Q(\mathbf{r}, t)(1 - \frac{E_g}{E_p}) \tag{1.24}$$

where $Q(\mathbf{r}, t)$ describes the spatial-temporal profile of absorbed power density delivered to the sample (W/m^3), E_g is the bandgap energy, and E_p is the photon energy ($E_p > E_g$).

This transport framework can be further refined using a statistical model based on the Boltzmann Transport Equation, which is also applicable for describing ballistic-diffusive and purely ballistic transport regime [132].

Thermal transfer at interfaces

Interfaces, defined as the boundary between two distinct materials or phases (e.g., a semiconductor nanostructure on an insulating substrate in the present thesis), play a critical role in many engineering applications as they represent a discontinuity in material properties, potentially affecting energy flow across the system. This is particularly relevant in electronics, where heat transfer at the interface between the nano conducting metallic layout and the dielectric substrate is key towards further device downscaling.

Several mechanisms are responsible for energy transfer inefficiencies at interfaces. A mismatch of phonon and electronic energy spectra of the two materials, referred to as **energy mismatch**, can lead to energy carrier reflection due to a lack of compatible energy states on both sides of the interface. Another key mechanism is **acoustic mismatch** [133], arising from the differences in materials properties such as mass density ρ and speed of sound v_s, which determine acoustic impedance $Z = \rho v_s$, representing resistance to acoustic waves propagation. The interface quality also affects thermal transport due to potential scattering of phonons and electrons at **defects** linked to the interface roughness or surface impurities. Furthermore, in cases involving two materials with different

heat carrier types (metal-insulator interface for instance), electron-phonon interactions may be necessary for energy transfer (e.g., from a metal to an insulator), reducing its efficiency [134].

These mechanisms contribute to hinder the thermal flow, creating a **Thermal Boundary Resistance** (TBR), known also as Kapitza resistance (R_K), originally observed by Kapitza at the interface between superfluid helium and a solid [135]. TBR is defined as the ratio of temperature difference to heat flow across the interface:

$$R_K = \frac{\Delta T}{\mathbf{q}}$$

with interface thermal conductance $G = R_K^{-1}$ (in W/m^2K) often used. The Kapitza length [136], defined as $l_K = kR_K$, represents the equivalent crystal length that would offer similar thermal resistance as the interface, providing an intuitive measure of the interface influence in nanoscale device engineering.

The most prominent theoretical models for predicting TBR at solid-solid interfaces are the *acoustic mismatch* and *diffuse mismatch* models (see Figure 1.9).

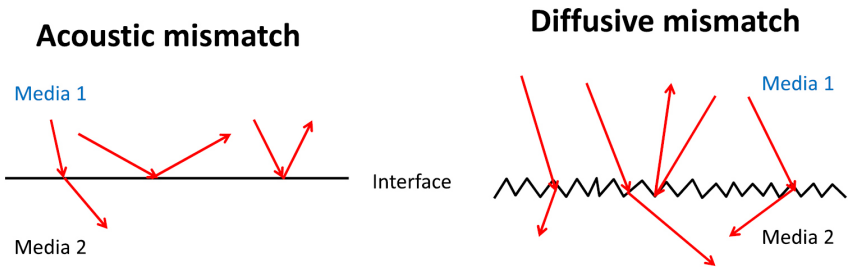

Figure 1.9: Schematic representation of phonon transfer at the interface between two media, as treated in the different models. [137]

These models describe phonon- mediated heat transfer. The two models diverge on assumptions regarding the presence of interface scattering [133]. The acoustic mismatch model is based on continuum acoustics. It treats phonons as plane waves with probabilistic transmission or reflection at the interface between two (continuous) materials, strictly dependent on the **acoustic impedance** Z of each material. Both sides of the interface are assumed isotropic and the transmission probability is independent of temperature, but the main assumption is that the interface is **perfectly smooth** and the phonons transfer through the boundary occurs without scattering or energy loss. This model is particularly suited to defect-free interfaces within crystalline materials, especially under low-temperature conditions where phonon scattering is minimal.

The diffuse mismatch model has been developed to take into account phonon scattering at imperfect interfaces, resulting in a modification of the energy transmission coefficient. A less perfect interface causes **diffusive scattering** of phonons, which lose

memory of direction and frequency and are randomly transmitted through the boundary if there is a matching energy state available in the phonon spectrum of the second material. TBR will depend mainly on the phonon density of states in both materials, i.e. on the phonon spectra overlapping. This model is particularly relevant for high-temperature and rough interfaces where phonon scattering predominates.

The focus of this study is the heat transfer mechanism at the interface between a high aspect ratio nanostructure and its supporting substrate. Assuming that the temperature of the nanostructure remains uniform throughout the cooling process, the heat flux at the interface can be expressed as:

$$\mathbf{q}(r,t) = G(T_{NS}(t) - T_{sub}(r,t))\mathbf{u}, \tag{1.25}$$

where T_{NS} and T_{sub} represent the temperatures of the nanostructure and the substrate, respectively, and $\mathbf{u}$ is a unit vector perpendicular to the interface. This uniform temperature assumption for the nanostructure is valid when the thermal transfer efficiency at the interface is significantly smaller than the thermal diffusion efficiency within the nanostructure. In cases where the length of the nanostructure is comparable to or smaller than the pump spot size ($L \leq$ FWHM), heat diffusion in the direction perpendicular to the interface is the only relevant thermal pathway. Under such circumstances, the Biot number (Bi) typically serves as a metric to determine if the nanostructure temperature can be assumed spatially homogeneous. The Biot number is defined as:

$$Bi = \frac{l/k}{R_K}, \tag{1.26}$$

where l is the characteristic length of the system (that is the radius of the nanostructure in this study) and k is the thermal conductivity of the nanostructure. A $Bi << 1$ implies that thermal transfer is much faster within the nanostructure than across the interface, hence for $Bi << 1$ the nanostructure temperature may be assumed spatially homogeneous.

The heat transfer to the surrounding air is neglected in this analysis due to the significantly lower thermal boundary conductance at the nanostructure-air interface. This may be intuitively understood by noting that the acoustic impedance mismatch between two solids (i.e. InAs NW and PMMA substrate) is much lower than between a solid and a gas (i.e InAs NW and air).

Assuming that the substrate temperature is only slightly perturbed in the region near the nanostructure, it can be approximated as constant and uniform in that vicinity, i.e., $T_{sub}(r,t) = T_0$. Integrating Equation 1.25 over the contact surface S_c one obtains the power transmitted from the nanostructure to the supporting substrate across the

interface. The energy-balance equation [138] (rate of storage of energy in volume V = rate of energy entering through the boundary surface of V) then reads:

$$\frac{CV}{S_c}\frac{dT_{NS}}{dt} = -G(T_{NS}(t) - T_0),$$

where V is the nanostructure volume and C its specific heat.
In this situation, the temperature decrease of the heated nanostructure is mono-exponential and reads:

$$T_{NS}(t) = T_0 + (T_{NS}(0) - T_0)exp(-t/\tau)$$

with characteristic time:

$$\tau = \frac{C}{G}\frac{V}{S_c}, \tag{1.27}$$

inversely proportional to the thermal conductance G.

The approximation of a constant temperature substrate might not always apply, nevertheless, it has the merit of highlighting the relevant physics. Eventually, when necessary, the cooling of the substrate is accounted for either via full FEM simulations or, in the data analysis process, including further exponential decays, each with its own characteristic time.

1.2.3 Signal processing

In this thesis, thermal dynamics and vibrational modes in high aspect ratio nanostructures are excited via ultrafast laser pulses. The experimental signals describing the induced optical changes in optical transmission over time are analyzed in two main steps.

The signal is first fitted using a phenomenological bi- or tri-exponential decay model, which reflects the **cooling dynamics** of the nanostructure:

$$f_{th}(t) = f_{0,th} + \sum_{i=1}^{3} A_{i,th} e^{-\frac{t}{\tau_{i,th}}} \tag{1.28}$$

In this expression, $f_{0,th}$ represents an offset, $A_{i,th}$ are the amplitudes, and $\tau_{i,th}$ are the characteristic time constants associated with the decays. The function that describes the thermal behaviour of the nanostructure provides insights into the underlying heat transfer mechanisms in the system. The time constants derived from the fit are linked to the *timescales* of heat diffusion within the nanostructure and heat transfer at the interfaces between materials.

The cooling dynamics is then taken into account and subtracted to the signal, leaving the pure **vibrational signal** as the residual. The *amplitudes, frequency* and *attenuation time* of the vibrational modes are then extracted by fitting the experimental data using

a function that models the behaviour of a damped oscillator, as described earlier. Depending on the number of vibrational modes excited in the system, one or more damped oscillators are used to fit the signal. This is expressed by the following function:

$$f_{osc}(t) = f_{0,osc} + \sum_{i=1}^{2} A_i \sin(\omega_i t + \phi_i) e^{-\frac{t}{\tau_{i,osc}}} \tag{1.29}$$

where $f_{0,osc}$ represents the background signal and the remaining terms describe the oscillatory motion and its damping behaviour.

Chapter 2

Optical techniques for single nanostructure investigation

This chapter presents the optical techniques employed to investigate the individual nanostructures presented in the introduction. The optical detection of nanostructures with dimensions at the micrometer and sub-micrometer scale, and the determination of their orientation with respect to the light polarization, is not possible resorting on standard diffractive optical techniques in the visible. Therefore, two other techniques are used in this work for imaging the nanostructures: the Spatial Modulation Spectroscopy (SMS), discussed in Section 2.1, and the Extinction Spectroscopy (ES), discussed in Section 2.2. The first technique is designed for the precise detection and characterization of individual nanometric objects. It is characterized by its ability to achieve exceptionally high spatial resolution and signal-to-noise ratio, which are critical for studying structures at the nanoscale. The second technique is optimized for the detection and analysis of micrometer-scale systems with heterogeneous substrates (such as the case of nanostructures suspended over trenches). Finally, Section 2.3 covers Ultrafast Time-Resolved Spectroscopy (US), the key technique used in this work for the exploration of mechanical and thermal energy transfer processes at the nanoscale, with temporal resolution on the order of hundreds of femtoseconds.

2.1 Spatial Modulation Spectroscopy

The SMS is an original far-field optical technique developed by the Lyon FemtoNanoOptics group for single particle investigations [112–116] . It relies on modulating the position of an isolated nano-object and utilizing lock-in detection of the transmitted laser beam for its detection and analysis. This method is particularly effective for studying nano-objects

that exhibit weak absorption or scattering signals or are non-luminescent. Specifically, it enables the investigation of their morphological characteristics by exploiting the close relation with optical properties.

In this work, SMS is primarily employed for detection purposes, especially for the localization (with respect to the laser beam) of the shortest nanostructures studied here - the 550 nm long InAs NWs - which will be discussed in detail in Chapter 5.

2.1.1 Working principle

When a light beam impinges on a nanostructure placed on a transparent substrate, part of the incident beam power (P_{inc}) is absorbed by the nanostructure (P_{abs}), part is scattered (P_{sc}), and part is transmitted (P_{tr}). The incident beam power is known, while the transmitted power can be measured by a photodetector placed along the direction of propagation of the light beam. Therefore, experimentally it is possible to obtain information on their difference, $\Delta P = P_{inc} - P_{tr}$, which is related to the position of the nanostructure on the x-y plane under the incident beam as well as to its optical response (absorption and scattering of light).
However, in general P_{inc} suffers from fluctuations larger or of the same order as the ΔP produced by the nanostructure, hindering the precise detection.

A powerful technique used to increase the signal-to-noise ratio consists in the modulation in time of ΔP and its **synchronous detection** at the modulating frequency. Conventional ways to enable ΔP modulation rely on the variation of the light wavelength or polarization [139, 140]. SMS goes beyond, enabling the precise identification of the **position** of a nano-object [112] and making it possible to perform *spectral* analysis at fixed *polarization* on individual nano-objects.

Specifically, the nano-object is **periodically displaced** within the focal plane of the tightly focused incident beam, as shown in Figure 2.1. The displacement is applied along one direction, namely the y-direction, with fixed amplitude δ_y and frequency f, leading to **modulation** of the transmitted beam **power** over time. The time-dependent signal ΔP is then demodulated at its first or second harmonic. This allows cutting off all the components at different frequencies, enhancing the signal-to-noise ratio and allowing for the detection of the nanostructure, precisely for the localization of the nanoobject with respect to the centre of the light beam. The following paragraph will explain in detail how this process works.

Starting from the assumption that the photodetector has a photosensor of a sufficiently large active area in order to fully collect the transmitted light while excluding the

scattered part, it is possible to assume that

$$\Delta P = P_{inc} - P_{tr} \simeq P_{ext} \tag{2.1}$$

where P_{ext} is the power *extinguished* by the nanostructure, i.e. the sum of the power absorbed and scattered from it:

$$P_{ext} = P_{abs} + P_{sc} \ .$$

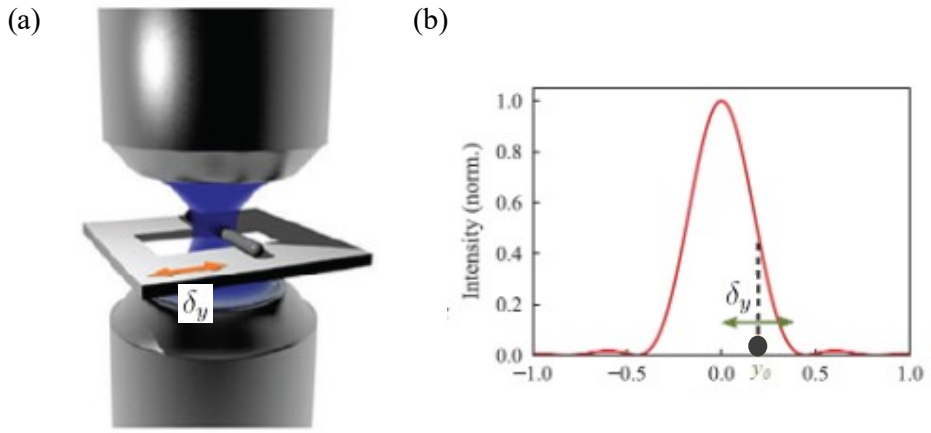

Figure 2.1: (a) Schematic of the SMS setup for position modulation, where the nanostructure oscillates with an amplitude δ_y under the incident laser beam. [113] (b) Graph illustrating the position modulation across the focused intensity profile of the Gaussian beam along the y-axis. [141]

From the extinguished power (and similarly from the absorbed or scattered power), it is possible to extract a meaningful parameter which identifies the effective total area of the nanostructure with respect to the impinging beam, i.e. it describes the amount of light extinguished from the nanostructure. It is called optical extinction cross-section σ_{ext} (m^2):

$$\sigma_{ext} = \sigma_{abs} + \sigma_{sc}$$

and it is defined as the ratio between the extinguished power and the intensity of the incident beam at the position of the nano-object (x_0, y_0):

$$\sigma_{ext} = \frac{P_{ext}}{I(x_0, y_0)} \ .$$

Therefore, it is possible to explicit the **dependence of ΔP from the position** of the nano-object:

$$\Delta P = P_{ext} = \sigma_{ext} I(x_0, y_0) \ .$$

When spatial modulation is applied to the nano-object, the value of power oscillates over time:

$$\Delta P(t) = \sigma_{ext} I(x_0, y_0 + \delta_y \sin(2\pi f t))$$

If the amplitude δ_y is smaller than the beam spot size (i.e. the Full Width Half Maximum ($FWHM$) of the intensity profile of the impinging Gaussian beam), it is possible to perform the Fourier expansion of ΔP up to the second order:

$$\Delta P(t) = \Delta P_0 + \Delta P|_f \sin(2\pi f t) + \Delta P|_{2f} \cos(4\pi f t) + o(\delta_y^2)$$

with components mainly depending on the extinction cross-section and the intensity spatial derivatives:

$$\begin{cases} \Delta P_0(x_0, y_0) = \sigma_{\text{ext}}[\, I(x_0, y_0) + \dfrac{\delta_y^2}{4} \dfrac{\partial^2 I}{\partial y^2}(x_0, y_0)] \\ \Delta P|_f(x_0, y_0) = \sigma_{\text{ext}}\, \delta_y \dfrac{\partial I}{\partial y}(x_0, y_0) \\ \Delta P|_{2f}(x_0, y_0) = -\dfrac{1}{4} \sigma_{\text{ext}}\, \delta_y^2 \dfrac{\partial^2 I}{\partial y^2}(x_0, y_0) \end{cases}$$

For the general case, where the assumption $\delta_y << FWHM$ does not hold, the Fourier components at harmonics nf (where $n = 1, 2, 3, ...$) are given by:

$$\begin{cases} \Delta P|_{nf}(x_0, y_0) = \dfrac{2}{T} \sigma_{ext} \displaystyle\int_{-T/2}^{T/2} I(x_0, y_0 + \delta_y \sin(2\pi f t)) \sin(2\pi n f t) dt \quad (n \text{ is odd}) \\ \Delta P|_{nf}(x_0, y_0) = \dfrac{2}{T} \sigma_{ext} \displaystyle\int_{-T/2}^{T/2} I(x_0, y_0 + \delta_y \sin(2\pi f t)) \cos(2\pi n f t) dt \quad (n \text{ is even}) \end{cases}$$

where $T = 1/f$ is the period. Experimentally, harmonics with $n \geq 3$ show significantly lower amplitudes, making $n = 1$ and $n = 2$ the most influential terms:

$$\begin{cases} \Delta P|_f(x_0, y_0) = \dfrac{2}{T} \sigma_{ext} \displaystyle\int_{-T/2}^{T/2} I(x_0, y_0 + \delta_y \sin(2\pi f t)) \sin(2\pi f t) dt \\ \Delta P|_{2f}(x_0, y_0) = \dfrac{2}{T} \sigma_{ext} \displaystyle\int_{-T/2}^{T/2} I(x_0, y_0 + \delta_y \sin(2\pi f t)) \cos(2\pi (2f) t) dt \end{cases}$$

The Fourier component at f or $2f$ is experimentally measured, and then it is normalized by the incident beam power P_{inc} (i.e. the measurement obtained when the nano-object is not under the beam), to obtain results which are independent from P_{inc}. Finally, the quantity $\frac{\Delta P|_{f,2f}}{P_{inc}}$ is measured.

The detection of the nanostructure laying over the substrate is performed by **raster scanning** the area where the object is expected and collecting the information on $\frac{\Delta P|_{f,2f}}{P_{inc}}$ at each point. Depending on the demodulation frequency, the map resulting from the acquisition resembles one of the simulated maps shown in Figure 2.2. Typically, for the **precise detection of the nanostructure**, a demodulation at $2f$ is preferred, as the maximum of the signal will align exactly with the position of the nano-object.

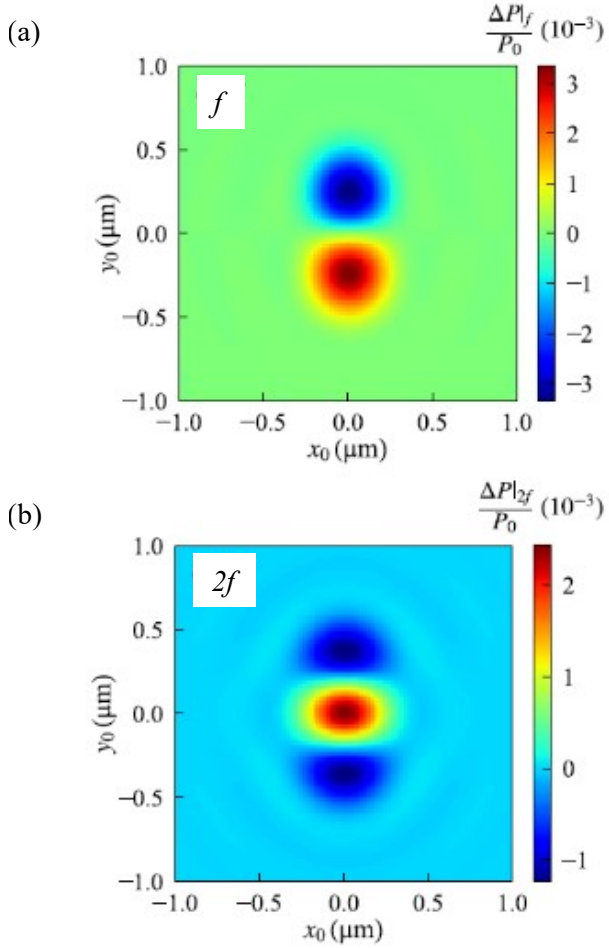

Figure 2.2: Simulated SMS maps generated by the scan of a nanoparticle and calculated for demodulation at frequency $F = f$ (a) and $F = 2f$ (b) [141]. P_0 corresponds to P_{inc} in the main text.

2.1.2 Experimental setup

A Ti:Sa laser source produces the light beam. The laser is a commercial tunable mode-locked oscillator with 2 W average output power and emission wavelength in the range $\lambda = [690 \div 1040]$ nm. It generates pulses approximately 150 fs wide with 80 MHz repetition rate, equivalent to a pulse repetition period of 12.5 nanoseconds. The range of the emission's wavelength can be extended:

- to the visible (VIS) range via an automated optical parametric oscillator (OPO) which enables the emission at $\lambda = [500 \div 750]$ nm, with the same characteristics as the main source;
- to the blue-ultraviolet (UV) range via a 100 μm thick barium beta-borate (β-BaB_2O_4) crystal (BBO), which doubles the frequency of the light source via Second-

Harmonic Generation (SHG).

Once the wavelength is fixed, the beam is directed towards a telescope which enlarges the spot size intending to obtain a quasi-plane wave condition at the entrance of the objective. A 100X apochromatic infinity-corrected objective with numerical aperture N.A. = 0.95 is used to direct the beam onto the sample. This enables an Airy intensity profile at the focal plane with $FWHM$ close to the theoretical diffraction limit: $FWHM = 0.515\frac{\lambda}{N.A.} \sim 0.55 \cdot \lambda$. The objective is equipped with a handle for the coarse movement along the z-axis, and a piezoelectric controller to finely focus the beam on the sample.

The sample is placed on a holder which is can be manually control for the coarse movements along the x-y directions, and is also connected to two piezoelectric actuators:

- one actuator enables the **raster scanning** of an area of 100 × 100 μm^2 with a resolution of 0.3 nm;
- the second enables the **modulation** of the sample's position **along one direction** (the y-axis in our reference) with tunable frequency f and amplitude δ_y.

The modulation signal is generated via a lock-in amplifier (LIA), typically at $f = 1.5$ kHz and $\delta_y \sim 300$ nm as optimal experimental conditions.

Once transmitted from the sample, the light is collected by a second 100X objective with numerical aperture N.A.' = 0.75 and sent to an avalanche photodiode. The LIA demodulates the signal collected from the photodetector at the desired frequency V_{LIA} and a digital multimeter (DMM) reads the time-averaged value V_{DMM}, necessary to obtain the normalized signal $\frac{\Delta P|_{2f}}{P_{inc}}$. Considering that the modulation of the signal given by the oscillation of the nano-object position is small, the approximation $V_{DMM} \simeq V_{inc,DMM}$ holds.

A software program enables signal collection from the LIA and the DMM and provides, for each position of the nano-object, an instantaneous value given by:

$$|\frac{\Delta P}{P_{inc}}|_{2f} = \alpha \cdot |\frac{V_{LIA}}{V_{DMM}}|$$

where α is a calibration factor that accounts for various instrumental effects, including the frequency-dependent gain $g(F)$ of the photodiode and multiplicative factors due to LIA demodulation. For this reason, the following relationship holds [142]:

$$\alpha = \frac{\pi}{\sqrt{2}} \frac{1}{g(2f)}$$

In the case of an ideal photodiode ($g(F) = 1$), this value is approximately 2.22.

This measurement is performed in the area surrounding the nanostructure, at a fixed wavelength and polarization of the beam, and with a spatial resolution chosen by the user. The amplitude of the signal is proportional to the extinction cross-section of the nano-object, which can thus be experimentally obtained. A schematic of the experimental setup is shown in Figure 2.3.

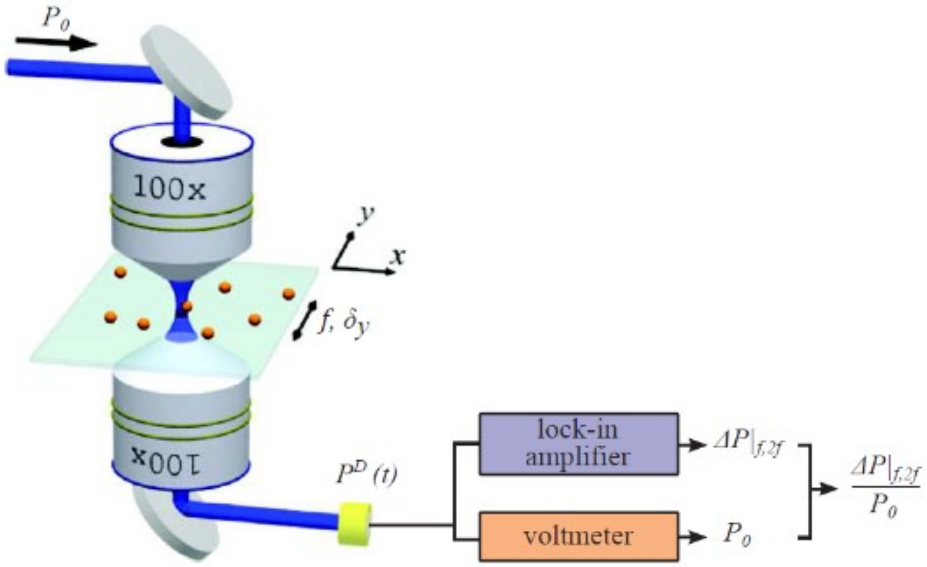

Figure 2.3: Schematic of the setup for SMS measurement. P_0 corresponds to P_{inc} in the main text. [141]

2.2 Extinction Spectroscopy

While SMS is employed in this work for detecting small nanostructures, ES is used for the localization (with respect to the center of the light beam used for the detection) of high aspect-ratio nanostructures whose longitudinal dimensions extend to the micrometer scale. In this work the technique was developed for the optical analysis of long MoS_2 NTs, whether suspended or supported on substrates, enabling the extraction of their extinction cross-section per unit length σ_L spectra (which will be discussed in detail in Chapter 4).

2.2.1 Working principle

This method enables the localization of nano-objects with respect to the center of the incident laser beam. Let us consider the case of MoS_2 NTs suspended over a trench in a PMMA layer, in turn supported by a sapphire substrate as illustrated in Figure 2.4.

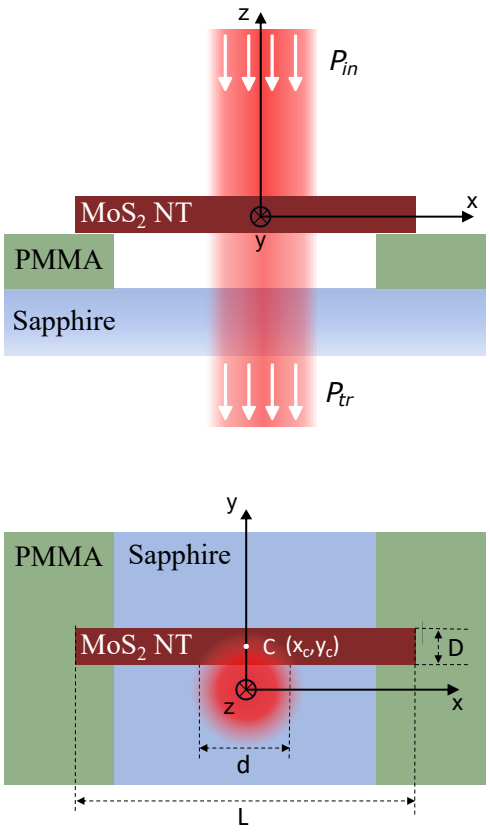

Figure 2.4: Pictorial view of the NT-based system in the suspended configuration during the ES measurement. Top panel illustrates the side view, showing incident and transmitted power as well as the defined reference coordinate system. Bottom panel shows the top view, highlighting the center of the NT and illustrating the movement of the sample beneath the fixed laser beam.

The sample is moved under a fixed laser beam of incident power P_{inc} and with a spot size of $FWHM = d$, obtaining a raster scan across the sample surface, while the transmitted power at each point of the area, $P_{tr}(x, y)$, is recorded.
The reference coordinate system is centered at the center of a fixed laser beam. For the NT, the x-axis and y-axis are aligned parallel and perpendicular to the NT axis, respectively, while the center of the NT is defined by the coordinates (x_C, y_C).
Since the power transmitted across the nano-object differs from its counterpart at the surrounding area, the nanostructure can be localized by detecting the change in transmitted power when the center of the laser beam coincides with the center of the nanostructure, i.e. when $x_C = 0$ and $y_C = 0$.

The technique also enables the retrieval of the extinction cross-section of the nanostructure under investigation. To this aim, only a single scan along the y-axis is required, with fixed $x_C = 0$ and y_C varying from $y_C = -\infty$ (i.e. $y_C << -d$) to $y_C = +\infty$ (i.e. $y_C >> +d$). $P_{tr}(y_C)$ indicates the transmitted power for each position y_C of the NT.

When the laser beam is completely on the substrate, the transmitted power is indicated as $P_{tr}(\infty)$.
In the case of nanostructures with dimensions exceeding the laser spot size, an extinction cross-section per unit surface, $\sigma_{ext}^{D,L}$, can be defined, where D and L represent the relevant geometric parameters of the nanostructure (i.e. diameter and length of the NTs).
To determine the extinction cross-section of the NT, the transmitted power has to be related to the power extinction due to the presence of the suspended nanostructure (i.e. NT, air gap, sapphire substrate) and the substrate. The transmitted power for the case of a laser beam centered completely on the substrate can be expressed as:

$$P_{tr}(\infty) = P_{inc}T_{sub},$$

where the substrate power transmission coefficient is represented by T_{sub}; differently, the transmitted power taking into account the presence of the nanostructure is:

$$P_{tr}(y_C) = P_{tr}^{NT}(y_C)T_{sub}$$

where $P_{tr}^{NT}(y_C)$ is the transmitted power across the NT. Using the Equation 2.1 it can be written as:

$$P_{tr}(y_C) = (P_{inc} - P_{ext}^{NT}(y_C))T_{sub}.$$

The transmittance of the substrate, T_{sub}, can be obtained from the power transmitted through the bare substrate $P_{tr}(\infty)$:

$$T_{sub} = \frac{P_{tr}(\infty)}{P_{inc}}$$

Thus, the expression can be rewritten as:

$$\frac{P_{tr}(y_C)}{P_{tr}(\infty)} = 1 - \frac{P_{ext}^{NT}(y_C)}{P_{inc}} \tag{2.2}$$

This equation is fundamental: it allow to address the NT extinction cross-section by measuring the quantity expressed by the first member.

Finally, it is important to clarify the relation between the extinction cross section per unit surface of the NT $\sigma_{ext}^{D,L}$ and the extinguished power at $x = x_C = 0$, for each position $y = y_C$ of the NT, $P_{ext}^{NT}(y_C)$. This expression reads as:

$$P_{ext}^{NT}(y_C) = \sigma_{ext}^{D,L} \times \int_{-\frac{L}{2}}^{+\frac{L}{2}} \int_{y_C-\frac{D}{2}}^{y_C+\frac{D}{2}} I_{inc}(x,y)\, dxdy, \tag{2.3}$$

where $I_{inc}(x,y)$ represents the intensity of a Gaussian beam:

$$I_{inc}(x,y) = \frac{P_{inc}}{2\pi(\frac{FWHM}{2\sqrt{2ln2}})^2} e^{-\frac{x^2+y^2}{2(\frac{FWHM}{2\sqrt{2ln2}})^2}} \equiv P_{inc} \cdot g(x,y) \tag{2.4}$$

In this expression, the function $g(x, y)$ accounts for the Gaussian profile of the beam. Substituting Equations 2.3 and 2.4 into Equation 2.2 yields:

$$\frac{P_{tr}(y_C)}{P_{tr}(\infty)} = 1 - \sigma_{ext}^{D,L} \times \int_{-\frac{L}{2}}^{+\frac{L}{2}} \int_{y_C-\frac{D}{2}}^{y_C+\frac{D}{2}} g(x, y)\ dxdy \tag{2.5}$$

and, by solving these integrals:

$$\frac{P_{tr}(y_C)}{P_{tr}(\infty)} = 1 - \sigma_{ext}^{D,L} \times \frac{1}{2} erf(\sqrt{ln2}\frac{L}{d}) \times \Big[erf\Big(\frac{\sqrt{ln2}(2y_C + D)}{d}\Big) - erf\Big(\frac{\sqrt{ln2}(2y_C - D)}{d}\Big)\Big] \tag{2.6}$$

D and L are known through preliminary morphological characterization, therefore d and $\sigma_{ext}^{D,L}$ are the remaining free parameters. This equation can therefore be used to fit the experimental data, allowing for the determination of $\sigma_{ext}^{D,L}$.
For the cases where the NT length L is much larger than the spot size d of the beam ($L >> d$), the function $erf(\sqrt{ln2}\frac{L}{d}) \sim 1$, making the fit function independent of L. The extinction cross-section per unit length σ_{ext}^{L} is then the relevant quantity for the analysis of the optical response of the NTs and it is calculated as $\sigma_{ext}^{D,L} \times D$.

This approach enables the extraction of the extinction cross-section per unit length for high aspect-ratio nanostructures, by experimentally measuring the transmitted power over an area that includes the nanostructure ($P_{tr}(y_C)$) itself and an area with the bare substrate only ($P_{tr}(\infty)$).

2.2.2 Experimental setup

To implement this technique, a dedicated experimental setup has been developed, as shown in the schematic in Figure 2.5.

As for the setup described in Section 2.1, a Ti:Sa laser serves as light source, providing an output power exceeding 2.9 W at a central wavelength of 800 nm. The laser's wavelength is tunable in the range of [690 ÷ 1040] nm. To extend the wavelength range, an automated OPO-SHG system is employed, allowing the system to span the wavelength from 340 nm (UV) to 1600 nm (far-IR). Again, to improve the signal-to-noise ratio, synchronous detection is employed. The laser beam, fixed at a selected wavelength, passes through a **mechanical chopper**, which modulates the light at a reference frequency f for a LIA. Then, the beam is expanded via a telescope (as shown in Figure 2.6a) and directed to a beam splitter:

I. **Main Beam Path**:
   The primary portion of the beam is directed toward the sample. It first passes through a polarizer, which ensures the desired polarization state immediately before the beam interaction with the sample. A 100X apochromatic infinity-corrected

objective, with numerical aperture N.A. = 0.70 and manual tunability, focuses the beam onto the sample. At the focal plane, the beam forms an Airy disk with an intensity profile and a $FWHM$ close to the diffraction limit, estimated as $FWHM = 0.74 \cdot \lambda$.

The sample is mounted on a micrometric stage equipped with two piezoelectric actuators. The first actuator enables fine movement along the x,y and z axis, facilitating a raster scan over an area of 100×100 μm^2. The second actuator permits oscillation along the y-axis, which is essential for SMS detection. This oscillation is not required for the ES technique, but the setup allows for an efficient switch between the two techniques. After interacting with the sample, the light is collected by a similar objective and directed to a silicon photodiode (PD1). The signal from PD1 is **demodulated by the LIA** at the chopper frequency f. The components referenced in the text are shown in Figure 2.6b.

II. **Secondary Beam Path**:

The remaining portion of the beam is directed to a second photodiode (PD2), with its output signal monitored by a DMM, providing a voltage proportional to the incident laser power (P_{inc}), and allowing to measure its fluctuations during the acquisition time of the experiment.

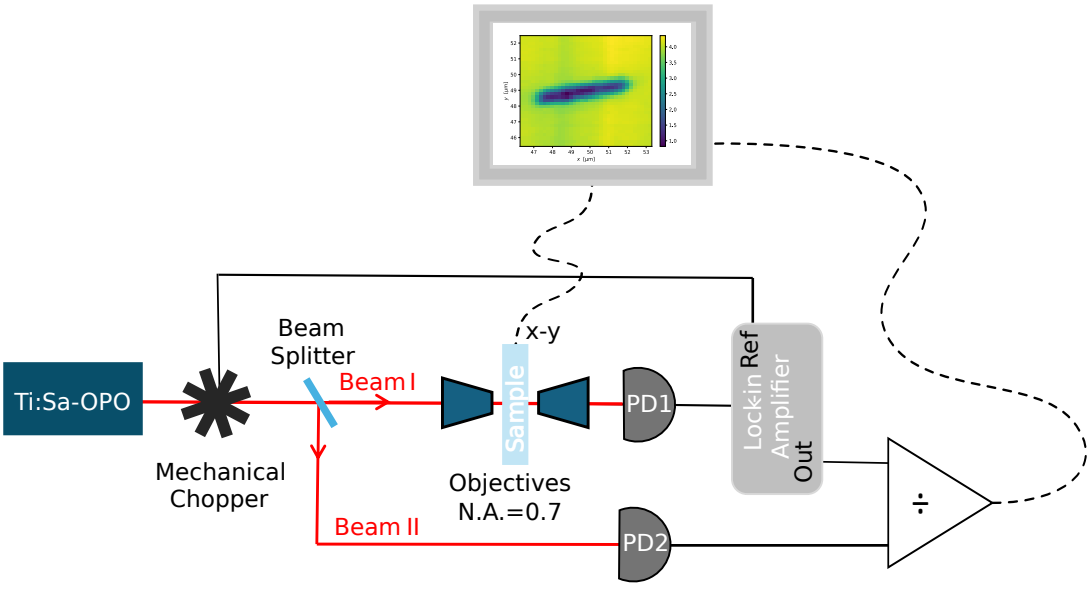

Figure 2.5: Conceptual schematic of the optical setup for Extinction Spectroscopy. Details of the set-up are discussed in the main text.

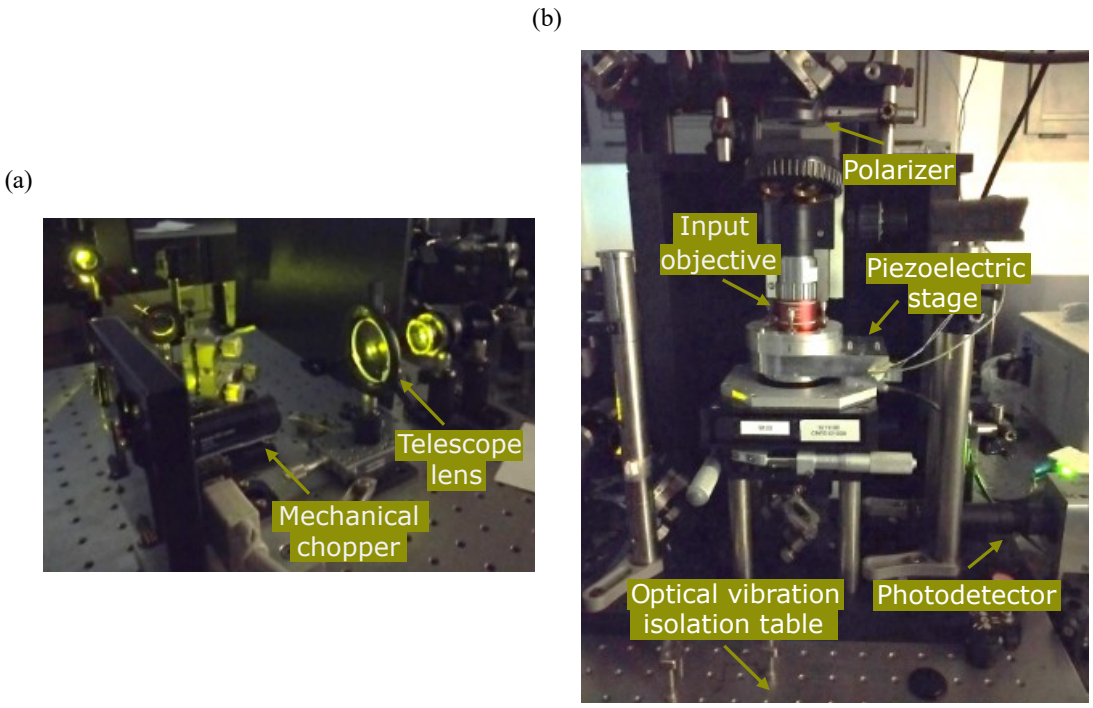

Figure 2.6: Elements of the optical setup used for ES experiment.

The output signals from the LIA, denoted as V_f, and the DMM, denoted as $V_{inc,DMM}$, are recorded using software that computes the instantaneous ratio $\frac{V_f}{V_{inc,DMM}}$. This ratio corresponds to the normalized transmitted power at specific spatial coordinates of the stage (x', y'), rescaled by a proportionality factor c:

$$\bar{P}_{tr}(x', y') = \frac{P_{tr}(x', y')}{c \cdot P_{inc}}$$

The use of synchronous detection in the transmitted signal enhances the signal-to-noise ratio, while the real-time ratio with the incident beam signal compensates for laser fluctuations, further improving measurement accuracy. A raster scan of the sample's surface is performed, resulting in maps similar to those shown in Figure 2.7.
In the real experiment, the NT may be not exactly perpendicular to the trench, and its orientation may be not orthogonal to the translational stage axis movement. Therefore, in order to apply the model described in the previous section for the retrieval of the extinction cross-section per unit length, the coordinate system defined in Figure 2.4 is superposed to the map in Figure 2.7, and a line-cut along the y-axis (i.e. the direction orthogonal to the NT axis) is extracted. Subsequent analysis allows for the determination of the absolute extinction cross-section per unit length as described in the previous section. The practical steps to achieve extinction cross-section per unit length from the fit of the line-cut are detailed in Chapter 4, in the framework of the actual measurements.

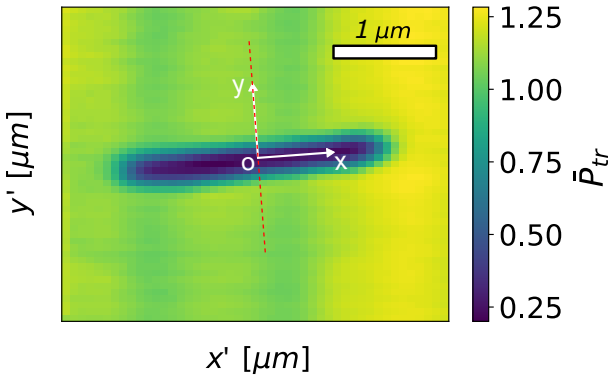

Figure 2.7: Example of a cartography obtained by ES technique on a MoS_2 NT with a length of $\sim$ 2.2 μm and a diameter of $\sim$ 120 nm, at a wavelength of 550 nm. In order to use the procedure for the retrieval of the extinction cross-section of the nanostructure, the coordinate system is redefined by the reference system centered on the nanostructure, with the y-axis corresponding to the axis of the nanostructure.

Finally, this technique provides a way to assess the orientation of the longitudinal axis of the nanostructure. The polarizer placed before the input objective is typically used to measure the polarization dependence of the transmitted power $\bar{P}_{tr}(x', y')$. Fitting this polarization plot provides the angle required to align the beam polarization parallel to the NT axis henceforth for any desired polarization. This measurement has been preliminarily performed before every linear or time-resolved optical analysis reported in this thesis.

2.3 Ultrafast Time-Resolved Spectroscopy

Ultrafast Time-Resolved Spectroscopy (US) is an optical technique that, through the combination of femtosecond laser sources and the pump-probe method, enables the study of ultrafast dynamics occurring, in the present case, in a timescale from the 100 fs to a few nanoseconds. This technique is non-invasive, as it is entirely contactless due to the use of optical excitation and probing, and it is low perturbing thanks to the use of low-power, high-repetition rate probe pulses. This allows avoiding the shortcomings typical of contact probes. Indeed, on the thermal side, contact probes introduce additional thermal resistances in series to the one to be measured. Additionally, the contact probe thermal capacitance adds up to the nano-sample one, thus biasing the measurement of the thermal transient. On the mechanical side, a contact probe affects the nanosystem eigenmodes and their damping toward the environment. The fast energy delivery, occurring on the sub-ps time scale, and the fast time-resolution of the probe process, spanning from the

sub-ps to the ns time scale, are particularly well suited to trigger and follow the mechanical and thermal transients that, for a nanoscale to mesoscale object, occur on these characteristic time-scales. Consequently, all-optical pump and probe techniques are particularly well-suited to investigate energy transients (both mechanical and energy ones) at the nanoscale. In this work, after carefully identifying the position of the nanostructures via SMS or ES, and, for the case of MoS_2 NT, after detecting its electromagnetic cross-section, the US technique is employed to investigate the mechanisms ruling the transient mechanical energy transfer processes in MoS_2 NTs (Chapter 4) and the mechanical and thermal energy transfer processes in InAs NWs (Chapter 5).

2.3.1 Working principle

The US technique is based on the pump-probe method, which utilizes two spatially overlapping and time-delayed femtoseconds (approximately 150 fs) laser pulses to perform the time-resolved analysis of phenomena occurring in the nanostructures.

- **Pump pulse**:
  This is the first pulse that interacts with the system, initiating an out-of-equilibrium state by transferring a specific amount of energy ΔU. This energy is imparted to the system in the form of heat (ΔQ) and work (ΔW). Consequently, concerning the thermal and acoustic phenomena of interest in this work, the temperature Θ of the system increases, and the vibrational eigenmodes u_j are excited. Both phenomena manifest as changes in the optical properties of the system via the complex dielectric function of the system:
  $$\tilde{\varepsilon_j}(t,x) = \tilde{\varepsilon_{j,0}} + \frac{\partial \tilde{\varepsilon_j}}{\partial \Theta}\Delta\Theta_j(t,x) + \frac{\partial \tilde{\varepsilon_j}}{\partial u}\Delta u_j(t,x) \tag{2.7}$$
  The time variation of $\tilde{\varepsilon_j}$ thus entails information on the thermal and energy transfer. This quantity depends on time t and space coordinates x, and rules the optical transmission coefficient T of the system. Therefore, the energy transients triggered by the pump pulse result in a time variation of the transmission coefficient of the system, which is exactly the physical quantity experimentally addressed.

- **Probe pulse**:
  This is the second pulse that reaches the system with a variable delay relative to the pump pulse, and its purpose is to *probe* the transition of the system from the out-of-equilibrium state back to equilibrium. Consequently, the transmitted portion of this pulse is measured at various instants following the excitation, providing information on the pump-induced change in the transmission of the system in relation to the equilibrium state, denoted as ΔT, over time.

Finally, the signal $\Delta T(t)$ is analyzed using the theoretical models described in Chapter 1 to correlate it with the underlying physical vibrational and thermal relaxation dynamics.

2.3.2 Experimental setup

The optical setup used for the US experiments is a two-color pump-probe spectroscopy configuration, obtained by modifying the setup described in Section 2.1, as shown in Figure 2.8.

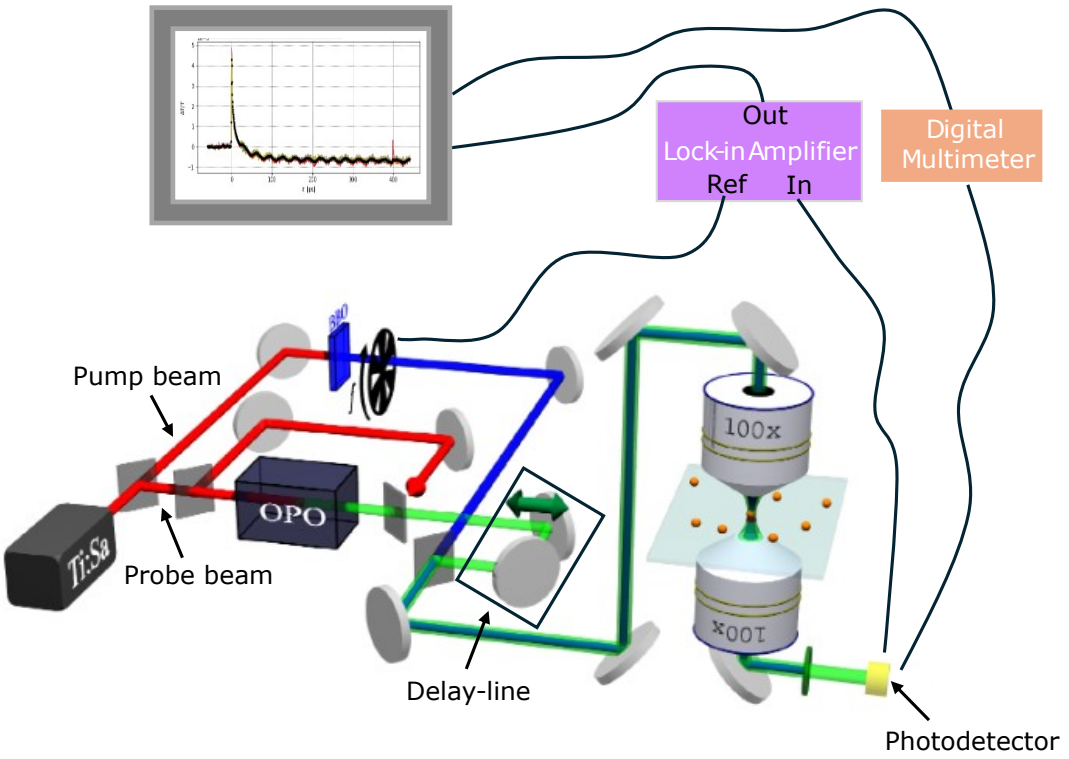

Figure 2.8: Schematic of the experimental setup for ultrafast pump-probe spectroscopy on single nanostructures. [141], adapted by the author.

The same Ti:Sa femtosecond laser source is employed (producing 150 fs wide pulses at 80 MHz repetition rate) with its wavelength emission range expanded by both the OPO and the BBO crystal for nonlinear frequency conversion. In this experiment, two beams are required, serving as the pump and probe beams. To generate these beams, the output from the Ti:Sa oscillator is split as follows:

- The **pump** beam, with a wavelength of 820 nm, is directed towards the BBO crystal, where second-harmonic generation (SHG) converts it to 410 nm. Afterwards, the beam's spot size is expanded using the telescope, and it passes through a **mechanical chopper** rotating at a specific reference frequency $f = 30$ kHz, which synchronizes the modulation of the pump with the LIA for phase-sensitive detection.

- The **probe** beam undergoes further division to enable wavelength selection. One fraction of the probe beam is sent through the OPO for wavelength conversion, providing tunability across the visible spectrum $\lambda_{pr} = [500 \div 750]$ nm while the other fraction remains unaltered. This division allows flexibility in choosing the probe wavelength that maximizes the sensitivity to the system under investigation. Only one of these two beams is ultimately used as the probe.
  The selected probe beam is directed through a mechanical **delay line**, which consists of an electronically controlled motorized linear translation stage equipped with a fixed mirror and a movable mirror. The movement of the mirror adjusts the optical path length of the probe beam, effectively varying the time delay t between the pump and the probe beams during the experiment. This delay time is crucial for time-resolved measurements, enabling precise control over the temporal overlap of the two beams. The mechanical delay line is shown in Figure 2.9a.

(a)

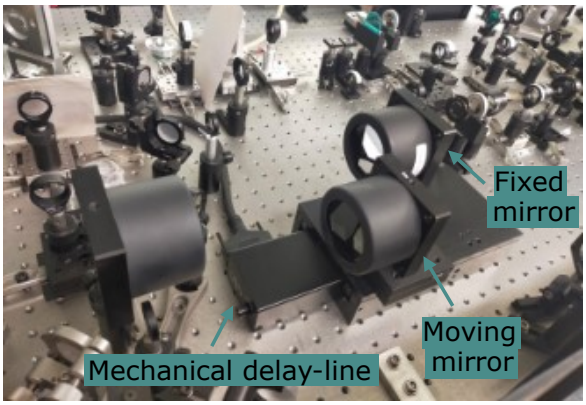

(b)

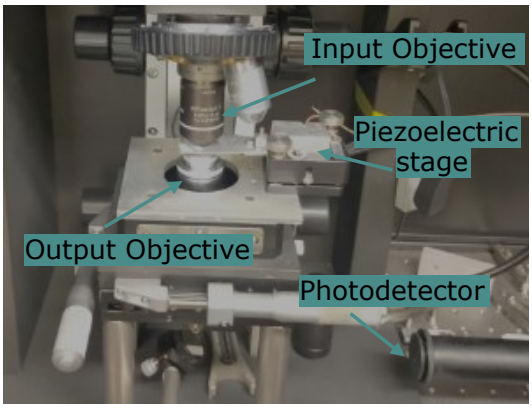

Figure 2.9: Photographs of the experimental setup used in the US experiments. (a) Mechanical delay line. (b) Piezoelectric stage, input and output objectives and avalanche photodetector protected by long-pass filters.

After passing through the delay line, the pump and probe beams are spatially recom-

bined and tightly focused onto the individual nanostructure through the same objectives described earlier and shown in Figure 2.9b. Long-pass optical filters are placed in front of the avalanche photodetector to block the 410 nm pump beam and ensure that only the probe beam reaches the detector, allowing for accurate measurement of the probe's interaction with the sample.

The signal from the photodetector is then directed to both a LIA and a DMM. The LIA demodulates the signal at the chopper frequency, enabling the detection of the sole transmission change ΔT induced by the pump pulse. Conversely, the DMM measures the total transmission of the probe beam, which is $T = T_0$ when the system is in equilibrium (i.e. before pump excitation) and $T = T_0 + \Delta T$ during the out-of-equilibrium state induced by the pump. Since $\Delta T << T_0$, in the low perturbation regime, the approximation $T \simeq T_0$ holds at all times.

For each time delay between the pump and the probe pulse, the experimentally measured quantity is $\frac{V_{f,LIA}}{V_{DMM}}$, which represents the **transmission change induced by the pump, normalized by the equilibrium transmission** $\frac{\Delta T}{T}$. Indeed, this can be expressed as:

$$\frac{\Delta T}{T} = \alpha \frac{V_{f,LIA}}{V_{DMM}}$$

where α is a proportionality factor similar to the one discussed in Section 2.1.2.

Notably, a set of ancillary measurements is required to ensure a good outcome from the entire experiment.

A procedure is required to ensure the **spatial overlap** of the two beams. This is achieved using one of the previously described imaging techniques (SMS or ES). For samples containing nanostructures with a length $L >> FWHM$, small nanoparticles - typically fragments from the same material - located near the target nanostructure are used to facilitate precise x-y alignment. In the case of nanostructure with $L \leq FWHM$, the nanostructure itself is used for the alignment. The pump and probe beams alignment process first begins with a coarse adjustment of the beams' position using iris diaphragms. **Fine-tuning** of their spatial overlapping is then carried out by scanning the nanoparticle under the first beam, recording the position of the nanoparticle with respect to this beam, and subsequently scanning under the second beam. The center of the second beam is then aligned to the recorded position via micrometric adjustments using the fine movement screws of the injection mirrors, which both control the beam angle and position.

After the pump-probe beam overlapping procedure, the nano-object needs to be precisely aligned under the center of the beams Gaussian profiles. This is achieved using one of the two detection techniques described earlier (SMS or ES), depending on the specific characteristics of the nanostructure. This alignment between the center of the beams and

the nanostructure must be checked at different stages of the measurement, depending on the sensitivity of the signal with respect to small movements of the stage dictated by the environmental conditions. To minimize this risk, both sample holder and objectives are enclosed into a chamber that remains closed during the experiment, to enhance thermal stability. This reduces the impact of temperature fluctuations in the experimental room. Additionally, the ambient temperature of the laboratory is carefully regulated to ensure stable experimental conditions.

These alignments are essential when investigating high aspect-ratio nanostructures, for which distorted signals can be easily produced when the pump and probe beams are only slightly spatially separated.

Chapter 3

Synthesis methods and morphological characterization

This chapter describes the experimental method used to grow nanostructures, fabricate the samples, and characterize them. In Section 3.1 the processes used to grow the different nanostructures on which this study is focused are addressed. In Section 3.2, the fabrication protocol developed to obtain the single nanostructures in a system suitable to be studied in an optical setup working in transmission mode is described. Each type of nano-object is addressed in three different configurations: suspended over a trench, supported on PMMA, and supported on sapphire. Their morphological characterization is reported in Section 3.3.

3.1 Nanostructures growth

This work focuses on multilayer MoS_2 NTs (Subsection 3.1.1) and wurzite InAs NWs (Subsection 3.1.2). Their different morphological properties allow the complete analysis of both the mechanical and thermal energy transfer happening in different geometries, such as the cylindrical shell (nanotubes) and the full cylinder (nanowires). The MoS_2 NTs used in this work were synthesized by the research group of Prof. Alla Zak (Department of Physics, HIT- Holon Institute of Technology, Holon, Israel), while the InAs NWs were grown by the group of Prof. Lucia Sorba (NEST, Istituto Nanoscienze - CNR and Scuola Normale Superiore, Pisa, Italy).

3.1.1 MoS_2 Nanotubes

The MoS_2 NTs investigated in this work are multiwall NTs with inhomogeneous diameters along their length, with average values in the range of ~ 220 nm and ~ 120 nm, and

lengths in the range of $[0.5 \div 3.6]$ µm. They are grown by a multi-step mechanism [27] having place in an appositely designed horizontal reaction system, provided with a split furnace, a quartz tube and a porous-quartz reaction cell, as depicted in Figure 3.1.

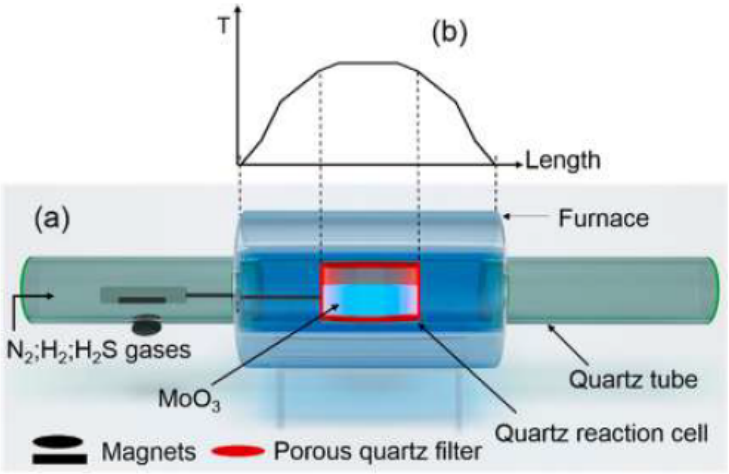

Figure 3.1: (a) Pictorial view of the horizontal rector employed for the growth of MoS_2 NTs. (b) Temperature profile along the furnace. [27]

The growth mechanism of these MoS_2 NTs is based on two stages, that are schematically depicted in Figure 3.2.

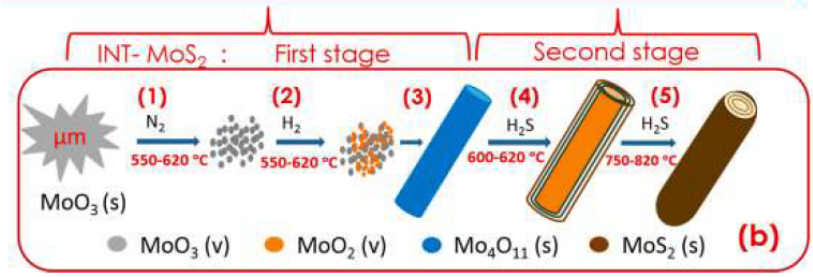

Figure 3.2: Schematic of the NTs growth process. [27]

The *first stage* is dedicated to the growth of **oxide nanowhiskers.** The temperature is controlled along the furnace to achieve a flat temperature zone with a precision of ± 2 °C. The precursor MoO_3 powder is placed out of the hot zone in the reaction cell. After the temperature is stabilized at 500 °C a N_2 gas used as a carrier spreads in the reactor for 30 min to obtain an inert oxygen-free atmosphere. Under an inert atmosphere, the precursor sublimes into molecular clusters. Then, a gas mixture of N_2 and H_2 is injected with a flow rate of 1 cm^3/min tuned by electronic mass flow controllers, regulated by a programmable logic controller. Reacting with the H_2 part of these clusters reduces

into MoO_2 or MoO_{3-x}. Being these compound clusters non-volatile at this temperature, they initiate the nucleation for the rest of the clusters which will collide with them. The precursor powder (inside the reaction cell) is moved in the hot zone with the help of magnets, so the growth of MoO_3 nanowhiskers takes place. This aggregation leads to the growth of Mo_4O_{11} elongated crystals, which are here called nanowhiskers. The dimensions can be adjusted by varying the reaction parameters (gas flow, temperature, and time). At the end, the cell is moved out and the furnace is cooled to room temperature under N_2 flow.

The *second stage* of this growth process is devoted to the **sulfurization** of the nanowhiskers into MoS_2 NTs. To avoid the nanowhiskers collapsing into 3D crystallites, this process is divided into two phases to gradually increase the temperature (from 600-620 °C to 750-820 °C). Similarly to the first stage, the whiskers react with the H_2S injected at a 100 cm^3/min flow rate: the sulfurization process starts at the surface, where a few external coaxial layers of MoS_2 grow, contemporary the molybdenum sub-oxide core reduces to MoO_2. Afterwards, the temperature is increased, allowing the sulfurization to proceed to the oxide core through inward diffusion of the gas through the defects of the external layers. The oxide-to-sulfide reaction proceeds epitaxially, and thanks to the significant difference in densities between MoS_2 and Mo_4O_{11}, the highly crystalline hexagonal MoS_2 NTs with hollow cores are formed (Figure 3.3).

The nanostructures' morphology is analyzed via SEM imaging (Figure 3.3a). The presence of a hollow core is statistically confirmed in NTs within their large dispersion in diameter (from 40 nm to 220 nm). A TEM micrograph showing the hollow core is reported in Figure 3.3b. Eventually, the nanostructures are analyzed via X-ray diffraction (XRD), to confirm their 2H-MoS_2 crystal structure (Figure 3.3c).

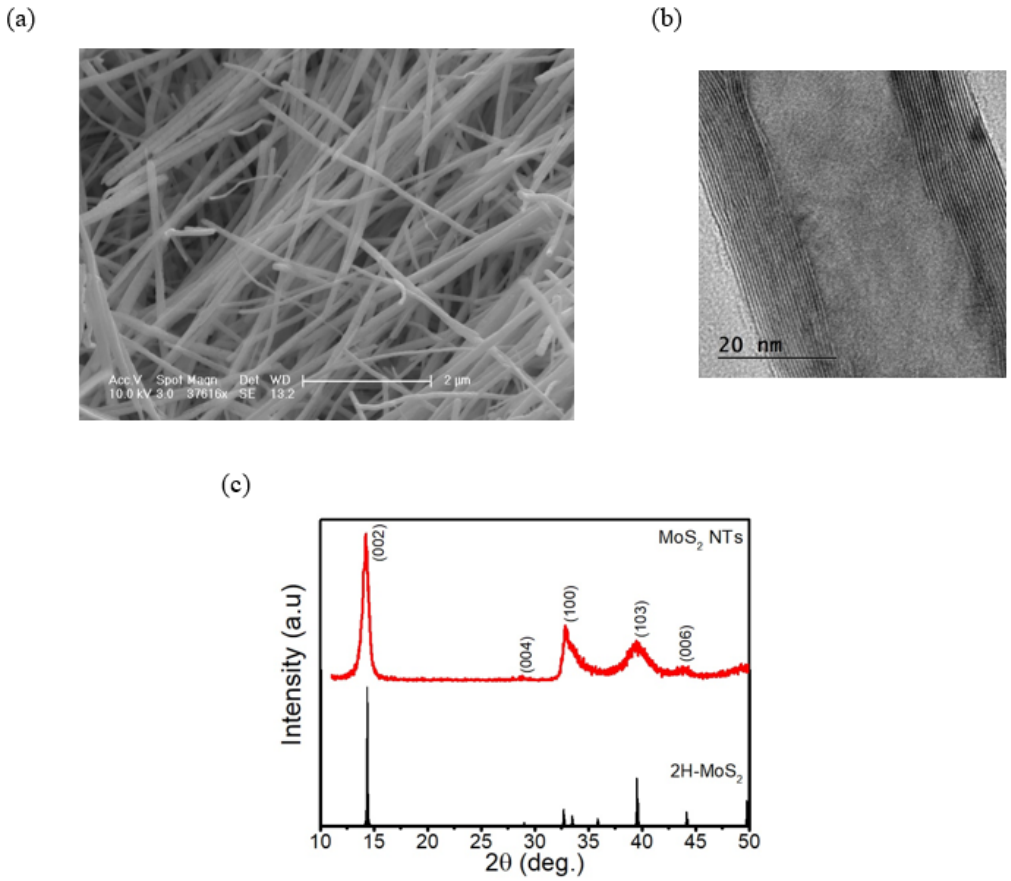

Figure 3.3: NTs characterization. (a) SEM micrograph of the MoS2 NTs batch at the end of the growth process. (b) TEM micrograph of an NT belonging to the batch, showing a hollow core. (c) XRD analysis, confirming the overall 2H-MoS_2 crystal structure.

3.1.2 InAs Nanowires

One of the most powerful techniques dedicated to the growth of semiconductor nanowires is the **Chemical Beam Epitaxy (CBE)**. This technique allows the bottom-up growth of single-crystal semiconductors by layer-by-layer depositing the proper chemical compounds in an epitaxial fashion.

In this work, two types of NWs are studied:

- InAs NWs type L: a batch of $\sim$ 6 µm long and 100 nm diameter NW, tapered at their extremities and undoped. Their crystal structure is WZ, with a low density of stacking faults.
- InAs NWs Type S: a batch of $\sim$ 550 nm long and diameters in the range [50 - 80] nm. Their crystal structure is WZ with stacking faults.

Both NW samples are grown in a CBE Riber Compact-21 system by the Au-assisted

Vapor-Liquid-Solid (VLS) method. This is a well-known growing technique for obtaining size-controlled nanostructures with a high aspect ratio.

A schematic view of the CBE system is shown in Figure 3.4a.

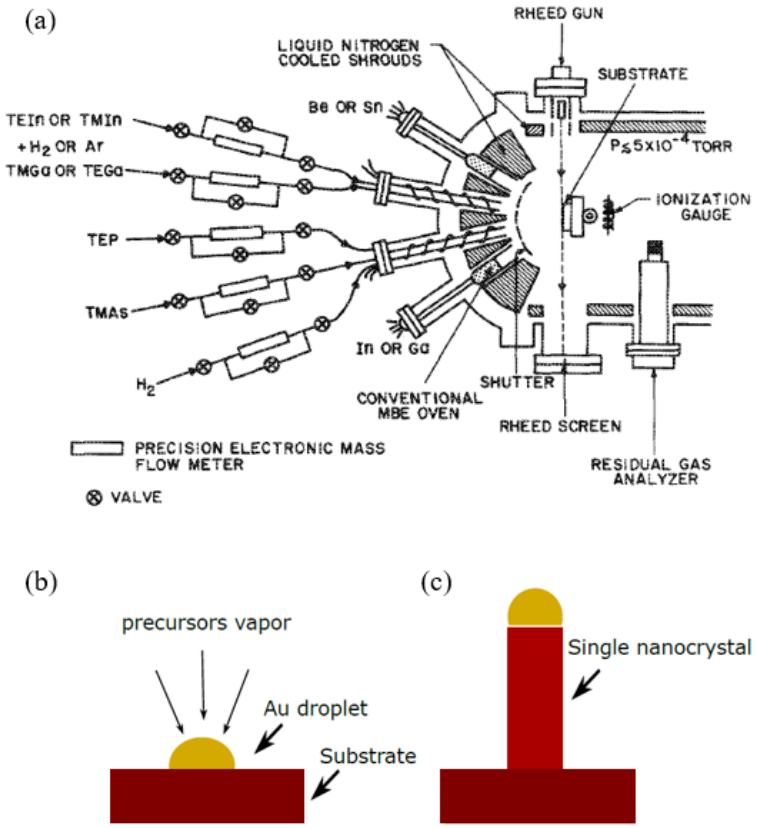

Figure 3.4: NW growth by VLS method in CBE system. (a) Schematic of the main components in a CBE equipment. [143] (b) Pictorial view of the VLS procedure.

The system is equipped with a high-vacuum growth chamber with a gas handling system linked to individual heated cells which are dedicated to the production of precursor molecules of the targeted material. Each cell has an individual line pressure and shutters to allow or stop the flow inside the chamber. Both NW batches are grown on an InAs(111)B substrate. The VLS technique exploits the presence of metallic liquid droplets on the substrate as a catalyst for the growth reaction (Figure 3.4b). A 0.1 nm thick Au film (0.5 nm thick for sample (S)) is deposited on the surface by thermal evaporation, and the substrate is placed in the high-vacuum chamber of the CBE. In order to trigger the Au dewetting, a thermal annealing of the substrate is performed at a temperature of (490±10)°C for 20 minutes under tert-butylarsine (TBAs) flux at line pressures of 1 Torr. Once the shutter is open, the pyrolyzed chemicals impinge on the heated growth substrate as a molecular beam. When the precursor in the vapour phase reaches the Au catalyst,

the droplets absorb it and reach a supersaturation state that leads to the precipitation and nucleation of the semiconductor at the solid/liquid interface. The NWs forests are grown at (420±10)°C for 50 minutes under trimethylindium (TMIn) and TBAs at a line pressure of 0.6 Torr and 2.4 Torr, respectively ((369±10)°C for 45 minutes at 0.3 Torr and 0.4 Torr for the sample (S)), as in Figure 3.4c. Sample (L) is placed under the metal-organic precursors flux for 30 minutes while linearly increasing the temperature and line pressure (this last one from 2.4 Torr to 3.4 Torr). This allows the NW to grow up to a length of approximately 6 μm, while the sample (S) is stopped at about 550 nm length. In the end, the flux is stopped and the forests are cooled down to room temperature.

The morphology of the NW forests is analyzed by a Zeiss field-emission Scanning Electron Microscope (SEM) operated at 5 kV and shown in Figure 3.5.

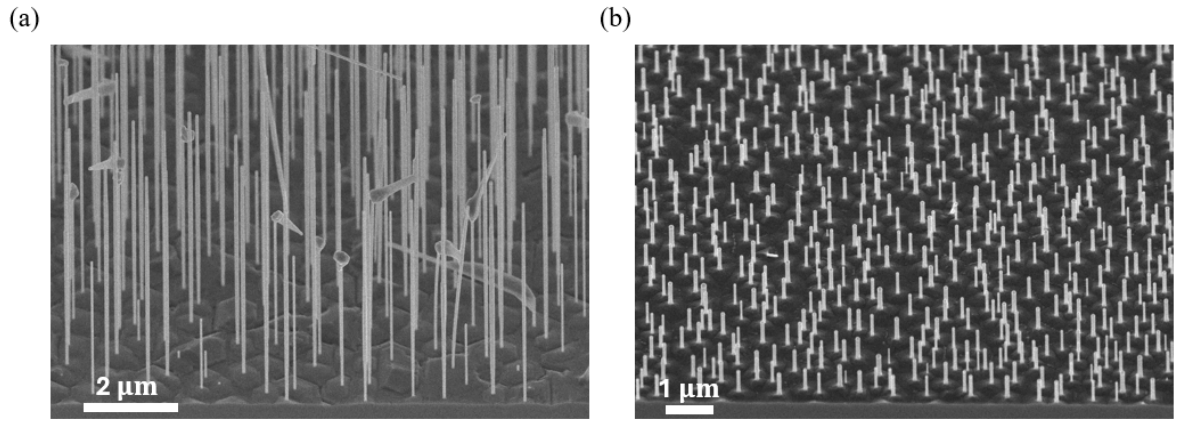

Figure 3.5: SEM micrographs of forests of InAs NWs from the batch L (a) and S (b).

The crystalline quality of selected NWs is characterized by High-Resolution Transmission Electron Microscopy (HR-TEM) and Electron Diffraction (ED). The results of these analyses are reported in Figure 3.6. Panels (a) and (b) show HR-TEM images of NWs-S with different diameters in the range $[51 \div 77]$ nm, as the NWs investigated later in this work by optical spectroscopy, while panels (c) and (d) show images of a NW-L taken at different locations. HR-TEM analysis reveals, in both NWs-S and NWs-L, the presence of structural defects known as stacking faults. These are planar defects that occur when the dominant stacking sequence of crystal layers is disrupted, e.g., because of the growth of a few atomic layers with ZB structure within a NW with WZ structure. Stacking faults appear as contrast lines perpendicular to the growth direction. In both cases, the stacking faults are more concentrated at the base of the NWs and progressively decrease in density toward the tip. Variations in defect density are observed, tentatively ascribable

to differences in the growth conditions at the local nucleation sites of individual NWs. The predominantly WZ crystallinity of the NWs is confirmed by the representative ED pattern shown in panel (e), which corresponds to a section of the representative NW-L along the [2,-1,-1,0] WZ zone axis, free of stacking faults.

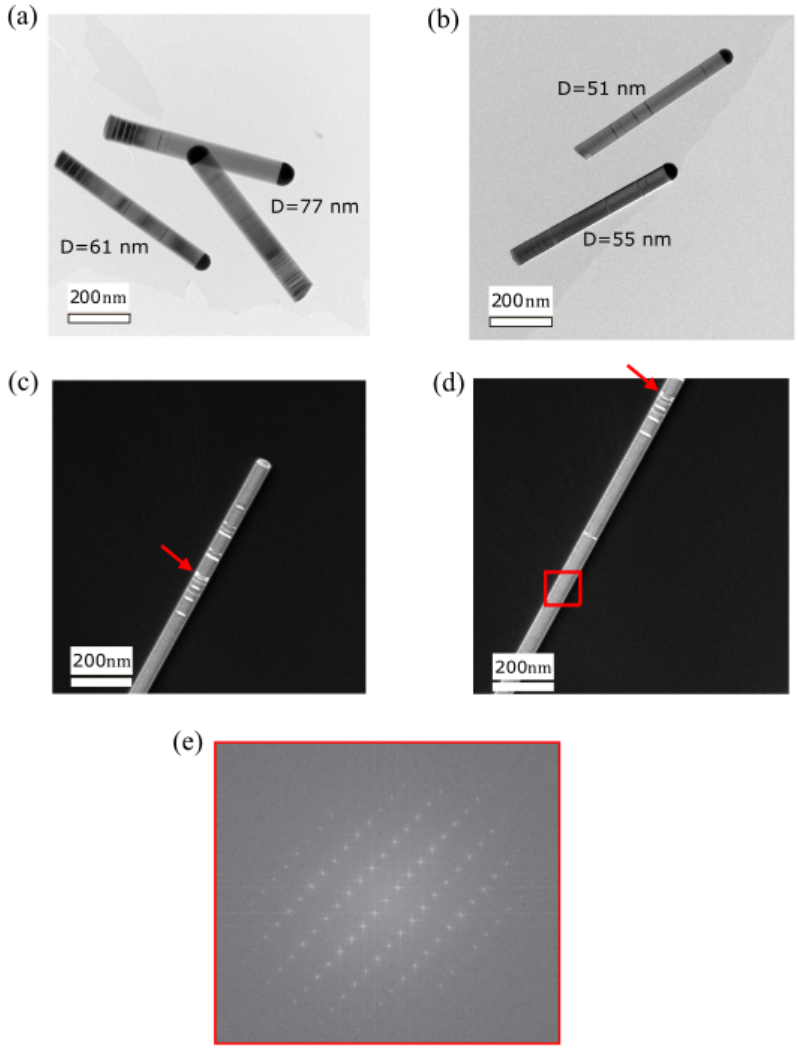

Figure 3.6: HR-TEM analysis for NWs-S (a, b) and NWs-L (c, d) and ED analysis (e). Panels (a) and (b) show NWs-S with varying diameters (ranging from 51 nm to 77 nm), showing the gradual concentration of stacking faults from the base to the tip. Panels (c) and (d) illustrate different sections of the same NW-L, with the red arrows marking the locations of the same stacking fault in both images. The stacking faults in NW-L are primarily concentrated at the base of the NW, leaving the rest of its length almost defect-free. Panel (e) displays the ED pattern acquired along the [2,-1,-1,0] WZ zone axis from a stacking-fault-free section (highlighted by the red rectangle) of the representative NW shown in panel (d).

3.2 Fabrication protocol for optical investigation of single nanostructures

This research focuses on the study of individual nanostructures in different configurations utilizing the optical techniques described in Chapter 2. The use of these techniques requires the nanostructures to be deterministically and suitably positioned onto the measurement substrate. Consistently, a fabrication protocol has been developed to realize a system fully transparent at the wavelength of interest [440 ÷ 940] nm, by minimizing the amount of metal used in the fabrication process and allowing for the control of the experiment at the single nanostructure level. The most challenging configuration involves the use of nanostructures suspended over a trench in the substrate, which enables the study of energy transfer disentangling the impact of the substrate from the actual response of the nanostructure.

The fabrication process involves three main steps:

1. Preparation of a pattern of metallic **markers** to serve as references fo precisely localize individual nanostructures under an optical microscope, for subsequent optical experiments;

2. realization of **arrays of trenches** in the substrate, to serve for developing suspended nanostructure devices.

3. Positioning of **individual nanostructures** over the measurement substrate.

Considering the dimensions of the nanomaterials used in this work, these steps rely on the use of scaning electron microscopes for material imaging and Electron Beam Lithography (EBL) for device fabrication.

Step 1. A 10 x 10 mm^2 sapphire substrate (square shape), 0.48 mm thick and with (0001)K(1120) crystal orientation serves as the substrate. It is subjected to a 1-minute baking process to eliminate potential humidity. Then, it is spin-coated with a positive polymethyl methacrylate (PMMA)-based **electronic resist** (AR679.04) at 4000 rpm for 1 minute, followed by a 1.30-minute prebake at 170 °C. This procedure facilitates the removal of solvent residuals, thereby enhancing adhesion to the substrate. Subsequently, a layer of a polyaniline-derivative-based **conductive coating** (AR5090) is spin-coated at 4000 rpm for 1 minute and then baked for 1 minute at 100 °C. The utilization of a conductive polymer as a top layer is crucial for facilitating the dissipation of charges during electron exposure when employing insulating substrates. Eventually, an oblique line is etched at the corners of the square to create reference markers for the following processes involving the precise control of the electron beam positioning onto the sample.

The array of markers is preliminarily designed via ELPHY Multibeam, a software for the preparation of **Computer-Aided Design (CAD) projects**, as depicted in Figure 3.7 .

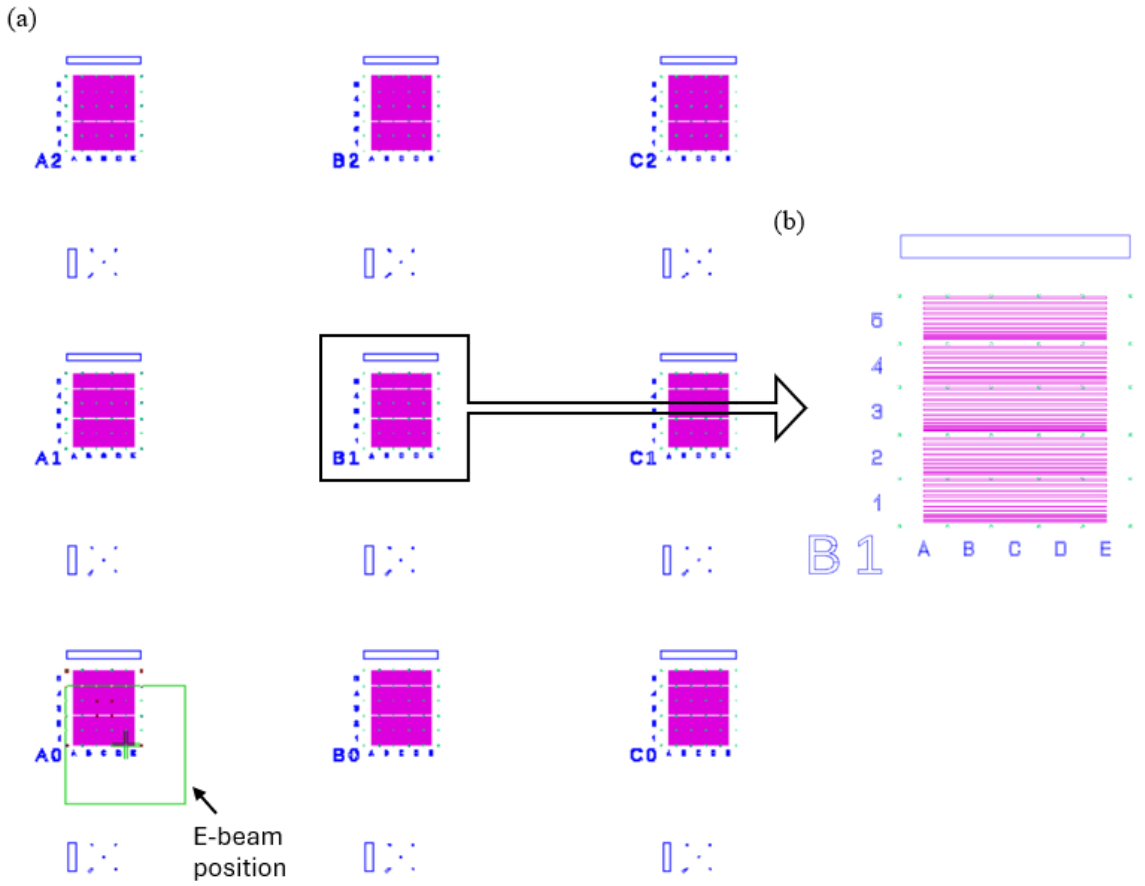

Figure 3.7: CAD project designed for the patterning of the markers mask (in blue and green) and the trenches sequences (in pink).

The CAD enables the precise design of patterns at the nanometric scale. The CAD project is then translated into instructions for the pattern generator, which after beam calibration scans the beam onto the sample surface following the CAD coordinates, thus exposing the designed pattern. This marker mask is crucial to allow the precise identification and positioning of individual nanostructures and the use of different magnifications. Two layers of markers are patterned in two separate steps, corresponding to markers with sizes of the order of 10 nm and 1 micrometer.

The prepared substrate is positioned on the sample holder of a Raith Ultraplus System equipped with an interferometric stage, inside the high vacuum environment characteristic of the EBL chamber. The two layers-patterning is directly written on the sample's surface via an electron beam with 20 V Electron High Tension (EHT), 10 (60) nm aperture and

310 μC/cm^2 dose used on a 200 (800) μm write-field (Figure 3.8a).

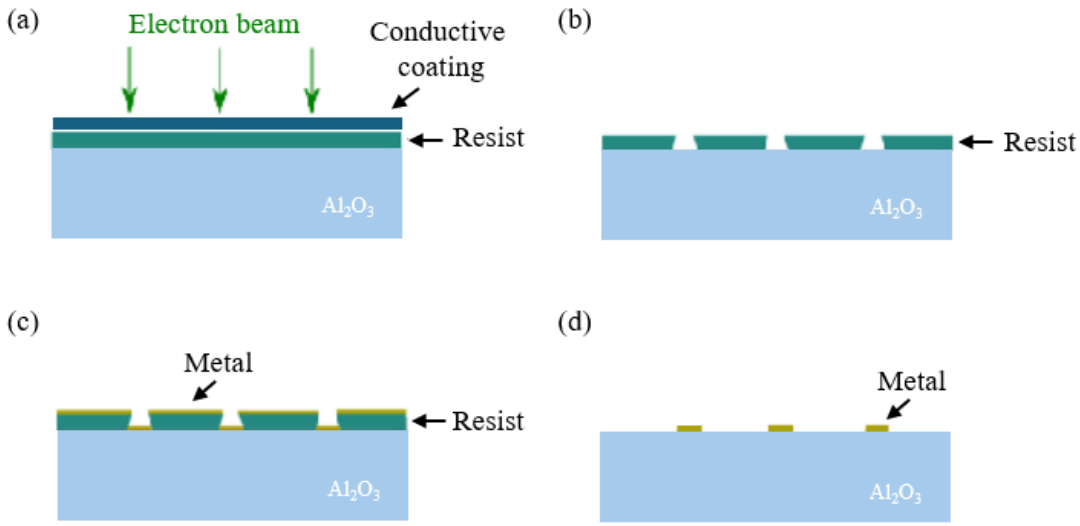

Figure 3.8: EBL procedure. (a) After spinning and baking a two-layer electronic resist/conductive coating, the sapphire substrate undergoes electron beam exposure. (b) The development step allows removing the electron-modified part of the resist. (c) A Ti/Au bilayer is deposited by thermal evaporation. (d) The lift-off process allows removing the remaining part of the resist together with the metal excess, resulting in the pattering of a metallic mask on the sapphire substrate.

During the **exposure** step, the high energy electrons impinge on the resist, breaking the chemical bonds in their polymeric chains, and provoking a change of the resist solubility in specific solvents. After exposure, the sample is rinsed in deionized (DI) water for about 1 minute to remove the conductive polymer. Then it is socked in a developer (a methyl isobutyl ketone-based solution, AR600-56) for 1 minute to dissolve the modified resist (Figure 3.8b). Then the sample is rinsed in isopropyl alcohol (IPA) and dried under nitrogen flux. Eventually, a plasma etching with a power of 30 W is performed for 1.15 minutes, to remove possible contaminants remaining from the previous fabrication processes. This step is intended to ensure a good outcome in the precision of the lithographic process.

Subsequently, a Ti/Au bilayer 5/50 nm thick is deposited on the sample via **thermal evaporation** (Figure 3.8c). The technique is based on the Physical Vapour Deposition (PVD) concept, typically used for thin-layer depositions.

After metal evaporation, the sample undergoes the **lift-off** process. This consists of a 5-minute soaking in acetone (ACE) heated at 50 °C temperature, to chemically dissolve the resist, followed by its mechanical removal using the ACE jet of a syringe.

This procedure allows *lifting* the metal from the locations where the resist is still present, resulting in the patterning of the metallic marker mask (Figure 3.8d).

The sample imaged at the end of this step is shown in Figure 3.9.

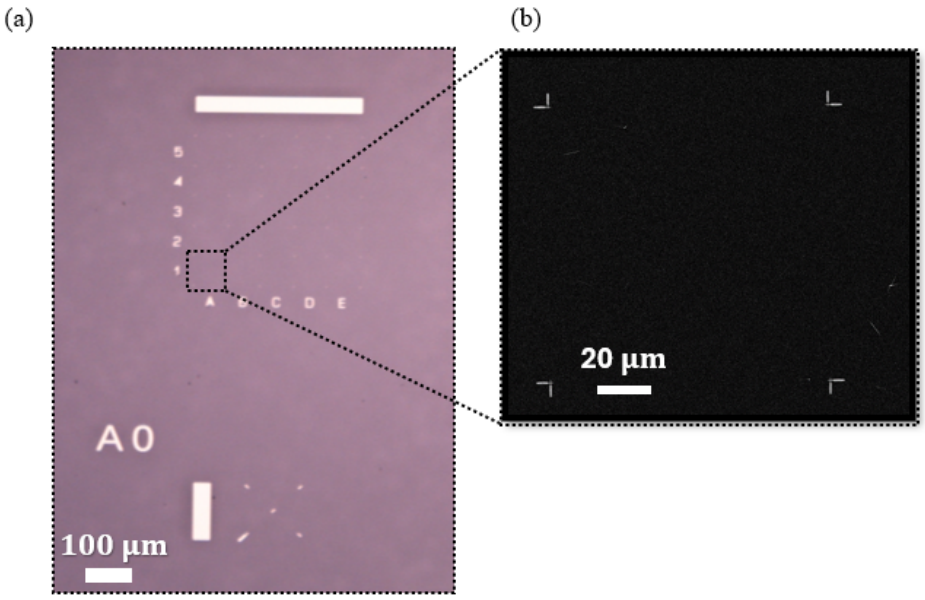

Figure 3.9: (a) Optical image showing part of the substrate after the first stage of lithography. (b) SEM micrograph showing a zoom on the smaller markers.

Step 2. Once the reference mask is ready, a second lithographic step is required for the realization of 270 nm deep trenches. As in step 1, the sample is baked to remove the humidity, then spin-coated and baked with the electronic resist and the conductive polymer. The CAD project is modified to add another project layer to position series of trenches with a width variable in the range of $[0.3 \div 5]$ µm on the reference mask. The EBL procedure is performed using a 20 V EHT electron beam, with 60 nm aperture and 310 $\mu C/cm^2$ dose. After the exposure, the sample is rinsed in DI and socked in the developer for 1 minute, then it is rinsed in IPA and dried under nitrogen flux, and a plasma etching with 30 W power for 1.15 min is performed. Eventually, in some cases, the sample is post-baked for 30 minutes at 150 °C to improve the PMMA stability. This step was advantageous in the case of long NWs and NTs, while it was not needed in the case of short NWs.

Step 3. This last step is dedicated to the deposition of nanostructures on the sample, by **drop-casting** technique. For InAs NWs, the Indium layer which covers the bottom of the growth substrate is removed to avoid excessive residuals in the solution. Then the NW forest is soaked in IPA. For MoS_2 NTs, the nanostructures are diluted in Ethanol. Preliminary tests have been performed to choose the right concentration in the solvent

that allows obtaining spatially separated nanostructures (approximately 1 μm apart) through drop cast on a substrate. Therefore, the solution containing the nanostructures is sonicated for 2 minutes and droplets of volume about ~ 0.4 μl are drop cast on the PMMA surface. After 2 minutes, the adhesion of part of the nanostructures in solution to the substrate (by van der Waals force) is relatively strong and stable. Consequently, the sample is rinsed in DI and dried under nitrogen flow to remove possible dirty and nanomaterial residuals.

SEM imaging is finally used to identify and characterize all the nanostructures of interest: suspended over trenches, deposited on the PMMA, and deposited on the sapphire substrate.

3.3 Post-processing characterization

Nanostructures in all three configurations have been characterized by **Scanning Electron Microscopy** (SEM), see Figure 3.10.

For conductive substrates, the electrons of the beam flow across the substrate toward the sample holder. Instead, for insulating substrates such as the sapphire substrate, electrons accumulate at the substrate, yielding to **charging phenomena**. These cause electron beam deflection due to the repulsive force which arises from the presence of the accumulated negative charge, resulting in the impossibility to perform high quality imaging. Several tests have been performed to identify the optimal conditions for imaging, corresponding to:

- limited charging effect;
- limited the PMMA alterations caused by the electron beam destroying the previously defined pattern.

Actually, the following conditions have been identified as the most effective:

- use of electrically conductive, non-porous carbon adhesive tape in contact with each side of the sapphire substrate, maximizing the electron discharge from the substrate (for electron beam working at 1.7 KV EHT, corresponding to 30 pA current, used in the Analytic mode and secondary electrons detected);
- sample completely in contact with the metallic holder (electron beam energy of 1.6 keV, with 10 pA current, ultra-high resolution scan mode, secondary electrons detected).

Use of low accelerating voltage, avoiding the charging effect thanks to the balance between the amount of electrons impinging and leaving the substrate surface.

The imaging of the overall substrate surface indicates that trenches are well-lithographed and relatively clean from residues. The imaging with $> 45°$ tilted stage clearly shows the nanostructures suspended over the trenches (Figure 3.10).

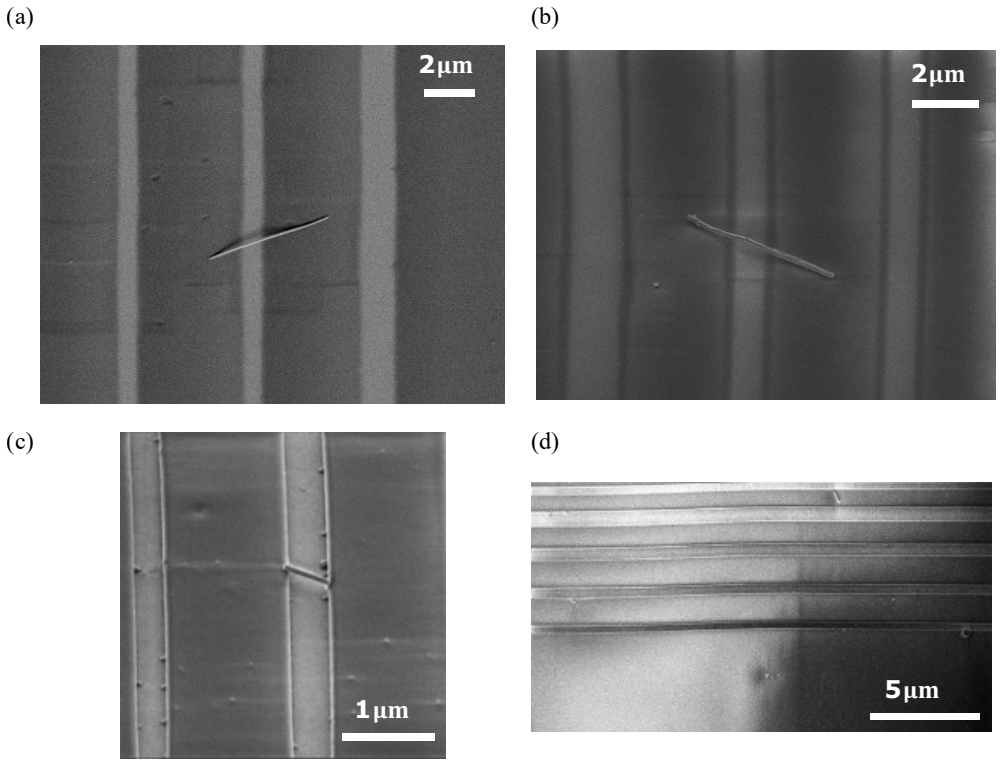

Figure 3.10: SEM imaging of the fabricated samples. (a) InAs NW-type L suspended over a trench, 60 ° titled view. (b) Suspended MoS2 NT, 45 ° titled view. (c) Suspended InAs NW-type S, 45 ° titled view. (d) View of the trenches at the end of the fabrication process.

To analyze the actual depth of the trenches, a DektakXT **stylus surface profiler** system is used. In order to have an average and more precise estimate of the PMMA thickness on the overall surface, the measure has been preliminarily performed orthogonally to a ~ 200 µm wide channel which is mechanically made on the sample, by hand. The measure indicates a (272 ± 2) nm PMMA thickness, as shown in Figure 3.11a. Subsequently, the profilometry applied along a line orthogonal to the trench (as displayed in Figure 3.11b). Although the lateral resolution of the profiler didn't allow a precise description of the trench's shape, the measure of the widest trenches confirmed their (300 ± 30) nm depth, verifying the successful outcome of the fabrication process.

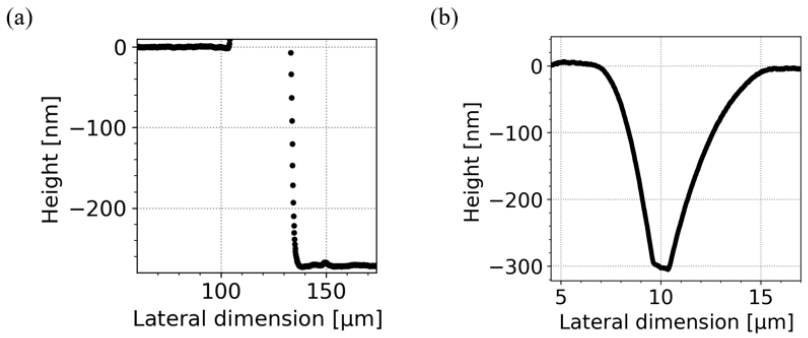

Figure 3.11: Experimental curves indicating the average PMMA thickness (a) and a trench depth (b), measured via profiler.

3.4 Raman and electronic characterization of MoS_2 NTs

Raman spectroscopy was performed on the optically characterized NTs to exclude the presence of oxide, which could potentially fill the inner core [27]. Raman analysis was conducted using a Horiba LabRAM HR Evolution micro-spectrometer equipped with a 532 nm solid-state laser (maximum power: 100 mW). The system employed a diffraction grating with 1800 grooves/mm for single-spectra acquisition. A 100X magnification lens was used to focus the Gaussian beam on the sample surface, with a FWHM of $\sim$ 1.5 µm and energy intensity of 0.63 mJ/µm^2. Data were acquired over 5 seconds with three accumulations to minimize noise. The extended spectrum, generated via the Horiba acquisition software, was composed of four consecutive spectra covering distinct Raman shift ranges. The Raman spectra, shown in Figure 3.12, featured the E_{2g} and A_{1g} peaks, corresponding to in-plane and out-of-plane vibrations of MoS_2 molecules, respectively [144]. A slight blue-shift was observed in the peaks positions for larger NTs compared to smaller ones, with values of 378 cm^{-1} and 405 cm^{-1} for smaller NTs and 382 cm^{-1} and 408 cm^{-1} for larger NTs. The peak separation of 27 cm^{-1} for smaller NTs and 26 cm^{-1} for larger NTs is consistent with a multiwalled structure comprising more than 10 layers [144]. Furthermore, Figure 3.12a shows the absence of satellite peaks at 280 cm^{-1} and 816 cm^{-1}, indicative of the MoO_x phase [145], confirming the lack of an oxide core in the NTs.

SEM imaging of MoS_2 NTs before the optical experiments suggested the occurrence of irregularities in the morphological features. However, the constraints imposed to the SEM settings to prevent sample damaging prior to optical investigation, were detrimental to optical imaging. Therefore, SEM imaging was performed without setting limitations after the optical experiments (ES and US), upon metalization of the NTs with a few

nanometer Au film.

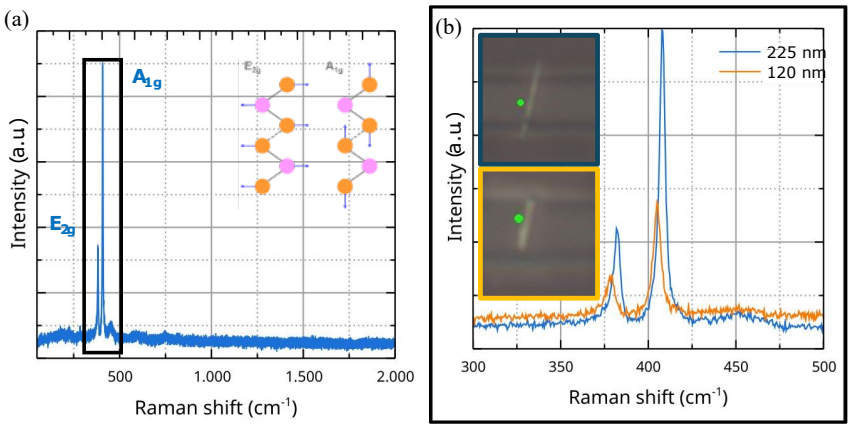

Figure 3.12: Raman characterization. (a) Representative Raman spectrum acquired on the suspended NT with external diameter 225 nm and showing the absence of satellite peaks related to MoO_x crystal phase. (b) Raman spectra of suspended NTs in two external diameter ranges. In the inset , the optical images are shown.

Images were acquired using an FEI Quanta-200 system with a secondary electron detector, operating at EHT = 15 kV, and are shown in Figure 3.13.

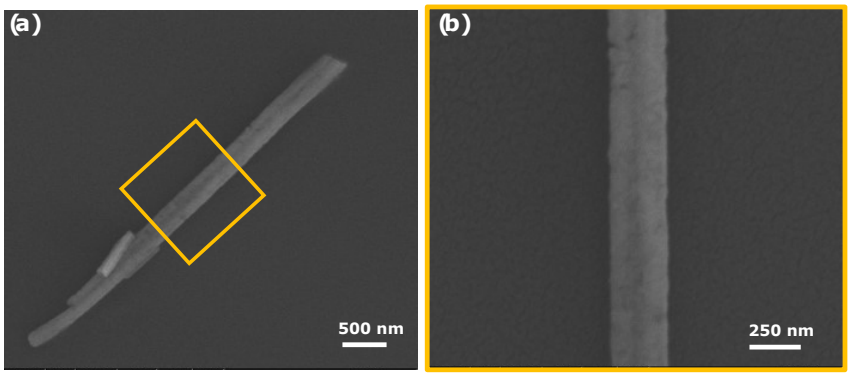

Figure 3.13: (a) SEM image of one of the measured NT, after metallization. (b) Magnification on the central section of the nanostructure.

Finally, High-Resolution Transmission Electron Microscopy (HRTEM) was performed on the same batch of NTs to obtain statistically significant insights into the internal structure of NTs with external diameters ranging from approximately 120 nm to 220 nm, as the ones investigated optically (see Chapter 4). The NTs were deposited on holey carbon-coated copper TEM grids, ensuring minimal overlap between nanostructures. HRTEM imaging was carried out using a ThermoFisher Talos FS200 microscope equipped with a Schottky field emission gun (FEG) operating at EHT=200 kV. Images were captured at varying magnifications to assess the number and arrangement of layers (Figure 3.14). NTs

within the targeted diameter range were observed to have inhomogeneous wall structures, with occasional layer dislocations disrupting their regular stacking, a common feature in van der Waals nanomaterials. Internal contrast variations were noted, suggesting irregularities and inhomogeneities in the layering, indicative of multiwalled domains with varying layer orientations.

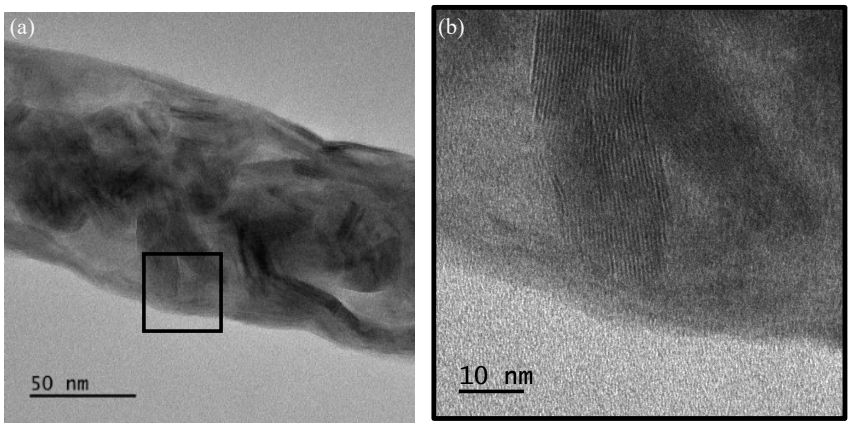

Figure 3.14: TEM image of a MoS_2 NT (a) and detail (b).

Chapter 4

Energy transfer in MoS_2 Nanotubes

This chapter presents the linear and ultrafast optical investigations performed on individual multiwall MoS_2 NTs. MoS_2 NTs were only recently synthesized: their linear optical properties together with sub-surface morphological features were largely unknown, and represent the focus of the present chapter. Section 4.1 addresses the SMS investigation of MoS_2 NTs. SMS is here employed, as a complementary technique to ES, for the localization of some of the NTs. Section 4.2 starts addressing the NTs orientation relative to the laser beam polarization, preliminary to their optical characterization by ES. Afterword, the section focuses on retrieving the extinction cross-section per unit length of the NTs and its dependence on NT diameter, environment, light polarization and wavelength. The optical extinction cross-section (sum of the absorption and scattering cross-sections) is the parameter which governs the attenuation of an optical beam upon interaction with a MoS2 NT. In particular, the absorption cross-section rules the NT's energy absorption which, in the context of pump and probe experiments (4.3), triggers mechanical vibrations.

Section 4.3 is devoted to the time-resolved investigation, providing insights into the MoS_2 NT's mechanical properties and linking them to morphological features not otherwise accessible. Specifically, the MoS_2 NT breathing and thickness modes are accessed. They allow to retrieve morphological information, such as the NT shell thickness. Section 4.4 summarizes the conclusions of the chapter and discusses future perspectives.

4.1 Optical detection

As described in Chapter 3, the electron microscopy characterization allowed to identify and morphologically characterize NTs with diameters of approximately 120 nm and 225 nm, in three configurations: suspended over trenches, PMMA-supported, and sapphire-

supported. The optical linear and time-resolved investigation conducted in this chapter focuses on five of these NTs, whose SEM images are provided in Figure 4.1.

The optical detection step is essential for positioning the nanostructure under the center of the laser beam used for the optical characterization. Therefore, to detect each NT, the target area was identified via optical microscopy using the metal markers patterned on the sample surface, and then the region was scanned under the laser beam, using either the SMS or the ES technique, described earlier.

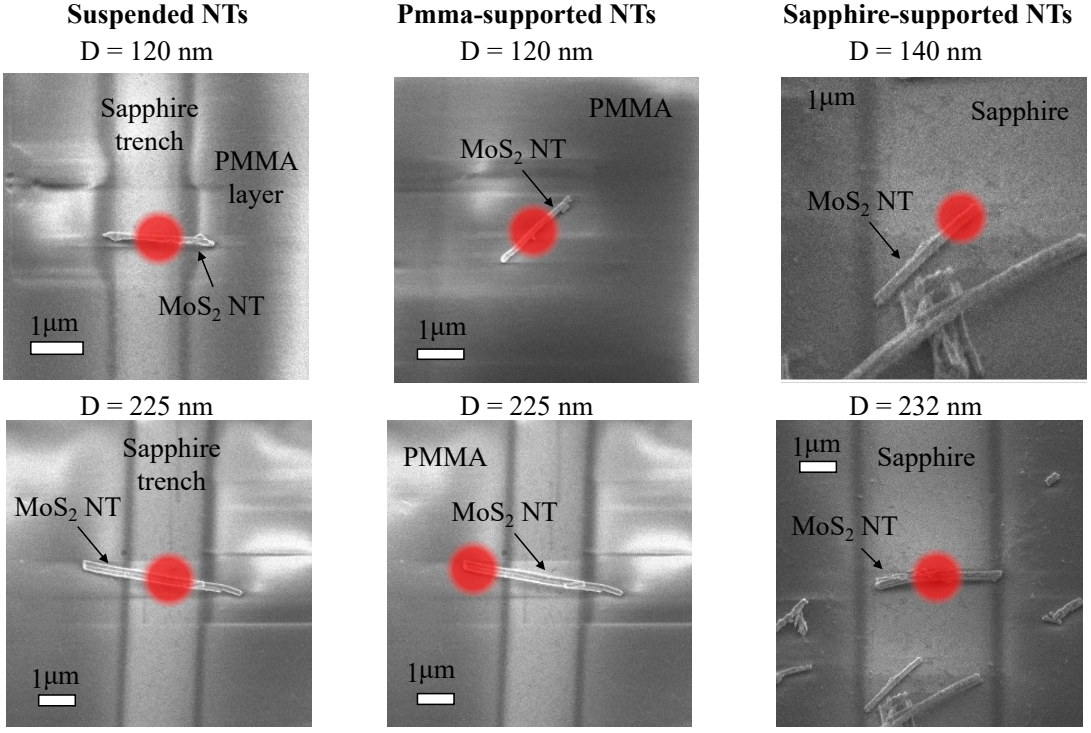

Figure 4.1: SEM images of the MoS_2 NTs in different configurations. The red spot indicates the laser beam position during the US measurements.

SMS was initially employed for detecting the nanostructures and optimizing sensitive beam parameters, such as the focal point. A representative SMS map acquired for a NT with a diameter of approximately 225 nm, suspended over a trench, is shown in Figure 4.2a, along with a line-cut across the NT axis in panel (b). The map was recorded at a wavelength of $\lambda = 820$ nm, with a spatial modulation amplitude and frequency of $\delta_y \simeq 300$ nm and $f = 1.5$ kHz, respectively. The map exhibits the characteristic three-lobe configuration expected for measurements at the $2f$ harmonic, where the central maximum indicates the location of the nanostructure on the map, as explained in detail in Chapter 2. The irregular shape of the lobes likely reflects the non-uniform morphology of the NT, while the amplitude of the signal is proportional to its optical extinction at the incident wavelength. In the following investigations, due to the large signals measured for

these NT, ES imaging and characterization were directly used instead of SMS, allowing to perform all the linear (and subsequently ultrafast) experiments.

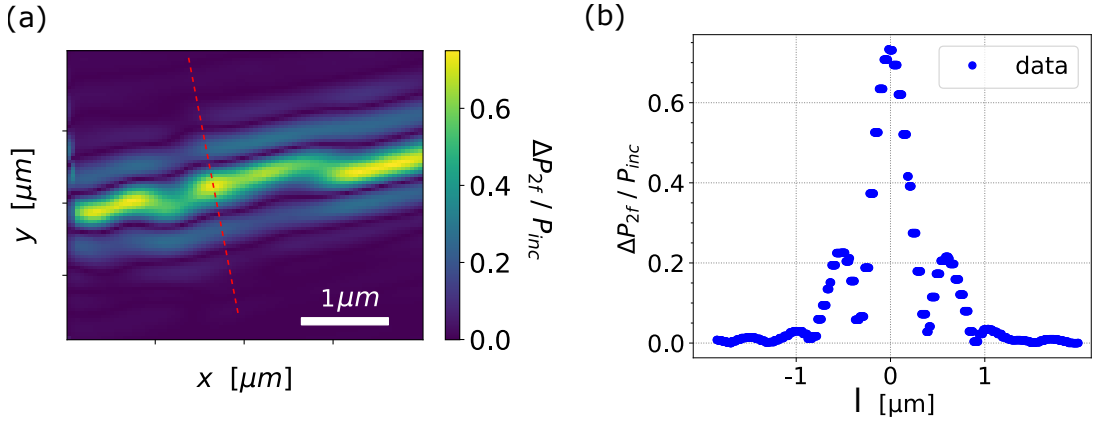

Figure 4.2: (a) SMS map of a MoS_2 NT with diameter 225 nm suspended over a trench. The dashed line indicates the direction l of the line-cut performed and shown in panel (b).

4.2 Optical extinction cross-section

The NTs were optically characterized by ES to extract their absolute extinction cross-section per unit length, $\sigma^{NT}_{L,ext}$. The conceptual and experimental procedure leading to this goal are detailed in Section 2.2. Once the chip is mounted under the input objective, the NT is detected with the laser beam focused on the NT plane. To map the transmitted power from the system, $\bar{P}_{tr}(x, y)$, the sample was raster-scanned under the laser beam. A representative 4 μm× 4 μm ES map is shown in Figure 4.3.

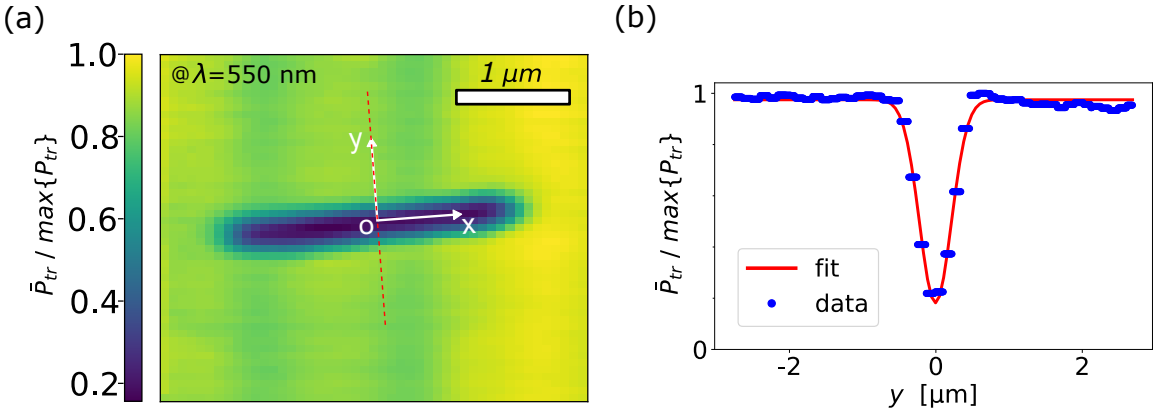

Figure 4.3: (a) ES map of a suspended NT ($D = (120 \pm 4)$ nm and $L = (2.2 \pm 0.1)$ μm) probed at $\lambda = 550$ nm with polarization parallel to the NT axis. (b) Data from the line-cut along the y-direction (blue dots) with a fitted curve (red line).

This shows the spatial distribution of the transmitted power, normalized to the maximum power within the scanned area (corresponding to the transmitted power through the substrate in the absence of the NT); thus, the value $\frac{\bar{P}_{tr}(x,y)}{max\{\bar{P}_{tr}(x,y)\}}$ is plotted. This map reports the transmission for a suspended NT with external diameter $D = (120 \pm 4)$ nm, length $L = (2.2 \pm 0.1)$ µm, suspended over a trench approximately 1.4 µm wide. The NT was probed using a laser beam with a wavelength $\lambda = 550$ nm and polarization aligned parallel to the NT's longitudinal axis. In the map, the blue region indicates the attenuation of the transmitted power due to the NT's presence. The strongest attenuation, corresponding to the minimum value of $\frac{\bar{P}_{tr}(x,y)}{max\{\bar{P}_{tr}(x,y)\}}$, occurs when the beam center aligns with the NT center, denoted as O in the figure. However, because the NT transversal dimensions are smaller than the laser beam spot size, the attenuation pattern does not directly reflect the NT's precise shape. It would be so if the NT's diameter D was smaller than the spot size, here indicated as d. This observation is demonstrated by the simulated output signals reported in Figure 4.4. The simulations were performed for a suspended NT with the same features as the representative NT of Figure 4.3a, for different values of d. The color scale is normalized from the minimum (blue) to the maximum (yellow) value of transmitted power. A clear absorption feature is obtained for small spot sizes (e.g. for the ratio $d/D = 1$), while the NT's shape is not distinguishable for large spot sizes (e.g. $d/D = 40$). The actual experimental case corresponds to a ratio of $d/D = 4.58$, with spot size $d = 550$ nm.

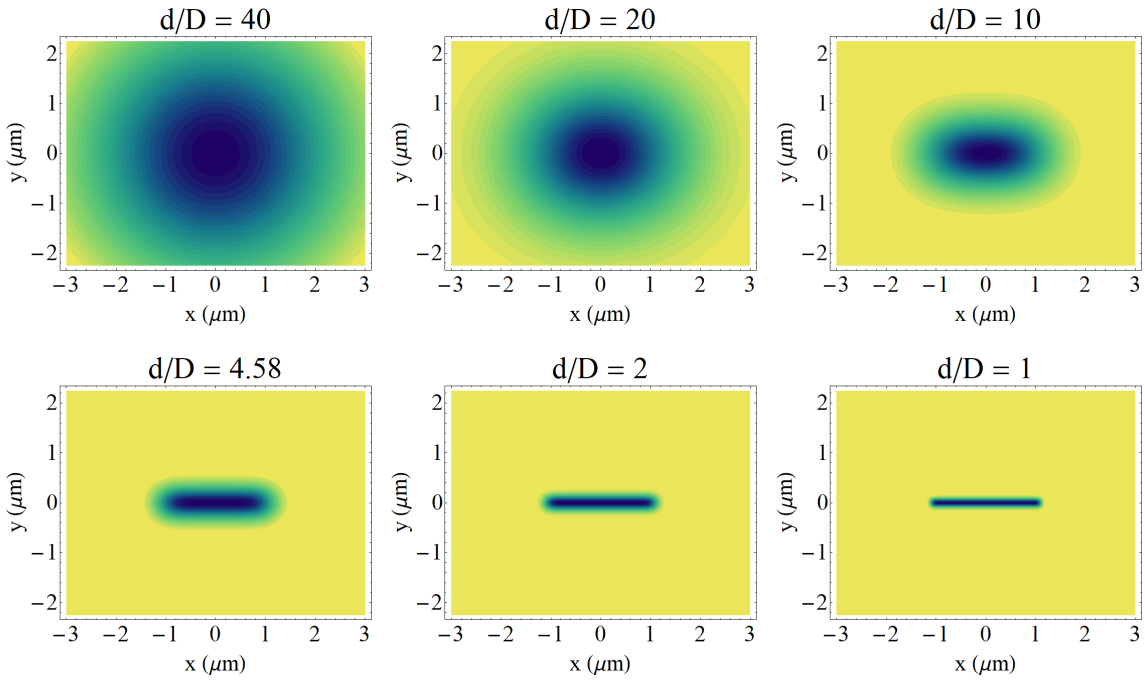

Figure 4.4: Simulated output signal at different spot sizes d.

As defined in Section 2.2.1, the coordinate system for applying the extinction cross-section per unit length retrieval method is identified by the center of the Gaussian laser beam and the NT longitudinal axis, therefore this was superimposed on the map, recovering the correct reference frame. A line-cut perpendicular to the NT axis was extracted from the map and $\sigma^{NT}_{L,ext}$ was calculated using the fitting procedure based on Equation 2.6. An example of the line-cut and its corresponding fit is shown in Figure 4.3b. To estimate error bars, the fitting procedure was repeated for adjacent positions along the NT, and the maximum and minimum variations in $\sigma^{NT}_{L,ext}$ were used to calculate the uncertainty. When multiple measurements were available, their mean value and standard deviation were used.

A wavelength and polarization-dependent analysis was performed. The polarization dependence of $\sigma^{NT}_{L,ext}$ was measured at λ=720 nm for the representative NT and the result is reported in Figure 4.5a. The extracted extinction cross-section per unit length strongly depends on the polarization direction, ranging from $\sim$ 650 nm^2/nm for parallel polarization to $\sim$ 515 nm^2/nm for perpendicular polarization. The fit of the polarization dependence of $\sigma^{NT}_{L,ext}$ allowed to identify the polarization of the laser beam with respect to the NT axis. The reference system shown in Figure 4.3a is superimposed also on the polarization plot in Figure 4.5a. Subsequently, ES maps were acquired across a wavelength range of $\lambda = [440 \div 940]$ nm, with the laser polarization fixed either parallel or perpendicular to the NT axis. The resulting $\sigma^{NT}_{L,ext}$ spectra for this NT are presented in Figure 4.5b for both parallel (blue) and perpendicular (red) polarization directions.

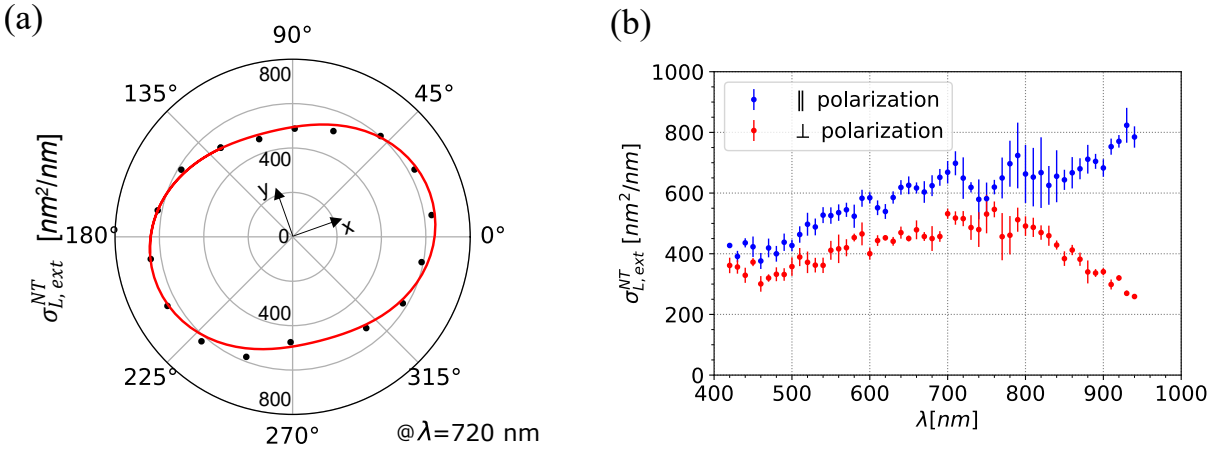

Figure 4.5: (a) Polar plot showing the polarization dependence of $\sigma^{NT}_{L,ext}$. (b) $\sigma^{NT}_{L,ext}$ spectra for the suspended MoS_2 NT with 120 nm diameter.

This procedure was applied to all NTs presented in Figure 4.1, with the resulting spectra displayed in Figure 4.6. Graphs in panels a-c refer to NTs with small diameter $D \sim 120$ nm, while panels e-g show data for wide diameter NTs with $D \sim 225$ nm. The first column reports the case of suspended nanotubes, while the second and third column refers to the PMMA and sapphire-supported NTs, respectively. $\sigma^{NT}_{L,ext}$ was found displaying values of tens to few hundreds nm^2/nm, depending on wavelength, polarization, environment and size.

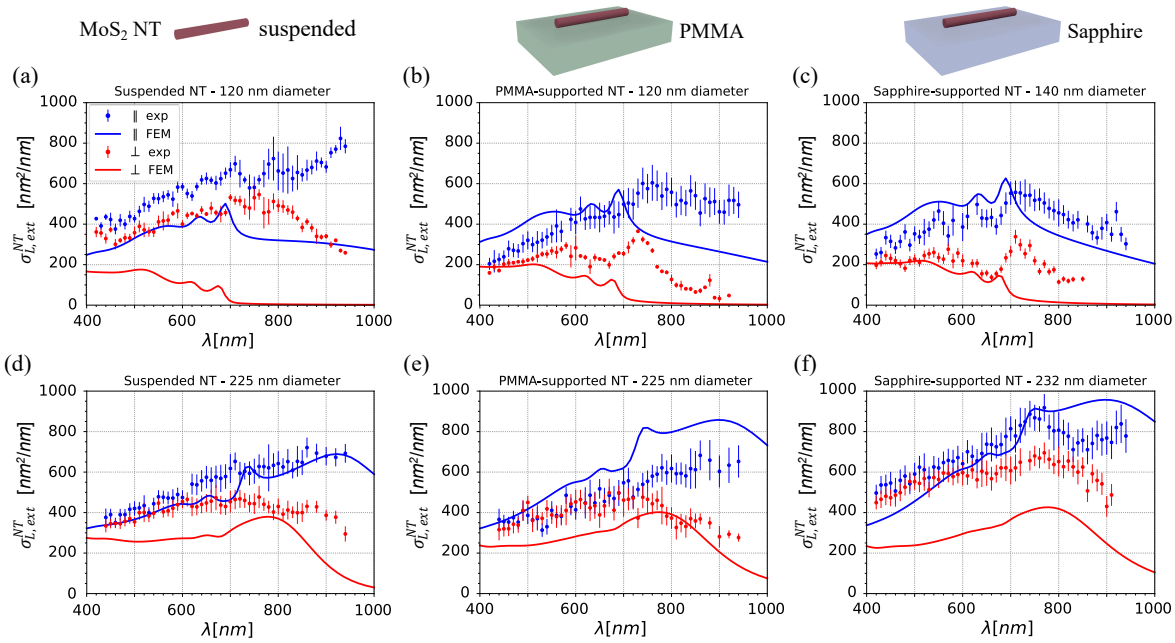

Figure 4.6: $\sigma^{NT}_{L,ext}$ spectra for all investigated MoS_2 NTs in different configurations.

Overall, these key parameters shape the observed trends.

Polarization effect. The orientation of the laser polarization relative to the NT axis significantly influences $\sigma^{NT}_{L,ext}$. Parallel polarization generally yields higher extinction cross-section values than perpendicular polarization, a behaviour that is confirmed both from the analytical and FEM simulations. As shown in Figure 4.7, a general increasing trend is observed for both polarization orientations up to a wavelength of about 740 nm. Beyond this point, the extinction cross-section per unit length decreases at longer wavelengths when the polarization is perpendicular to the NT axis (as shown in panels (c) and (d)), while it increases for larger NTs (panel (b)) and small suspended NT (panel (a)) when the polarization is parallel.

Environment effect. The presence and type of substrate also play a critical role in determining $\sigma^{NT}_{L,ext}$, as can be observed in Figure 4.7.

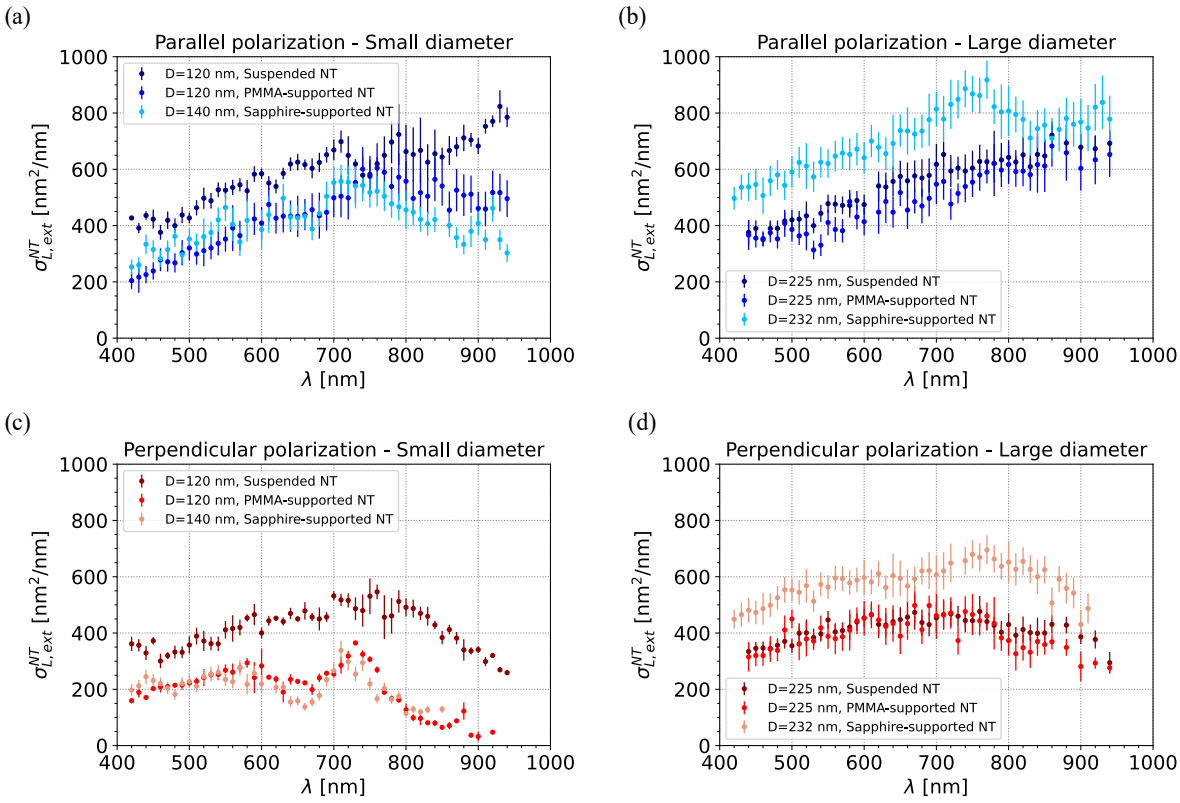

Figure 4.7: Effect of light polarization as well as of the presence or absence of media supporting the NTs on the $\sigma^{NT}_{L,ext}$ spectra, for NTs with diameter on approximately 120 nm (a), (c) and 225 nm (b), (d).

For smaller NTs, in both parallel and perpendicular polarization (panels (a) and (c)) the suspended NT exhibits a higher extinction cross-section over the entire wavelength range for both polarizations (although its diameter is slightly smaller than the one of sapphire supported NT, as evidenced by SEM images). Furthermore, it has more distinct spectral features compared to supported NTs (followed by the sapphire-supported NT, and lastly by the PMMA-supported one) and it shows an increasing trend at longer wavelengths, likely due to a greater contribution from scattering effects. For larger NTs, the spectral features are generally smoothed. The NT measured for both the suspended configuration (laser spot over the trench) and the PMMA-supported configuration (laser spot over the NT extremity on the PMMA) display nearly identical spectra, with the suspended portion having slightly higher values. The sapphire-supported NT, however, shows higher extinction values, which is likely due to its irregular shape and the slightly superior diameter of the investigated nano-object.

Diameter effect. Figure 4.8 highlights diameter-dependent trends for NTs measured in suspended, PMMA-supported and sapphire-supported configurations.

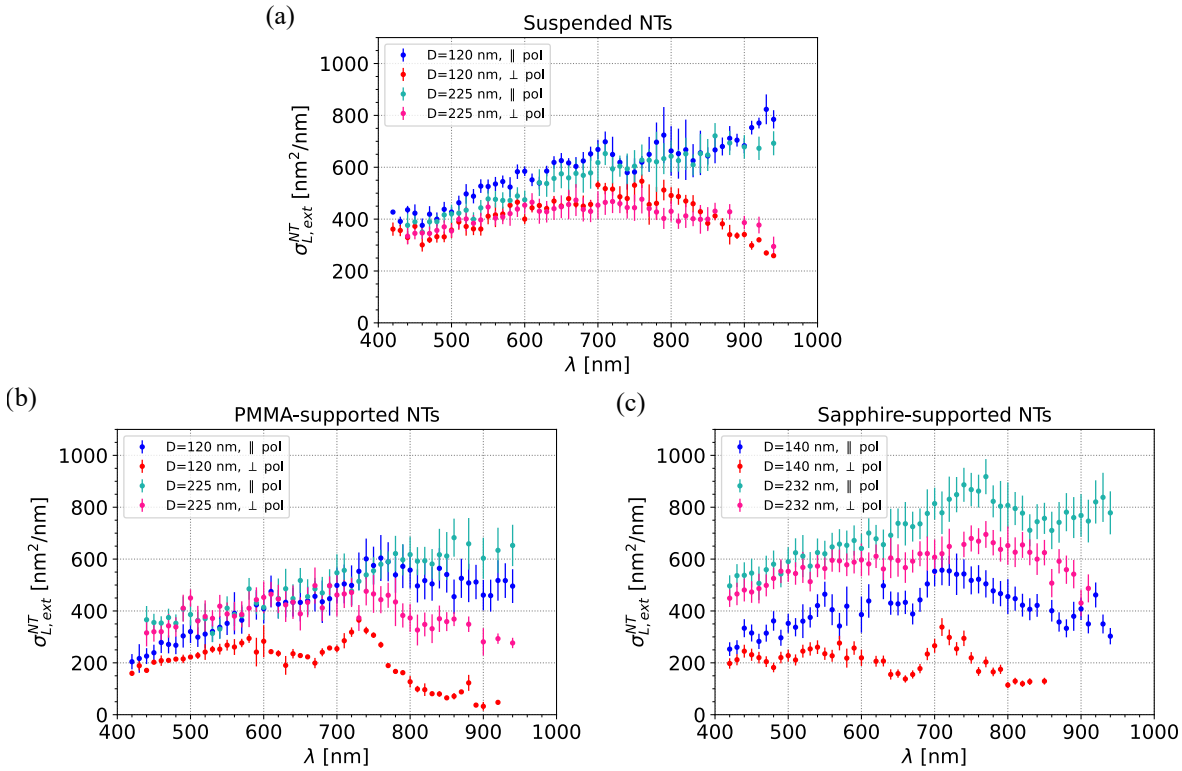

Figure 4.8: Effect of diameter on the $\sigma^{NT}_{L,ext}$ spectra for suspended (a), PMMA-supported (b) and sapphire-supported (c) NTs.

For suspended NTs, slight differences were observed between NTs with different diameters. However, the spectrum for the thinner NT exhibits more distinct features, which tend to broaden in the NT with larger diameter. This behaviour is generally observed also for supported NTs, and is likely due to the increased scattering effects at larger diameters. Instead, in the case of sapphire-supported NTs, a larger diameter results in higher extinction values. This effect may be attributed to the presence of the sapphire substrate or, more likely, to the irregular morphology of the specific NT.

Lastly, it was observed that the configuration with suspended NT of small diameter allows for an enhanced resolution of the spectral features, enabling the identification of a more extensive range of resonances. Specifically, resonances detected at 650-660 nm, 590-600 nm and 450 nm can be attributed to the MoS_2 bulk excitons of type A (660 nm), B (602 nm) and C (459), respectively [28, 146–148]. In comparison, the PMMA-supported NT reveals only a subset of the resonances observed in the suspended configuration. Notably, the resonance at 750 nm in parallel polarization (730 nm in perpendicular polarization) splits into two distinct peaks at 710 nm and 790 nm. For the sapphire-supported NT, a resonance at 550 nm is observed in parallel polarization (540 nm in perpendicular polarization), which is absent in the suspended NT configuration.

4.2.1 Discussion and Interpretation

These results represent the first measures of the absolute extinction cross-section per unit length for MoS_2 NTs in different configurations and sizes. To rationalize these results and to elucidate the role of the absorption - a key factor for subsequent time-resolved investigations - both analytical and FEM simulations were used. These methods provided a comprehensive understanding of the system's optical properties.

Analytical simulations

The analytical model employed Mie theory, extended for an infinitely long cylinder as detailed in Section 1.1.2. The simulation results for NTs with diameters of 120 nm and 225 nm are presented in Figure 4.9, with panels (a) and (b) corresponding to the smaller diameter and panels (c) and (d) to the larger one. The NTs were assumed to be immersed in air, with the environmental refractive index incorporated into the model.

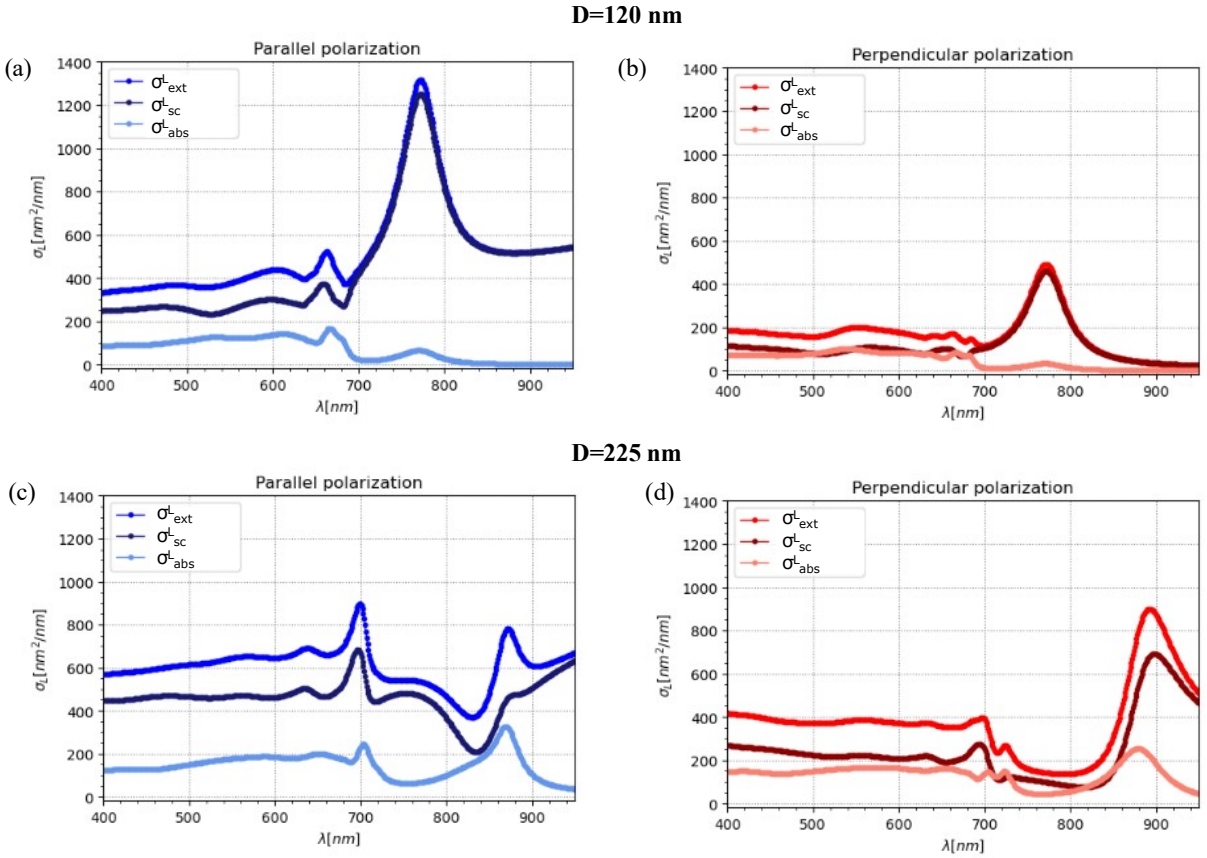

Figure 4.9: σ_{ext}^{L} spectra for the 120 nm and 225 nm diameter NT, simulated by Mie theory, for both polarization directions. The contributions of absorption and scattering are represented.

This approach enabled a first insight into the separation of absorption and scatter-

ing contributions to the absolute extinction cross-section per unit length. The simulated sigma extinction cross-section per unit length, σ_{ext}^{L}, broadly reproduced the experimental trends for both polarization configurations, reflecting similar differences in the values obtained for parallel and perpendicular polarization cases. Importantly, these simulations highlighted the substantial influence of scattering, even when relying solely on an analytical framework.

Nevertheless, the model's limitations arise from its simplifying assumptions. Although the NTs' diameter-to-length ratio (approximately 0.05) supports the hypothesis of an infinitely long cylinder, several approximations could lead to discrepancies with experimental data. For instance, (i) an incident electromagnetic *plane wave* was assumed, (ii) the NT was modeled as a solid cylinder rather than a hollow structure, and (iii) the optical properties were derived from the refractive index at different wavelengths of a multilayer flake of MoS_2 [149], as the properties of MoS_2 NTs are not yet characterized.

These factors likely contribute to the inability of the analytical model to exactly match the experimental data, even though it captures the overall trends.

FEM simulations

To address the complexities and refine the analysis, finite element method (FEM) simulations were performed. These accounted for essential parameters such as the geometry of cylindrical shells, the anisotropic dielectric tensor of MoS_2, the presence of substrates, and the cone of light collected by the photodetector. Figure 4.10 provides a schematic of the FEM model.

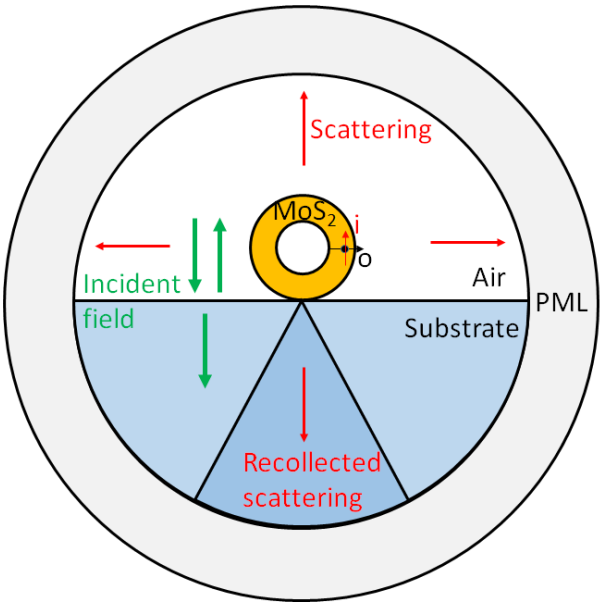

Figure 4.10: Schematic of the model used for FEM simulations.

The RF module of the COMSOL software is employed to construct a 2D simulation model, which is suitable thanks to the translational symmetry along the NT axis. The optical response was modeled assuming linearly polarized plane-wave illumination of infinitely long NTs. A perfectly matched layer surrounded the simulation domain to prevent spurious reflections at its borders.

The NT geometry was represented as a circular shell defined by external (D) and internal (D_{in}) diameters. For smaller NTs, wall thicknesses of 10 nm were assumed, with D_{in}=120 nm and D=140 nm. Larger NTs were modeled with wall thicknesses of 20 nm, D_{in} = 190 nm and D = 230 nm. The values adopted for D are close to the values retrieved by the SEM measurements.

The anisotropic dielectric tensor accounted for differing in-plane and out-of-plane dielectric properties, corresponding to the NT's axial and radial directions. Literature values for bulk MoS_2 dielectric properties were employed [150, 151]. The inhomogeneous environment around the NT was included to account for substrate effects. Refractive indexes n_{sub} of 1.76 and 1.5 were used for sapphire and PMMA substrates, respectively, and a refractive index of 1 was used for taking into account the air both surrounding and inside the NT. The scattered field formulation was used and partial wave reflections from substrates were incorporated in the definition of the electromagnetic field interacting with the NT.

The absorbed and scattered powers are obtained from the computed electric field profiles. To align with experimental measurements, the simulations considered the effect of light scattered at small angles, which is recollected by the detection objective and thus does not contribute to extinction [114]. Scattered light with angles less than arcsin(NA), where NA=0.7 was the numerical aperture of the output objective, was excluded. For substrates, Snell's law adjusted the angle threshold to $\arcsin(\mathrm{NA}/\mathrm{n}_{sub})$.

Figure 4.6 compares simulated and experimental σ_{ext}^{NT} spectra for suspended and supported NTs of varying diameters and polarizations. While the simulations successfully capture the magnitude and qualitative trends, deviations are notable at longer wavelengths and for suspended NT with 120 nm diameters. These discrepancies can be attributed to the irregular NT morphologies, as observed in electron microscopy images and to the potential bundling or partial filling of the NT core by internal walls. Furthermore, assumptions about the dielectric tensor and chosen internal diameters also play a role.

Further simulations, shown in Figure 4.11, explored the effects of these assumptions, for the case of suspended NT with 225 nm diameter. An isotropic dielectric tensor derived from measurements by Yim et al. [152] was considered (panel (a)). This model resulted in a trend smoother but similar to anisotropic simulations, confirming both the validity

of the anisotropic model and the bulk dielectric table used. The role of diameters and shell thickness has been addressed. In panel (b) both internal and external diameters are varied, keeping constant the wall thickness. This shows just a slight adjustment of the spectral curves. On the contrary, panels (c) and (d) show the dependence of the simulation on the value chosen as external and internal diameter, while keeping constant the internal and external one, respectively, i.e. changing the shell thickness: significant changes were observed in this case.

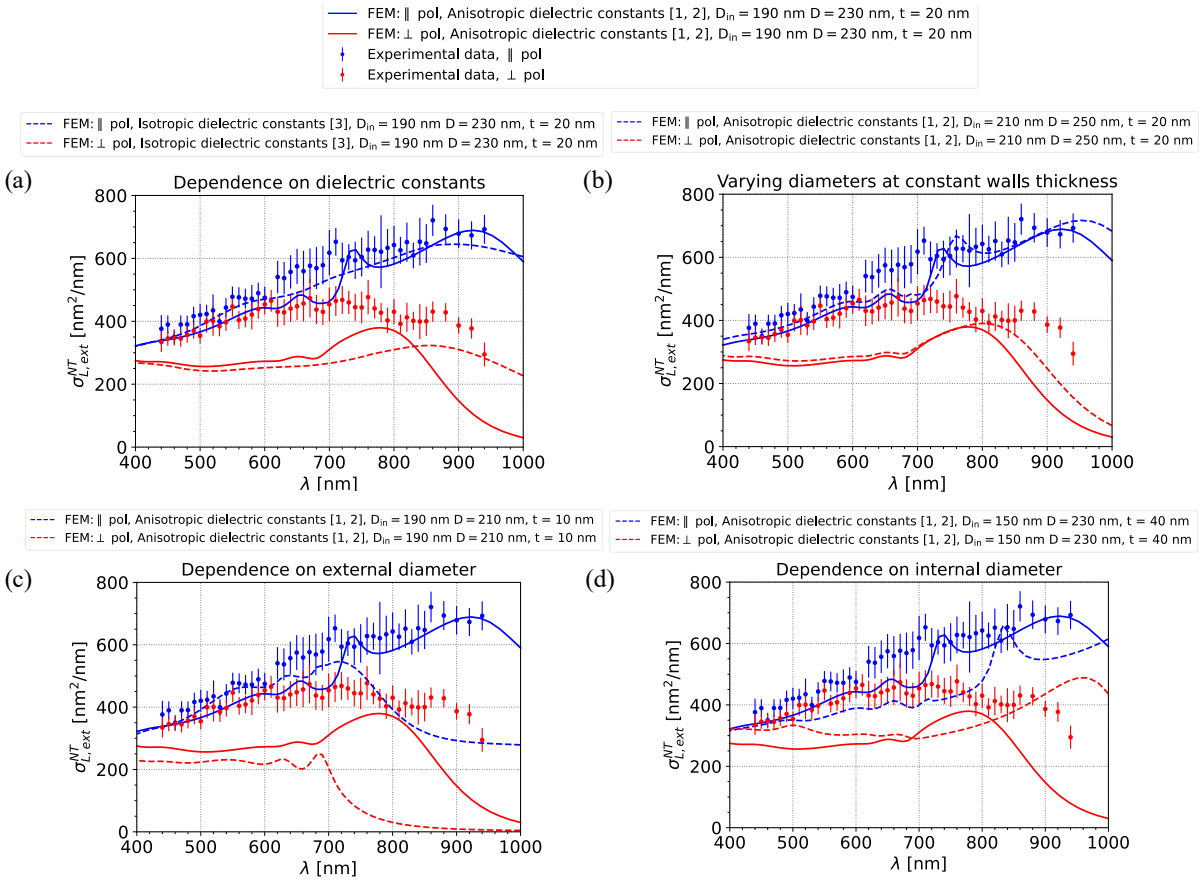

Figure 4.11: Comparison of the σ_{ext}^{L} experimental spectra, with the signal obtained by FEM modeling, changing different parameter, i.e. dielectric constants, shell thickness, internal and external diameter.

Finally, the agreement between simulations and experimental data, particularly for larger NTs, suggests that the chosen shell thicknesses are reasonable. For smaller NTs, further pump-probe measurements will refine estimates, predicting a thickness near 16 nm.

Absorption contribution

FEM simulations have been instrumental in elucidating the relative contributions of absorption and scattering cross-sections per unit length. Unlike the archetypal behaviour observed in single-walled carbon NTs [113, 153, 154], where $D \ll \lambda$ and the extinction cross-section is predominantly attributable to absorption, the diameters of MoS_2 NTs in this study are only slightly smaller than the incident laser wavelengths. This size regime precludes such a simplification, as scattering contributes significantly, as previously evidenced by simulations (Figure 4.9).

Figure 4.12 illustrates the absorption contribution (shaded area) to the extinction cross-section per unit length (solid line) for a representative 225 nm diameter NT, in comparison with experimental results.

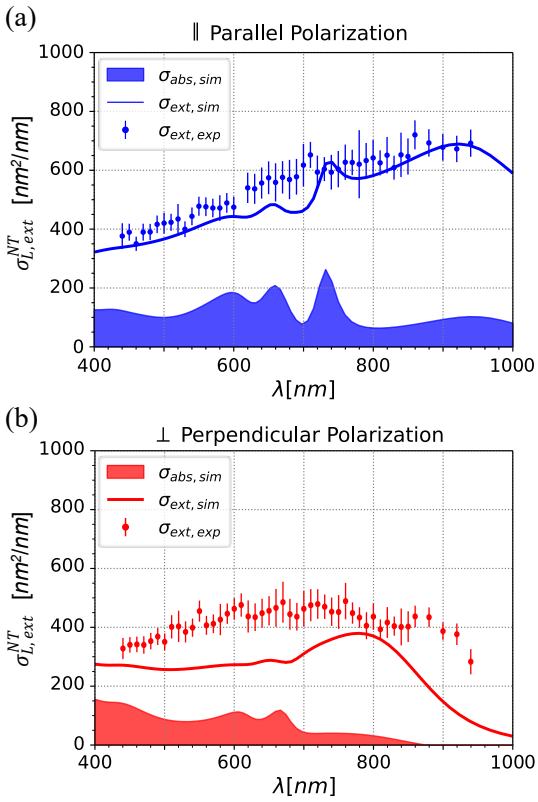

Figure 4.12: σ^{L}_{ext} spectra for the 225 nm NT, comparing experimental and simulated results for both polarizations. The shaded area represents the absorption contribution to the signal.

It is observed that scattering and absorption ($\sigma^{NT}_{L,sc} = \sigma^{NT}_{L,ext} - \sigma^{NT}_{L,abs}$) contribute nearly equally to the extinction cross-section up to $\lambda \simeq 700$ nm, consistent with expectations at longer wavelengths. A similar trend is noted for the 120 nm diameter NT, with a slightly reduced dominance of the scattering contribution at wavelengths shorter than 700 nm.

Further analysis of panels (a) and (b) reveals polarization-dependent effects: scattering is enhanced for parallel polarization up to approximately 900 nm, whereas for perpendicular polarization, scattering diminishes beyond approximately 760 nm. At wavelengths exceeding 700 nm, the observed absorption aligns with theoretical predictions. Specifically, the imaginary part of the dielectric function (k) decreases significantly near 700 nm, reducing to one-tenth of its value at 600 nm. This behavior corresponds to the bulk MoS_2 bandgap near 700 nm (1.77 eV). However, k does not vanish entirely [150, 151], and in conjunction with geometric effects, it continues to contribute to absorption. Below 700 nm, absorption is primarily dictated by the dielectric properties, while above 700 nm, geometric effects become dominant, giving rise to resonances.

4.3 Mechanical properties

As outlined before in this thesis, MoS_2 is highly relevant for mechanical engineering, thanks to its high mechanical strength and wear resistance, while its electronic properties make it promising for flexible nanoelectronic devices. However, given the recent synthesis of MoS_2 NTs, their mechanical properties remain largely unexplored. Following the characterization of their optical properties, the same nanostructures are here examined using US to investigate their mechanical properties. The analysis focuses on two temporal regimes - tens of ps short and hundreds of ps long time windows - enabling the identification of optically excited radial vibrational eigenmodes in each regime, specifically thickness and breathing mode, respectively. The characteristic period of the thickness mode is analyzed to determine the shell thickness of the investigated NTs. This measurement is crucial for modeling the breathing mode, providing an estimation of the expected periods, which aids in identifying the experimental mode.

4.3.1 Experimental configurations

Multiple experimental tests were conducted to optimize the pump-probe configuration, specifically by varying wavelengths and powers, and to maximize signal amplitude while avoiding single-structure damage. The optimized experimental configurations for each case are summarized in Table 4.1, highlighting the probe wavelength as the most sensitive parameter. Notably, the pump beam was consistently optimized to $\lambda_{pump} = 410$ nm, with pump powers in the range $[15 - 40]$ μW. A weaker probe power ($P_{probe} < 1$ μW measured before entering the input objective) was used across all configurations.

Testing of various pump-probe polarization combinations revealed that the signal time-resolved trace ($\Delta T/T$) was maximum when both pump and probe beams were po-

larized parallel to the NT axis. This configuration enhances light absorption and thereby maximizes the amplitude of the initial displacement.

Experimental configurations: λ_{probe} [nm]; $\lambda_{pump} = 410$ [nm]			
	Suspended NT	PMMA-supported	Sapphire-supported
$D \sim 120$ nm	650 ± 10	700 ± 10	700 ± 10
$D \sim 225$ nm	550 ± 10	550 ± 10	690 ± 10

Table 4.1: Summary of pump-probe configurations for signal measurements.

The irregular morphology of the NTs (due to still challenging synthesis process), as revealed by TEM analysis (Section 3.4), complicates the detection of clear vibrational signatures. This complexity arises from the simultaneous excitation of multiple modes with low-quality factors, making discrimination challenging. However, analysis of extensive experimental data has enabled the identification of different vibrational periods corresponding to dominant eigenmodes triggered by absorption of the pump pulse.

4.3.2 Short time-scale (tens of ps) vibrations

For short time-delay windows, a single dominant mode was consistently observed across all NTs, as reported in Table 4.2.

Experimental short periods [ps]			
	Suspended NT	PMMA-supported	Sapphire-supported
$D \sim 120$ nm	10 ± 1	9 ± 2	10 ± 2
$D \sim 225$ nm	10 ± 2	9 ± 1	10 ± 1

Table 4.2: Short periods extracted from fits.

Figure 4.13 shows a representative short-period signal and its thermal fit (panel (a)). The residue, obtained as the difference between the black and blue curves in panel (a), is reported in panel (b) together with it's fit performed using a single oscillator model (see Section 1.2 for details on the data analysis). The oscillation period is approximately $T_{thk} \simeq 10$ ps, and its characteristics were found to be independent of the NT's external diameter, length, or surrounding environment. The subscript "thk" stands for *thickness*, since, as will be shown shortly, the oscillation is attributed to the NT radial thickness mode. Given that the shell thickness of the NT is significantly smaller than its other dimensions (e.g., diameter and length), the corresponding vibration frequency is expected to be higher, leading to a shorter oscillation period. Consequently, this mode can be

associated to the vibration of the shell thickness, h. Occasionally, frequencies with a shorter period of approximately $T \simeq 5$ ps were also detected. These frequencies can be tentatively attributed to the second harmonic of the fundamental thickness mode. However, due to its sporadic detection and experimental uncertainties - estimated to be around ± 2 ps (relative uncertainty of 40 %) - they were not addressed further.

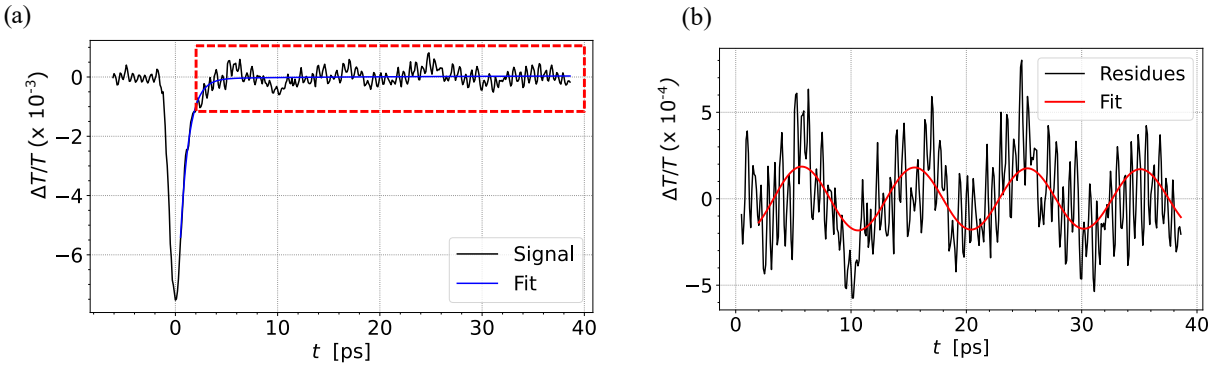

Figure 4.13: Short-period mode. (a) Pump-probe signal and its "thermal" fit for the case of a sapphire-supported NT ($D = 232$ nm). (b) Residue and its single damped oscillator fit. The oscillation is attributed to the thickness mode.

Estimation of shell thickness

These measurements provide critical information for estimating the shell thickness of the MoS_2 NTs - a parameter that is challenging to access. As detailed in Chapter 3.2 (Section 3.4), direct measurement using TEM was hindered by the complex orientation of the multi-walled domains that form the NT shells. These orientations obscure the clear electronic detection of the hollow core. Similarly, Raman spectroscopy provided only a broad approximation; the distance between the E_{2g} and A_{1g} peaks is insufficient to resolve structures thicker than 10 layers.

The shell thickness was estimated from the experimentally observed oscillation period using the model presented in Section 1.2.1 for the thickness mode of a film of thickness h, here mimicking the unfolded NT. The oscillation period of the thickness mode for the NT thus reads:

$$T_{thk} = \frac{2h}{v_{thk}}, \tag{4.1}$$

, where v_{thk} represents the sound velocity along the film thickness, $v_{thk} = \sqrt{E_{thk}/\rho}$, with E_{thk} the relevant Young modulus. For MoS_2, the Young's modulus in the thickness direction is governed by the stiffness coefficient C_{33}, which relates stress to strain along this direction. Using $C_{33} = 52$ GPa (from literature values for bulk and thin films of MoS_2 [155, 156]), $\rho = 5,06 \cdot 10^3$ Kg/m^3, and the experimentally observed period $T_{thk} \simeq 10$

ps, the shell thickness is calculated to be $h \simeq 16$ nm. This thickness corresponds to approximately 28 MoS_2 monolayers.

4.3.3 Long time-scale (hundreds of ps) vibrations

In the case of long time-scale time-resolved investigations, oscillations were detected for suspended NTs, regardless of diameter. These are shown in Figure 4.14.

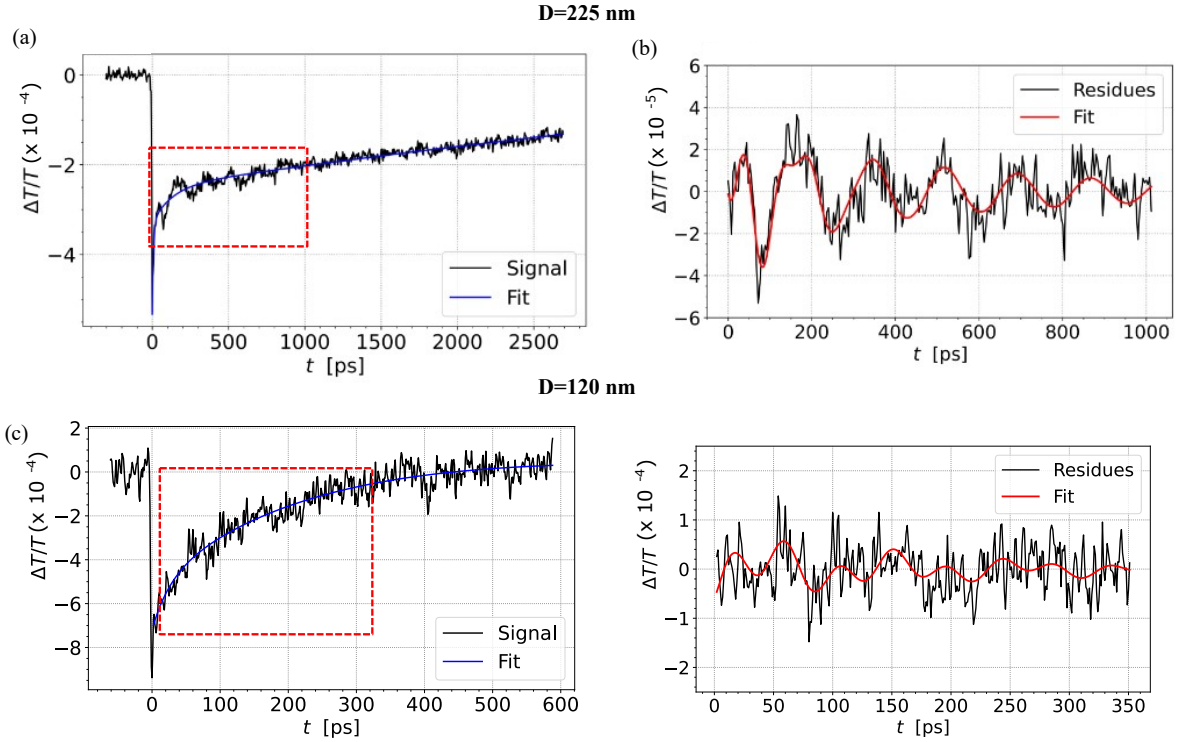

Figure 4.14: Long-period vibrational modes. Pump-probe signals and their "thermal" fit for the case of suspended NTs with diameters (a) 225 nm and (c) 120 nm. Residuals highlighting vibrational components are shown in (b) and (d) together with their two damped oscillators fits.

Panels (a) and (c) display the full signals for the suspended NTs (with external diameters $D = 225$ nm and $D = 120$ nm, respectively) including multi-exponential fitting to capture the thermal relaxation. Panels (b) and (d) show their residuals (difference between signal and fit reported in panels (a) and (c)), highlighting vibrational modes. The residuals are each fitted with the sum of two damped oscillators. Refer to Section 1.2 for details on the fitting procedure.

These analyses revealed the presence of two oscillations for each suspended NT, one characterized by a shorter period (namely T_1) and another characterized by a longer period (namely T_2). Vibrational modes were also detected for the case of substrate-supported NTs, although acoustic damping towards the substrate strongly reduced their

lifetime, hindering their visibility. Table 4.3 lists all the periods identified for the NTs in different configurations.

Experimental long periods [ps]			
	Suspended NT	PMMA-supported	Sapphire-supported
$D \sim 120$ nm	46 ± 11 ; 110 ± 4	41 ± 5 ; 18 ± 3	66 ± 8
$D \sim 225$ nm	79 ± 10 ; 175 ± 20	90 ± 19 ; 153 ± 25	88 ± 10 ; 223 ± 33

Table 4.3: Long vibrational periods extracted from fits.

Two vibrational modes were observed in supported NTs with large diameters, exhibiting oscillation periods similar to those retrieved for suspended NTs. For NTs with small diameters, the PMMA-supported configuration displayed two vibrations with periods of approximately $T \sim 41$ ps (in the same range as for small suspended NT) and $T \sim 18$ ps (potentially representing a second harmonic). In contrast, only one mode was detected for the sapphire-supported NT.

Although the vibrational periods seem to cluster in two modes with linear dependence of the corresponding periods, T_1 and T_2, on the NT diameter, the long-period oscillations could not be assigned to a specific mode and will not be further addressed in this work.

On the contrary, the approximate analytical model outlined in Section 1.2.1 supports the assignment of the short-period oscillations in Table 4.3 to the fundamental breathing modes, as will be detailed shortly. Figure 4.15 show the linear dependence of these experimental vibrational periods on the NTs diameters. The linear fit passing through the origin as dictated by the model, supports the assignment of these oscillations to radial eigenmodes.

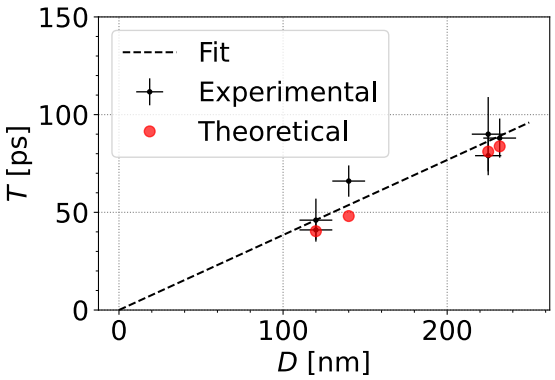

Figure 4.15: Period-diameter relationship for long time-scale modes in all investigated NTs. T_1 values align with theoretical predictions for the breathing mode.

Identification of the fundamental breathing mode

Modeling the breathing mode of MoS_2 NTs is not trivial. The NTs are composed of an anisotropic, multilayered material (MoS_2) that is rolled into a cylindrical shell. The stiffness matrix required to describe such a system is unavailable in the literature. Therefore, to address this topic, the simplified model formulated for a single-wall NT, and presented in Section 1.2.1 was here adapted to estimate the vibrational periods of the breathing mode of multi-wall MoS_2 NTs. For the sake of calculating the breathing mode, the MoS_2 NT is mimicked as a single-wall NT, with a radius equivalent to its average radius R_{avg}, made of a homogeneous and isotropic material of Young modulus matching the *in-plane* Young modulus of MoS_2. The tension responsible for the breathing mode is in fact tangential to the NT's surface and is hence related to *in-plane* Young modulus of MoS_2 (substantially, close to the C_{11} elastic component of bulk MoS_2 which rules the in-plane elastic response), refer to Section 1.2.1 and references therein for further details. The breathing mode period then reads:

$$T_{br} = \frac{2\pi R_{avg}}{v_{br}}, \tag{4.2}$$

where v_{br} is the sound velocity along the tangential direction. This velocity was estimated using the Young's modulus $E = (330 \pm 70)$ GPa, reported in the literature for MoS_2 nanosheets with thicknesses between 5 and 25 layers [157]. The average radius R_{avg} was calculated as:

$$R_{avg} = \frac{D - h}{2}, \tag{4.3}$$

where D is the external diameter measured via SEM and h is the shell thickness previously estimated from the thickness mode period. Using this approach, the theoretical breathing mode periods were determined to be $T_{br} = 41$ ps and $T_{br} = 82$ ps for NTs with external diameters of 120 nm and 225 nm, respectively.

The theoretical breathing mode periods are plotted in Figure 4.15, showing good agreement with the experimental data. These results further validate the value of the estimated shell thickness h of the MoS_2 NTs, and the assumptions made on the stiffness matrix. Furthermore, the shell thickness h is here found to be constant with NT diameter, at least for MoS_2 NTs with diameters in the 100 nm range, as the ones here investigated. The models, while simplified, effectively grasp the underlying physics, yielding a meaningful interpretation of the observed vibrational spectra.

The present investigation proves that ultrafast time-resolved nanoscopy is an effective tool to access morphological parameters of nano-objects of complicated geometry, such as MoS_2. Specifically, in the present investigation, US yielded nanoscale morphological information, specifically the NT shell thickness, which was not accessible through other

means, such as TEM or Raman spectroscopy. This finding confirms what has already emerged throughout this thesis. Ultrafast mechanical and thermal transients, in addition to providing information on the thermics and mechanics of the system, can also be exploited as a non-destructive, in-situ tool to access sub-surface morphological information at the nanoscale.

4.4 Conclusions and Perspectives

In conclusion, the absolute experimental values of the optical extinction cross section per unit length of single MoS_2 multiwall NTs in the wavelength range spanning from 440 to 940 nm have been reported. Measuring individual NTs has enabled correlation of results with their specific dimensions, composition, and, to a certain extent, morphology, a crucial consideration given the wide dispersion of these properties.

Measurements revealed a strong dependence on the diameter of the NT and its environment, with significant variations observed between suspended, PMMA-supported and sapphire-supported configurations.

The values are highly sensitive to the polarization of light, with distinct differences observed between parallel and perpendicular polarizations.

Finite element method simulations, informed by morphological input parameters from electron microscopies, indicate that both absorption and scattering contribute significantly to the extinction cross section per unit length, with the relative contributions varying with NT diameter, surroundings and light polarization.

Regarding the mechanics, impulsively excited ultra-high frequency (GHz range) acoustic oscillations were detected in a previously studied individual MoS_2 NT using time-resolved optical nanoscopy. By measuring NTs with two distinct diameters and applying simple analytical models, the radial and breathing modes of the NTs were resolved. Analyzing these modes not only holds promise for future mass sensing applications but also proved essential for determining the NT shell thickness, a critical morphological parameter. This thickness could not be accessed by other methods, such as TEM or Raman spectroscopy, highlighting US as a non-destructive technique that provides valuable subsurface morphological information on hollow nanostructures.

The present work identifies areas for future research to build upon the current understanding. Regarding the MoS_2 extinction cross-section, the agreement between experiment and simulation was only qualitatively satisfactory in some cases, highlighting the need for a more accurate dielectric function for realistic MoS_2 multiwall NTs. This could be pursued by further improving NTs morphology. As for the mechanics, devel-

oping a suitable numerical model to account for the actual MoS_2 dielectric tensor would be desirable. Furthermore, extending the investigation to MoS_2 NT of smaller diameters will open the gate towards excitation of even higher acoustic frequencies, a key aspect for mass-sensing and high-frequency opto-acoustic transducers. Furthermore, it would enable modulating the MoS_2 electromagnetic whispering gallery mode (detected in 60 nm diameters NT) via excitation of the radial modes.

Chapter 5

Energy transfer in InAs Nanowires

This chapter reports on the mechanical and thermal energy transfer involving individual InAs NWs investigated by all-optical means. Section 5.1 focuses on the optical detection of individual NWs via two optical methods, the choice depending on the NW size. Then it describes the measurement of the pump and probe beam polarizations with respect to the NWs axis. This is a required step, preliminary to time-resolved measurements, the latter being addressed in Section 5.2. Sections 5.3 and 5.4 present a comprehensive discussion of the experimental and theoretical results concerning the mechanics and heat transfer out of individual InAs NWs. Sections 5.3 reports the identification of breathing and extensional modes, and their correlation to the NWs' morphological features. The measurements allow benchmarking the stiffness matrix proposed for WZ InAs NWs. The mechanisms responsible for the attenuation of NW oscillations are addressed for the case of the radial breathing mode in the hypersonic frequency range. Extrinsic (i.e. due to transmission of mechanical energy from the NW to the substrate) and intrinsic attenuation times are retrieved, showing extrinsic attenuation to be dominant pathway. In Section 5.4 a novel metric is introduced to characterize heat transfer dynamics (from the NW to the substrate) starting from time-resolved optical traces acquired under "non-ideal" conditions, as is the case for suspended NWs. The role played by the substrate in the NW thermal relaxation is addressed. An estimate of the interface thermal conductance at the NW-PMMA interface is provided. Section 5.5 summarizes the results and explores the broader implications and potential future directions of this study.

5.1 Optical detection and polarization measurements

This thesis focuses on two types of InAs NWs, described in Chapter 3: one NW-L (a few μm long, with diameter $\sim$ 100 nm) and four NWs-S (length $<$ 1 μm, with varying

diameters in the range $[55 - 75]$ nm). Given their different dimensions, different optical detection methods (described in detail in Chapter 2) are used for these two types of NWs, namely, Extinction Spectroscopy (ES) for centering the laser beam on NWs-L, and Spatial Modulation Spectroscopy (SMS) for centering on NWs-S.

5.1.1 NWs-L

NWs-L partially suspended over a trench and partially supported on PMMA were examined. A representative SEM image of this configuration is shown in 5.1. SEM microscopy was used to detect NWs and analyze the geometry of the system, as detailed in Chapter 3.

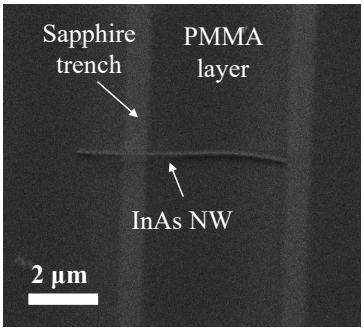

Figure 5.1: SEM image of NW type L analyzed via Ultrafast Spectroscopy (US).

Optical detection of NWs-L was performed by ES, by raster scanning the sample under a focused laser beam and detecting the transmitted power, $\bar{P}_{tr}$, at each point of the area surrounding the nanostructure, as explained in detail in Chapter 2.

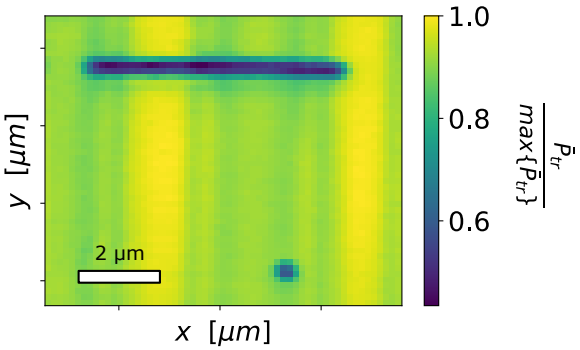

Figure 5.2: Representative ES map acquired at a wavelength of $\lambda = 410$ nm on a type-L NW. The map spans an area of 8.7 µm $\times$7.3 µm, including the NW and a nanoparticle used as a spatial reference and for pump and probe beam alignment, prior to the time-resolved investigation on the NW.

A representative ES map is shown in Figure 5.2, covering an area of 8.7 μm ×7.3 μm that includes the suspended NW shown in Figure 5.1 and a nanoparticle that was used to align the pump and probe beams (as detailed in Chapter 2). The nanoparticle also served as a reference point to test the reproducibility of precise beam positioning along the NW length during the measurements. The map was acquired at a wavelength of $\lambda = 410$ nm with polarization parallel to the NW axis. The value of $\bar{P}_{tr}$ is normalized to its maximum on the map, $max\{\bar{P}_{tr}\}$.

5.1.2 NWs-S

NWs-S, either suspended over a trench or fully supported on PMMA, were characterized by SEM to determine their morphological properties (see Figure 5.3).

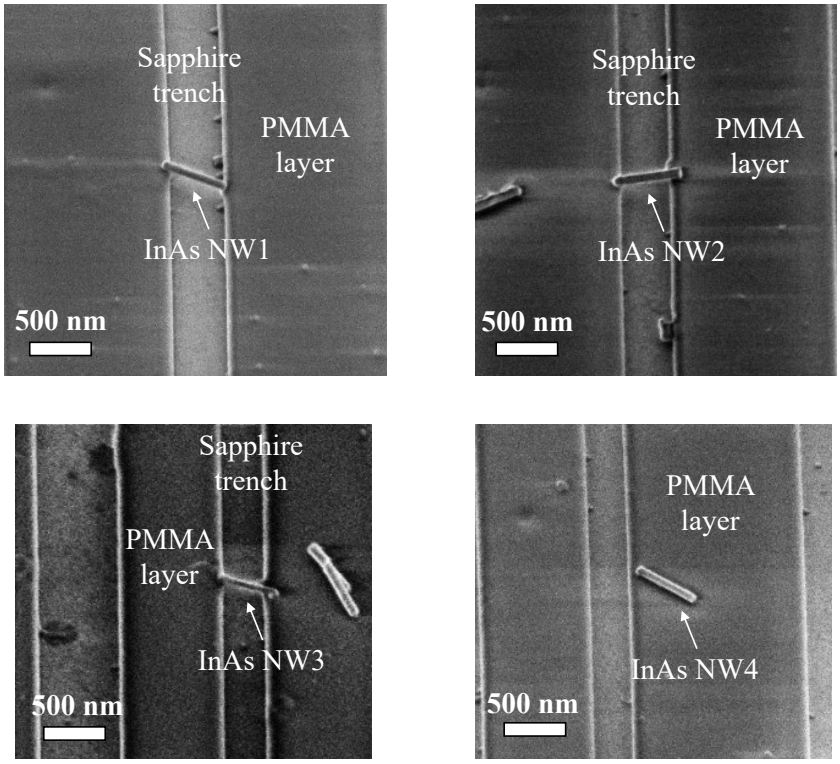

Figure 5.3: SEM images of type-S NWs, which are the subject of US investigation.

SEM characterization yielded NW diameter (D), length (L), and the total length of contact between the NW and the PMMA substrate (L_c). The latter is schematized in Figure 5.4. The properties of the four NWs selected for optical investigation are summarized in Table 5.1. Most of the NWs were found to display an Au nanoparticle embedded at one end. The Au nanoparticle served as the metallic seed acting as a catalyst during the growth procedure. The diameter of the Au nanoparticle is approximately $t \simeq 28$ nm and is included in the reported total length of the NWs.

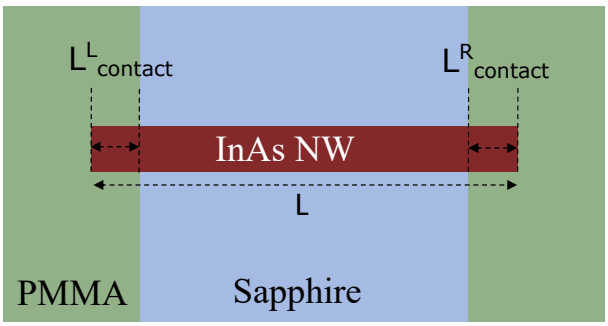

Figure 5.4: Schematics illustrating the top view of a NW with length L laying over a trench in the PMMA layer. The total length of contact between the NW and the PMMA substrate (L_c) is defined as the sum of the contributions at the two extremities: $L_c = L^R_{contact} + L^L_{contact}$.

NW-S characteristics			
	D [nm]	L [nm]	L_c [nm]
NW1	65 ± 6	528 ± 20	49 ± 10
NW2	77 ± 6	566 ± 20	164 ± 11
NW3	55 ± 6	477 ± 20	168 ± 15
NW4	65 ± 5	501 ± 20	501 ± 20

Table 5.1: Characteristics of the four NWs type S investigated in this work.

NWs-S were optically located via SMS. A representative SMS map of one NW (namely, NW1 in Table 5.1), along with a corresponding line-cut taken perpendicularly to the NW longitudinal axis (along the red dashed line), are shown in Figure 5.5.

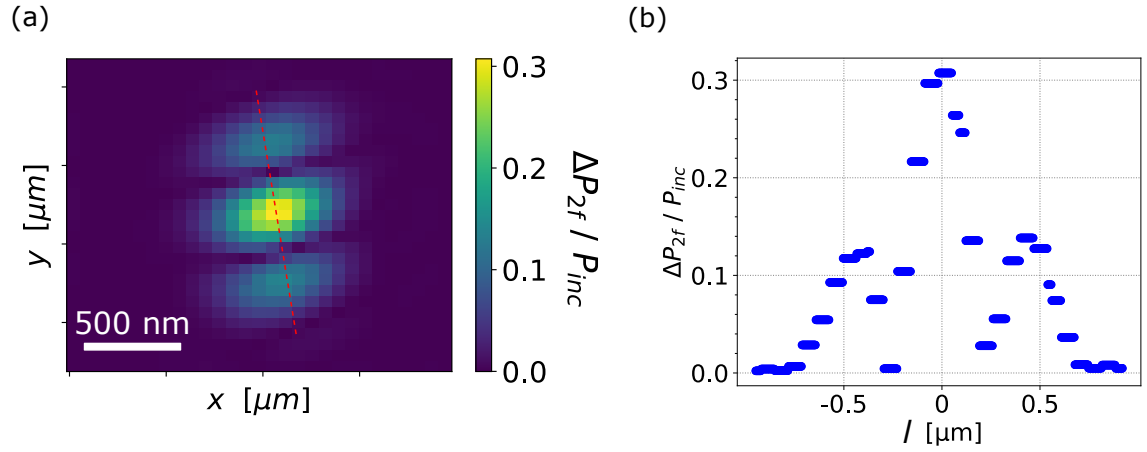

Figure 5.5: SMS map of NW1 over a 2 µm × 2 µm area acquired at $\lambda = 650$ nm (a), and line-cut across the center of the tri-lobed shape, orthogonal to the NW axis (see the red-dashed line reported in panel (a)) (b).

5.1.3 Polarization measurements

Once an individual NW is located, the orientation of its longitudinal axis relative to the laser beam polarization is determined through polarization-dependent ES, for both pump and probe beams. ES maps are acquired at a fixed wavelength λ, with the polarization direction of the incident laser beam varying in steps of 20°. For each map, acquired at a specific polarization direction, the ratio $\frac{P_{tr}^{NW}}{P_{tr}^{trench}}$ is calculated, where P_{tr}^{NW} is the power transmitted through the NW and P_{tr}^{trench} is the power transmitted through the trench. These ratios are plotted on a polar graph. Fitting the polar plot data allows retrieving the polarization component parallel to the NW axis, corresponding to the minimum transmitted power (minimum value of $\frac{P_{tr}^{NW}}{P_{tr}^{trench}}$), as well as the component perpendicular to the NW axis, corresponding to the maximum transmitted power(maximum value of $\frac{P_{tr}^{NW}}{P_{tr}^{trench}}$). The procedure is iterated for both pump and probe beams.

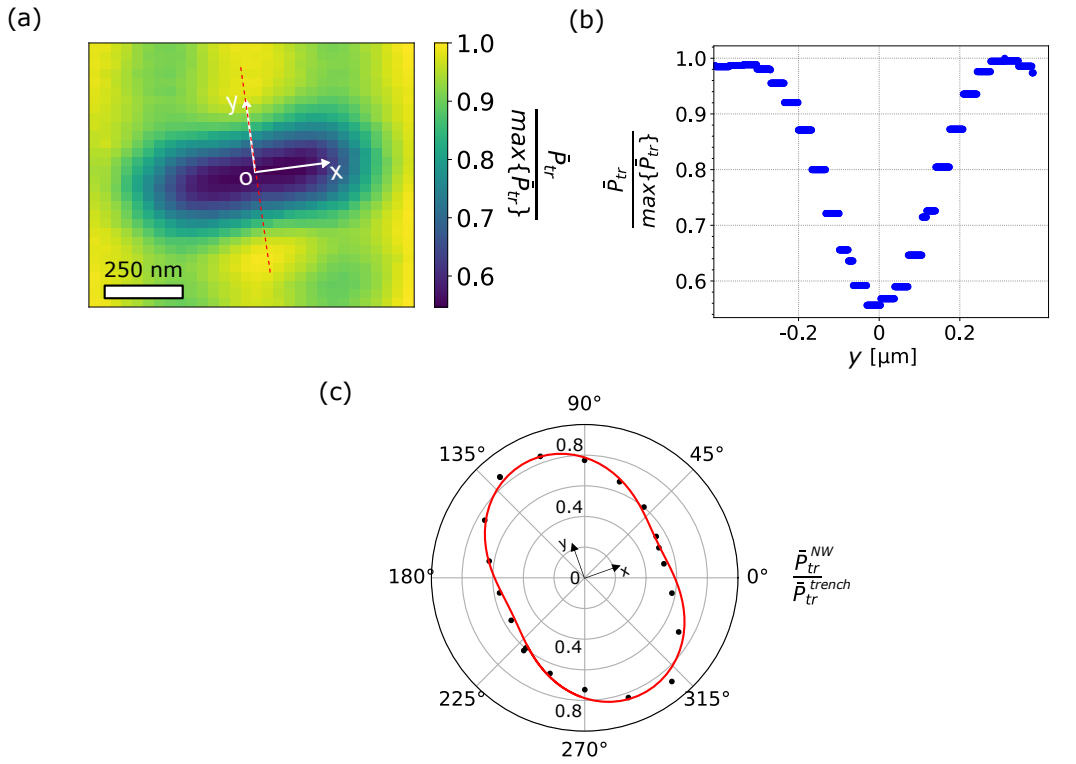

Figure 5.6: ES map of NW1 (blue shape) laying over the trench (central yellow stripe). Image acquired scanning an area of size 1 μm × 1 μm, at $\lambda = 410$ nm and light polarization parallel to the NW axis (a). Line-cut performed along the y direction, perpendicular to the NW axis (as indicated by the dashed line in panel (a)) (b). Polarization dependence of the power transmitted by the NW over the power transmitted by the trench at $\lambda = 410$ nm. Experimental data (black dots) are fitted with the red curve (c).

An ES map acquired on the representative NW1 at a wavelength of $\lambda = 410$ nm, at a

fixed polarization (parallel to the NW axis), over a scan area of 1 μm × 1 μm is shown in Figure 5.6a, with the line-cut along the segment perpendicular to the NW axis reported in panel (b). The polarization-dependent signal is shown in panel (c).

5.2 Time-resolved measurements

Once the NW is located under the collinear pump and probe incident beams and its orientation with respect to their polarization directions is known, the set-up is configured for pump-probe measurements (as detailed in Chapter 2). Pump and probe beams with approximately 100 fs long pulses were employed, and, due to technical constraints, wavelengths $\lambda_{pump} = 410$ nm and $\lambda_{probe} = 820$ nm were used for measurements on NWs-L, while $\lambda_{pump} = 410$ nm and $\lambda_{probe} = 650$ nm were used for the study of NWs-S. Both beams were polarized parallel to the NW axis, and their spot size was approximately at the diffraction limit. A probe power of $P_{probe} < 1$ μW (power measured at the entrance of the input objective) was used, while pump power of 6 μW and 50 μW were used. Powers were always measured at the entrance of the input objective. The time-resolved optical traces here reported were obtained spanning time-delay windows of either 1.35 ns or 3 ns depending on the particular need of each measurement (dictated by the trade-off between acquisition time and time resolution). The experimental data presented in the following two sections were obtained using the configurations described above and are analyzed with a focus on mechanical and thermal energy transfer.

5.3 Mechanical properties

As detailed in the introduction of this thesis, InAs NWs have attracted significant interest due to their potential in flexible [22, 54–56] and fast-response [48–53] nanoelectronics as well as electromechanical applications at the nanoscale [57–59]. Despite the interest in the mechanics, only a few works report on the response of InAs NW arrays to a thermo-mechanical stimulus [131, 158]. A comprehensive understanding of their mechanical properties is still lacking. The aim of this chapter is to expand knowledge on this topic focusing on the mechanical properties of *individual* (WZ) InAs NWs. In particular, the present study investigates, via US, the mechanical properties of individual nanostructures to correlate their mechanical behaviour with their morphological features. First, individual NWs are examined in the suspended-over-trench configuration, mimicking a free-boundary condition. This is at variance with previous experiments [131, 158] where a forest of vertically aligned NWs, each with one extremity anchored to the substrate,

characterized by a wide dispersion of geometric parameters was investigated. Then, the impact of the substrate is also explored. The extensional and breathing modes of the NWs in different configurations are identified and correlated to the stiffness matrix of InAs NWs.

5.3.1 Experimental results

The mechanical properties of InAs NWs (both type-S and type-L) were evaluated from the time-resolved optical traces. A representative pump-probe signal, obtained on NW1 (see Table 5.1), is shown in Figure 5.7, reporting the relative transmission variation as a function of the delay time between the pump and probe pulses. The signal is acquired

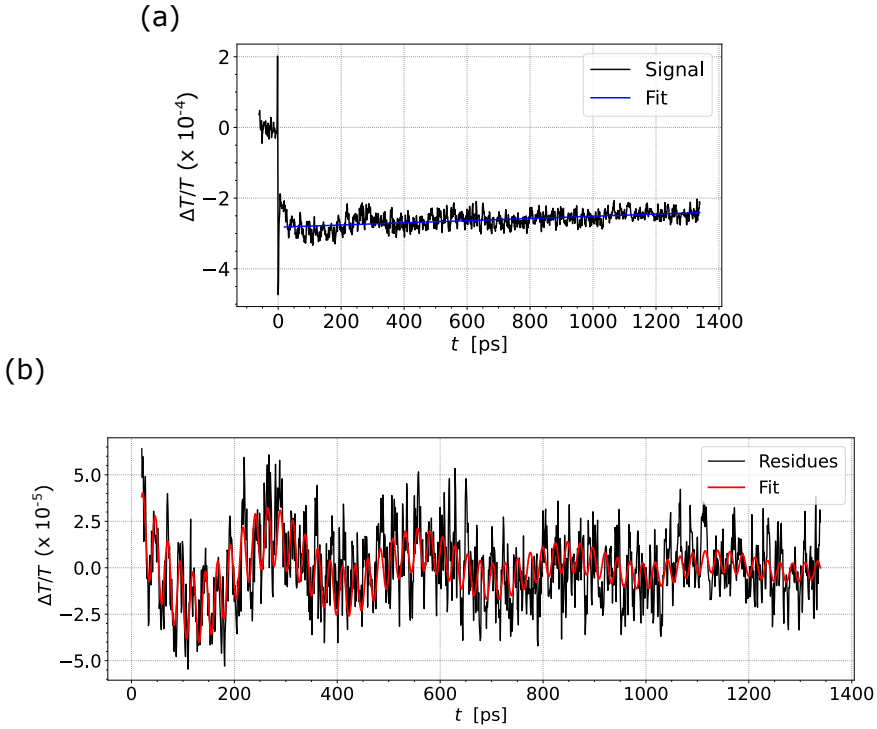

Figure 5.7: (a) Representative pump-probe signal acquired on NW1, reporting the relative transmission variation versus the delay time between the pump and probe pulses. Pump power P_{pump} = 6 μW and temporal resolution of 1 ps. (b) Residues obtained after subtracting from the optical trace the thermal contribution to the signal.

over a time-delay window of 1350 ps and for a pump power of 6 μW. Details of the signal processing procedure can be found in Chapter 1. Due to the long attenuation time (far exceeding the investigated time-delay window), the standard exponential fit was replaced with a linear fit, which was used to subtract the thermal part of the signal, thus isolating the residual oscillations. A fit using two damped oscillators was then performed to extract two distinct vibrational modes characterized by long (hundreds of ps timescale) and short

(tens of ps timescale) periods, respectively. The oscillation periods are ascribed to radial and longitudinal modes based on their linear dependence on the NW's diameter and length, respectively, as reported in Figure 5.8 and 5.9 and related discussions.

Concerning **type-S NWs** (see Figure 5.3), the characteristics of the dominant modes are summarized in Tables 5.2 and 5.3.

Parameters of the breathing mode in NWs-S			
	T [ps]	τ [ps]	Q
NW1	24 ± 1	643 ± 72	115 ± 14
NW2	31 ± 1	318 ± 77	33 ± 8
NW3	19 ± 2	/	/
NW4	20 ± 1	77 ± 10	12 ± 2

Table 5.2: NWs-S: short vibration periods (tens of ps), attenuation times and Q-factors extracted from the fit of the pump-probe signals. These periods are assigned to the breathing mode of the four NWs-S in Subsection 5.3.2. Attenuation times and Q-factors are retrieved from signals acquired with a pump beam power of 6 μW, measured at the entrance of the input objective.

Parameters of the longitudinal mode in NWs-S	
	T [ps]
NW1	280 ± 20
NW2	305 ± 10
NW3	340 ± 20
NW4	270 ± 40

Table 5.3: NWs-S: long vibration periods (hundreds of ps) retrieved from the fit of the pump-probe signals. These periods are assigned to the longitudinal mode of the four NWs-S in in Subsection 5.3.2. The τ and Q factors could not be confidently retrieved, from the fits, at variance with the case of the breathing modes. The explored time-delay window is here expanded to 3 ns.

The reported periods are calculated as the average of the results obtained from multiple measurement sets conducted at both low and high pump powers (6 μW and 50 μW, as measured at the entrance of the input objective). The attenuation times and Q-factors in Table 5.2 refer to measurements performed at 6 μW pump power. It is here anticipated that the modes are assigned to breathing (tens of ps periods) and longitudinal (hundreds of ps periods), as will be discussed shortly in Subsection 5.3.2. Additional

modes were observed under specific conditions. Specifically, NW2 exhibited a mode with $T = (1.37 \pm 0.02)$ ns at high pump power only. In similar conditions, NW3 showed a mode with $T = (37 \pm 1)$ ps. Further analysis of the modes with periods $T = (1.37 \pm 0.02)$ ns and $T = (37 \pm 1)$ ps have not been pursued, as: (a) they were observed in two NWs only and (b) they do not correspond to the *breathing* mode that is the primary focus of this study. In fact, their periods are longer than the fundamental breathing mode (the maximum period expected for the breathing mode) estimated from the analytical model (by far for the $T = (1.37 \pm 0.02)$ ns case, whereas $T = (37 \pm 1)$ ps is approximately twice the period of the fundamental breathing mode). Consequently, these modes are not expected to belong to the breathing mode family. For these reasons, and in the attempt to make definite claims in the debated issue of InAs NW mechanical properties, we opted to rely on fully consolidated evidence only, leaving out these in the following analysis.

Concerning the **type-L NW** (see Figure 5.1), modes were detected exclusively under a high pump power (60 μW, as measured at the entrance of the input objective), on a time delay window extended up to 3 ns. Specifically, for the measurement performed on the suspended NW portion (diameter $D = (101 \pm 6)$ nm and length $L \sim 6$ μm), only short periods (tens of ps) were detected, amounting to $T = (32 \pm 1)$ ps and $T = (73 \pm 5)$ ps. It is here anticipated that the former is attributed to the fundamental radial mode, as will be detailed in Subsection 5.3.2. The mode with period $T = 73$ ps, on the other end, escaped a clear assignment. No clear oscillations were observed when the measurement was performed on the NW portion in contact with the PMMA layer.

No long-period modes, suggestive of longitudinal modes, were detected for the NW-L. The absence of the fundamental longitudinal mode in this case can be ascribed to different reasons. First, the fundamental period associated with the extensional mode for a NW of $L = 6$ μm is estimated to be $T \simeq 3$ ns, using Equation 1.13 and a sound velocity $v_s = 4130$ m/s [131]. This period is challenging to detect as it matches the extent of the maximum time-delay window accessible with the optical setup (3 ns). Second, the mechanism triggering mechanical oscillations in such long nanostructures, i.e., the absorption of a pump pulse with an optical spot size significantly smaller than the NW length, does not efficiently excite the fundamental longitudinal mode. As a matter of fact, in the case of NW-L, the pump beam excites a displacement wavepacket, along the NW long axis, with a characteristic size comparable to the diameter of the pump beam spot on the NW. A broad range of NW eigenmodes hence contributes to the wavepacket spectral content. Differently, in the case of NWs with lengths similar to the beam spot diameter, the NWs are uniformly excited by the pump beam, and hence a few longitudinal eigenmodes (the fundamental one overall) are excited, rather than a wavepacket.

5.3.2 Analysis

In this section, the time-resolved optical traces are first rationalized on the basis of the analytical theory for high aspect-ratio, homogeneous and isotropic cylinders. Fits of the experimental data for both longitudinal (longitudinal mode period vs. L) and radial breathing modes (radial breathing mode period vs. D) yield effective Young modulus and Poisson ratio for the InAs NW. The values are reasonable, nevertheless some discrepancies arise with respect to previous reports. A more refined analysis is then performed based on FEM modeling, which allows to relax the hypothesis inherent to the analytical model. Among the improvements is the introduction of a stiffness matrix for WZ InAs NW, thus accounting for the anisotropy of the material in the solution of the acoustic problem. The outcome of FEM simulations matches experimental data. This result, on one side, rationalizes the acoustic dynamics, on the other, it validates the stiffness matrix theoretically proposed for WZ InAs NWs, the detection of both longitudinal and radial breathing modes being key to the task. The quality factor (Q-factor) of the radial breathing mode is then investigated as a function of the extent of the contact between the NW and the supporting substrate. This allows to address the relevance of the intrinsic versus extrinsic mechanical attenuation mechanisms, a key aspect in nanomechanics.

These results were achieved thanks to measurements performed on individual (as opposed to an ensemble) InAs NWs. This fact underlies once more the importance of the developed experimental technique for mechanical nanometrology applications.

Longitudinal modes

Long-period oscillations of NWs-S (NW1, NW2 and NW4) versus NW length are reported in Figure 5.8 (black dots). The period scales linearly with L, with values in the hundreds of ps. These evidences support the attribution of these modes to longitudinal NW modes. A preliminary rationalization of these results is performed by adopting the model for high aspect-ratio cylinder addressed in Subsection 1.2.1.

It is worth recalling that the model was developed for homogeneous and isotropic cylinders, hence it describes the NW elasticity via two parameters only: the Young's modulus E and Poisson's ratio ν. E and ν are to be considered as "effective" elastic parameters. In fact, given the anisotropy of the InAs NW, a full mechanical characterization requires a stiffness matrix depending on more than two elastic parameters. This point will be addressed further on.

Fit to the experimental data (dashed line) with Equation 1.13, upon fixing the WZ InAs density $\rho = 5670$ kg/m^3, yields a longitudinal Young's modulus $E = (79.6 \pm 0.8)$ GPa. This value of E is in agreement with the average value of E for InAs NWs reported

in the paper from Lexholm et al. [79] (average taken over the same range of diameters here reported).

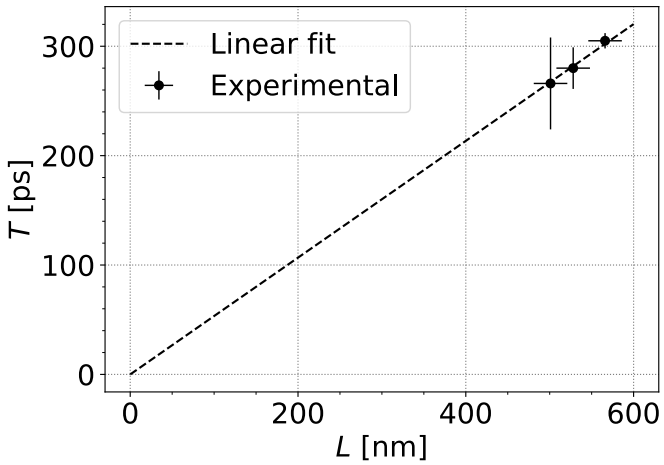

Figure 5.8: Longitudinal mode periods. Long period oscillations of NWs-S (NW1, NW2 and NW4) versus NW length (black dots). NW3 is excluded from this analysis due to its morphological features at the extremities biasing the longitudinal period. Linear fit to the experimental data (dashed line) adopting Equation 1.13, with fixed WZ InAs density $\rho = 5670$ kg/m^3 [131]. A longitudinal Young's modulus $E = (79.6 \pm 0.8)$ GPa was retrieved from the fit.

The dispersion of the E values was though large, amounting to (78 ± 18) GPa for $D \sim 80$ nm, that is amounting to a 23 % uncertainty. Relevant to the following discussion is the way in which E was retrieved in the above-mentioned article. The authors measured the eigenfrequencies of the NW bending mode via a stroboscopic technique, thus with an all-optical non-contact technique. They then extracted the Young modulus fitting the data with the Euler–Bernoulli equation for an ideal geometry. This procedure is conceptually quite close to the one here adopted up to now. The value of 79.6 GPa is though off with respect to the value of 96.7 GPa reported by some of us [131] measuring the same longitudinal mode on a forest of vertically aligned, substrate-bound InAs NWs, synthesized in similar conditions as the present NWs. E was extracted from time-resolved optical measurements performed via Asynchronous Optical Sampling (ASOPS). The measurements were though performed on an ensemble of NWs affected by a wide size dispersion. The question then arises as to the origin of these discrepancies. Is the retrieved value of $E = 79.6$ GPa correct or something went missing in the interpretation/retrieval procedure? This question is postponed until after the analysis of the radial modes, which will furnish further indications.

A technical note is here due regarding the experimental data. The long oscillation

period measured on NW3 was excluded from the longitudinal mode analysis (it is not reported in Figure 5.8). This period deviates from the linear trend. SEM images indicate that NW3 extremities are embedded within the PMMA layer, resulting in altered boundary conditions. These conditions likely lead to a longer longitudinal vibrational period compared to the predicted value, while not affecting the radial mode, which is instead dominated by the displacement in the radial direction along the entire length of the NW, hence less affected by morphological deviations occurring at the extremities only. Concerning the experimental observation that a NW with embedded extremities exhibits a longitudinal vibrational period longer than its free-ends counterpart, we propose a qualitative rationalization. When the extremities of the NW are embedded and the NW is thermo-mechanically excited, the region of PMMA embedding the extremities of the NW deforms to some extent. The PMMA-loaded NW can be regarded as having an effective length $\bar{L} > L$, which results in a longer oscillation period. This scenario, although likely, should be verified taking into account (i) the precise extent to which the NW is embedded and (ii) the extent of the PMMA portion that is affected by the NW longitudinal displacement. Unfortunately, these details are missing and would require a dedicated investigation which is out of the scope of the thesis.

Radial modes

Short-period oscillations of NWs-S (NW1 to NW4) and NW-L are reported in Figure 5.9 (black dots). The period scales linearly with D, with values in the tens of ps. This evidence supports the attribution of these modes to radial NW modes, specifically to breathing modes. Similarly to the analysis of longitudinal modes, a preliminary rationalization of these results is performed by adopting the model for high aspect-ratio cylinders addressed in Subsection 1.2.1. Fit to the experimental data (dashed line) with Equation 1.14, upon fixing $\tau_0 \sim 2.04$ [158], WZ InAs density $\rho = 5670$ kg/m^3 [131] and longitudinal Young modulus $E = 79.6$ GPa (as obtained from the longitudinal mode analysis), yields a Poisson's ratio $\nu = 0.32 \pm 0.03$.

This value of the Poisson's ratio can be compared against the value $\nu \sim 0.22$ reported in the literature for InAs NWs (although of different lengths and dimensions) [158]. The measurements from which the value was retrieved were based on time-resolved X-ray diffraction. In this sense, the technique is to some extent similar to the one adopted in this thesis and the results should be, at least from the technique's point of view, comparable. To appreciate the extent of the deviation, it is recalled that theory requires $0 < \nu < 0.5$. Again, as for the case of the longitudinal modes, the question arises as to the significance of these discrepancies. This issue will be addressed in the following

section.

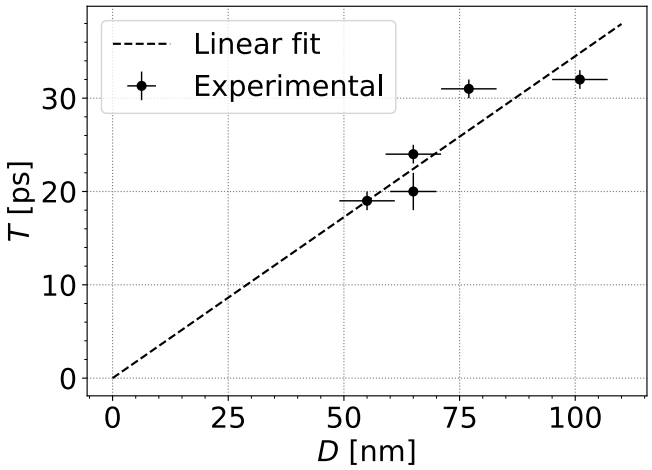

Figure 5.9: Breathing mode periods. Short period oscillations of NWs-S (NW1 to NW4) and NW-L ($D \sim 101$ nm) versus NW diameters (black dots). Linear fit to the experimental data (dashed line) adopting Equation 1.14, with fixed $\tau_0 \sim 2.04$ [158], WZ InAs density $\rho = 5670$ kg/m^3 [131] and longitudinal Young modulus $E = 79.6$ GPa (from the longitudinal mode analysis). A Poisson's ratio $\nu = 0.32 \pm 0.03$ was retrieved from the fit.

FEM modeling of the acoustic problem and stiffness matrix of InAs NWs

The values of the elastic properties, retrieved fitting the experimental data with a simple analytical model, are reasonable numbers for the effective E and ν, nevertheless, some discrepancies with previous measurements did arise. Furthermore, a thorough understanding of InAs NWs' mechanical properties requires accessing the stiffness matrix. In the following, possible causes that might affect the values of the elastic constants are addressed. The ansatz is that the major criticality in the retrieval of the elastic properties stands in the adoption of an oversimplified model to fit the experimental data. A full FEM model is then introduced, relaxing all the approximations of the analytical model and describing the elastic problem in terms of a theoretical stiffness matrix. FEM simulations based on this model match the experimental longitudinal and breathing modes, while providing displacement fields with a correct symmetry. On one hand, these results confirm the correctness of the ansatz; on the other hand, they provide a benchmark for the elastic stiffness matrix of InAs NWs.

The above-mentioned discrepancies in the values of the elastic constants could arise because of structural differences in the probed samples or oversimplification of the fitting model. As for the material, the samples probed in the present thesis are not purely

WZ InAs but rather polymorphic. This is well represented in the TEM images of NWs reported in Figure 3.6. These images were taken from NWs sorted from the same batch as the one measured in this thesis work. The images clearly show the presence of stacking faults. Although it was not possible to perform a statistical investigation to provide the actual percentage of stacking fault per unit length of the NWs, the images suggest the presence of phases other than WZ. This is coherent with literature results where InAs NWs have been reported [159] to switch from WZ to Zincblende (ZB) structure as the NW diameter increases from a few tens of nm to beyond 100 nm. The diameters of the NWs object of the US measurements spanned from 55 to 100 nm. This suggests, on the one side, that the effective E and ν values here extracted are actually values weighted on different polymorphic configurations (encompassing WZ and possibly ZB), on the other, that the crystal structure of the NWs here explored could be different from the one explored in the other two mentioned works. For instance, in Gandolfi et al. [131] the probed NWs had diameters with average values of either 20 nm or $\sim$ 40 nm with a clear WZ structure. That said, we believe this not to be the dominant reason behind possible disagreements, at least regarding the E value. As will be addressed further on, the ZB InAs crystal, when viewed in the spatial reference system with an axis parallel to the cube diagonal (as for the case of the InAs (111)B substrate), looks similar to the unit cell of WZ InAs [160], hence the Young's modulus should be similar too [161, 162]. The ansatz is here made that discrepancies are due to the oversimplified analytical model adopted to fit the longitudinal and breathing modes periods. Equations 1.13 and 1.14 were derived assuming (i) a cylindrical geometry, whereas the InAs NWs have hexagonal cross-section; (ii) a *high* aspect-ratio, whereas for the NW-S sample the ratio $L/D \sim 8$; (iii) a homogeneous material, not certainly the case due to the presence of the metallic (Au) catalyst nanoparticle at the NW tip; (iv) an isotropic material, not certainly the case for an InAs NW.

In order to remedy to these limitations, a FEM model was developed accounting for both the actual InAs NW morphological features (remedy to points i-iii) and the InAs NW stiffness matrix (remedy to point iv). The idea is to verify if the experimental results can be rationalized on the basis of a refined model. Should this be the case, the proposed InAs NW stiffness matrix would also be validated against the experimental results. The model was implemented in the Solid Mechanics module of COMSOL Multiphysics. A 3D geometry was considered. Each NW was modeled as a prism with a hexagonal cross-section. The principal diagonal of the hexagon is defined as the diameter of the nanostructure. The prism length is defined as the length of the InAs NW only, that is without considering the Au catalyst (at variance with respect to the length used in the

analytical model). The prism length and the length of the hexagon diagonal were both derived from SEM images. The gold catalyst was modeled as a hemispherical tip, with its circular cross-section circumscribing the NW's hexagonal cross-section.

One of the key challenges in modeling InAs NWs is determining the mechanical properties to assign to them. This is complicated by the fact that WZ InAs does not occur naturally as a bulk crystal. However, it is observed that the ZB InAs crystal, when viewed from a specific spatial reference system with an axis aligned with the cube diagonal (similar to the InAs (111)B case), exhibits a unit cell structure that closely resembles that of WZ InAs [163]. Based on this similarity, the rotated bulk ZB InAs stiffness matrix is used as a proxy for the mechanical properties of WZ InAs NWs. The InAs stiffness matrix in the rotated frame reads [131]:

$$C'\,(\mathrm{GPa}) = \begin{pmatrix} 103.9 & 38.6 & 31.7 & 0 & -9.7 & 0 \\ 38.6 & 103.9 & 31.7 & 0 & 9.7 & 0 \\ 31.7 & 31.7 & 110.7 & 0 & 0 & 0 \\ 0 & 0 & 0 & 25.8 & 0 & 9.7 \\ -9.7 & 9.7 & 0 & 0 & 25.8 & 0 \\ 0 & 0 & 0 & 9.7 & 0 & 32.7 \end{pmatrix} \tag{5.1}$$

The density of WZ InAs was set to $\rho = 5670$ kg/m^3.

The mechanical eigenvalue problem for the above-mentioned model is then solved. Formally, this means solving Navier's equation (i.e. the dynamic equation of elasticity, see Subsection 1.2.1) in the frequency domain, imposing zero-stress boundary conditions on all external surfaces. To this end, a triangular mesh was applied to the NW base and swept along the NW axis. A tetrahedral mesh was used for the gold tip.

Eigenmodes with physically sound displacement fields (see Figure 5.11 for an example) were found with periods matching the experimental ones. Figure 5.10 reports, for each NW-S, the calculated eigenperiods (red markers) falling close to the experimental one and bearing a displacement field compatible with a longitudinal mode (panel a) and to a radial mode (panel b). Numerical results show good agreement with experimental data (black dots) within the error bars. Note that numerical eigenperiods reported in Figure 5.10b are shown with an error bar. For each NW-S, multiple radial modes with periods close to the experimental one resulted from the simulation. The average of the values closest to the experimental one was considered, with an error bar accounting for the dispersion of more period-wise distant modes. We recall that the experimental value for the longitudinal mode only of NW3 was not considered because the extremities were embedded within the PMMA layer, resulting in altered boundary conditions. Nevertheless, we calculated the longitudinal mode within the FEM model (assuming nominal boundary conditions);

the eigenperiod is reported as a red triangle in Figure 5.10a and aligns well with a linear trend.

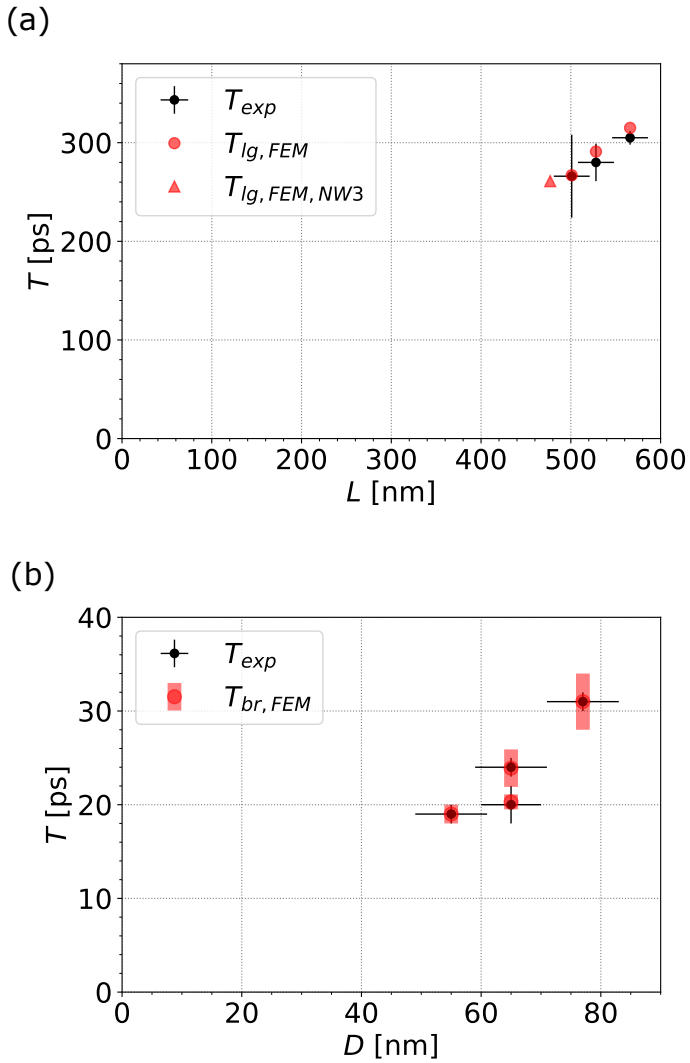

Figure 5.10: Mode periods from FEM simulations (red markers) vs. experimental periods (black markers) for NWs-S. Refer to Table 5.1 for a correspondence of the reported values with each specific NW-S. (a) Longitudinal mode periods. The experimental value for the longitudinal mode of NW3 is not reported (NW3 extremities are embedded in PMMA, resulting in altered boundary conditions). Nevertheless, the calculated longitudinal mode (assuming nominal boundary conditions) is reported as a red triangle and aligns well with a linear trend. (b) Radial breathing mode periods. Error bars (red rectangles) are included for $T_{br,FEM}$, as discussed in the main text.

Short-period radial modes were quite challenging to address, as their periods often overlap with longitudinal and torsional modes' periods of higher order. This occurs because the diameter D (primarily responsible for the radial mode period $T_{br} \propto D$) is shorter than the NW length L (primarily responsible for the longitudinal mode $T_{lg} \propto L$).

Hence, it often occurs that the period of a low-order radial mode falls in close proximity to a high-order longitudinal (and torsional) mode. Nevertheless, resonant frequencies with radial symmetry were identified in the FEM simulations and found to align with experimental observations. Torsional modes, although numerically predicted with periods in closed proximity to the experimental periods, were not considered, since they cannot be excited in the experiment. In fact the symmetry of their displacement is orthogonal to the initial displacement triggered by a Gaussian laser pump pulse[1].

Regarding NW4 ($D = (65 \pm 5)$ nm, $L = (501 \pm 20)$ nm), which in the experiment was deposited on PMMA (SEM image in the bottom left panel in Figure 5.3), it is worth noting that, although the FEM model did not include the substrate, it successfully recovered the correct longitudinal eigenmode period of 270 ps, as shown in Figure 5.10a. This suggests that the PMMA substrate has minimal impact on the longitudinal mode period.

We now address the longitudinal or radial character of the modes in the realistic scenario mimicked by the FEM model. Figure 5.11 shows the calculated displacement fields for the case of NW1 ($D = (65 \pm 6)$ nm, $L = (528 \pm 20)$ nm). Panel (a) shows the displacement field of the eigenmode with calculated period of $T = 291$ ps. The displacement field is clearly oriented along the NW axis, justifying the assignment of this mode to a longitudinal mode. Panel (b) shows the displacement field of the eigenmode with calculated period of $T = 24$ ps. The displacement field has both radial and longitudinal components, the former being prevalent. This justifies the assignment of this mode to a breathing radial mode. The displacement field, here reported for the specific case of NW1, is representative also for the results obtained for the other NWs.

The agreement between FEM simulations and the experimental data validates the stiffness matrix for WZ InAs NWs, C', against both longitudinal and breathing modes. C' may thus be exploited within relevant scenarios of applied stress, such as those resulting from thermal expansion, or from the application of stresses/loads inducing strain along the NW's longitudinal or radial axis. Although the benchmarking based on longitudinal and breathing modes only is not sufficient to validate *all* the elements of C', the present results constitute an important step forward, allowing C' to be adopted to make predictions in most situations of applicative relevance.

[1] Actually, deviations from the ideal geometry may somewhat relax the orthogonality, nevertheless the excitation efficiency would remain very low as compared to the radial and longitudinal modes.

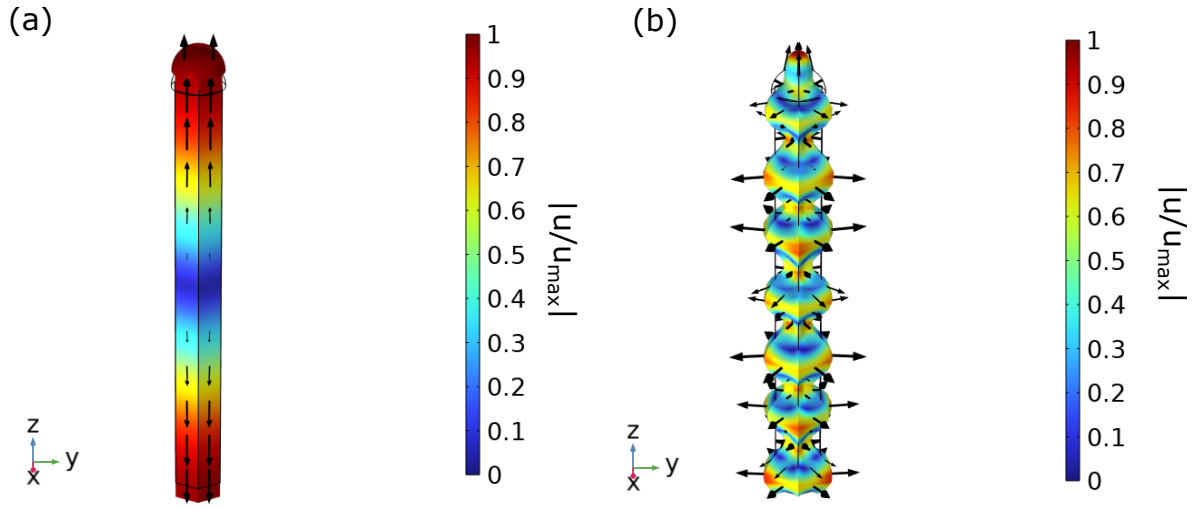

Figure 5.11: Displacement field of the longitudinal (panel a) and breathing (panel b) modes calculated from FEM simulations for the representative case of NW1. The calculated mode periods are $T = 291$ ps (panel a) and $T = 24$ ps (panel b). The color scale represents the magnitude of the displacement, normalized to its maximum value. The arrows indicate the displacement vector, while the black lines denote the reference (not-deformed configuration). The colored shape represents the configuration deformed by the displacement. The semispherical Au tip is positioned at the top extremity of the NW.

Appendix: technical comments on InAs NW stiffness matrix C'.

In order to account for the radial breathing modes, the NW cross-section had to be taken as hexagonal. If one were to adopt a circular cross-section instead, as is commonly the case to work out analytical models [127, 128] (usually applied for isotropic crystals), the elastic stiffness matrix for the WZ structure (which has hexagonal symmetry) would not be compatible with a NW of circular cross-section. During the thesis work, FEM simulations were implemented also to test for the latter case (not reported in the manuscript), resulting in unphysical eigenmodes displacements fields in the radial direction. The stiffness matrix imposes constraints on the eigenmodes displacements that are not compatible with a circular boundary. The circular cross-section approximation, on the other hand, remains valid for addressing the NWs longitudinal vibrational modes [131], whose displacement oscillates primarily along the [111] direction and is ruled by a combination of the stiffness components C'_{11}, C'_{12}, C'_{13}, C'_{33}, the latter being the most relevant. The stiffness matrix terms C'_{15}, C'_{25}, C'_{46} (and their symmetric), on the other hand, are relevant to correctly access the breathing mode but are of no concern to the longitudinal ones. Measurements of the breathing mode period thus allow to test the stiffness matrix also for

these terms, which was not possible with the longitudinal mode. The analytical derivation of the breathing mode period as a function of the stiffness matrix elements C'_{ij} is not straightforward, at variance with the case of longitudinal modes. The testing method for the validity of the stiffness matrix is thus based on numerically simulating the breathing mode period by incorporating the stiffness matrix to be validated, and then verifying the accuracy of the simulated period by comparing it to the experimentally measured period. In the future, it would be desirable to test the sensitivity of the breathing mode period to the single stiffness matrix components to determine if there is a dominant term ruling the oscillation.

Attenuation

The impact of the substrate on the attenuation of mechanical vibrations is now addressed. The acoustic attenuation time, τ_{br}, (or the oscillation quality factor, $Q_{br} = \pi\tau_{br}/T_{br}$, which, for a given T_{br}, is proportional to τ_{br}) could be confidently retrieved for the breathing mode of NW1-S, NW2-S and NW4-S (see Table 5.2). Of concern to the mode attenuation time, these three NWs differ by the extent of their contact with the PMMA substrate (see Table 5.1). Figure 5.12 reports τ_{br} as a function of L_c/L, where, it is recalled, L_c and L indicate the contact length and the total length of each NW, respectively.

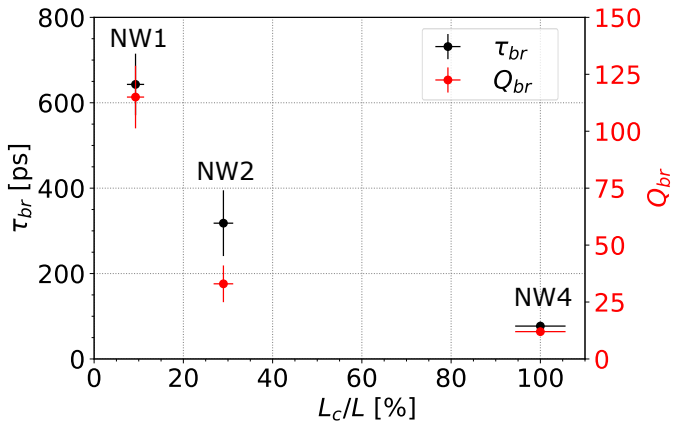

Figure 5.12: Attenuation time τ_{br} (left axis, black dots) and quality factor Q_{br} (right axis, red dots) of the breathing mode measured on NW1-S, NW2-S and NW4-S versus L_c/L. NW4-S completely adheres to the PMMA substrate.

Attenuation of a mechanical oscillation in a nanosystem occurs through two parallel channels. *Extrinsic* (also called *radiative*) attenuation arises from the radiation of acoustic energy from the nanosystem to the surrounding environment. This is due to the contact with the supporting substrate (the attenuation to air is negligible in comparison

and is here neglected). If a nanosystem has no contact, its extrinsic attenuation time, τ_{ext}, diverges (assuming the system to be in vacuum). *Intrinsic* attenuation is due to intrinsic losses within the material, ultimately converting elastic energy to heat. Intrinsic attenuation is always active irrespective of the presence or absence of contact.

A major quest in nanomechanics is to identify the dominant dissipation mechanism and estimate its corresponding attenuation time. This is particularly true for attenuation of oscillations in the hypersonic frequency range, as in the present case. To address this point it is convenient to work with attenuation rates, defined as $\Gamma_{br} = 1/\tau_{br}$, $\Gamma_{int} = 1/\tau_{int}$ and $\Gamma_{ext} = 1/\tau_{ext}$ for the total, intrinsic and extrinsic attenuation, respectively. Let's then consider a generic infinitesimal cross-sectional slab of the NW. If the slab is in contact with the PMMA substrate, it can radiate acoustic energy toward it at a radiation rate Γ_{ext}. If the slab is located within the suspended portion of the NW, it is assumed to be non-radiative, hence $\Gamma_{ext} = 0$. On the other hand, the same slab is always affected by intrinsic attenuation, no matter if it is located in the portion of the NW in contact with PMMA or in the suspended portion of the NW. Note that, within this definition, Γ_{ext} is an intensive quantity, just like Γ_{int}. For a NW of total length L and contact length L_c this ansatz translates to:

$$\Gamma_{br} = \Gamma_{int} + \frac{L_c}{L}\Gamma_{ext} \tag{5.2}$$

The experimental data Γ_{br} versus L_c/L are reported together with the linear fit to Equation 5.2 in Figure 5.13.

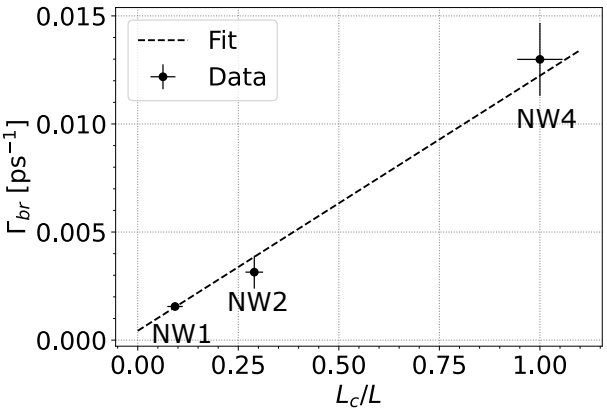

Figure 5.13: Attenuation rate relative to the breathing mode measured on NW1-S, NW2-S and NW4-S versus L_c/L.

The fit yields a value of $\Gamma_{ext} = (0.0120 \pm 0.0020)$ ps^{-1} and $\Gamma_{int} = (0.0004 \pm 0.0003)$ ps^{-1}, resulting in $\tau_{ext} = (84 \pm 14)$ ps and $\tau_{int} = (2500 \pm 1900)$ ps. Despite the large uncertainty on τ_{int}, the present result yields an order of magnitude estimate. Extrinsic attenuation

thus prevails by far in InAs NWs with oscillation frequencies in the GHz range. The significance of this result is best appreciated in the case of a NW fully adhering to the PMMA substrate, as is the case for NW4. In Equation 5.2 the term $(L_c/L)\Gamma_{ext}$ reduces to Γ_{ext} and extrinsic attenuation takes 84 ps, versus 2500 ps that would be required if only intrinsic attenuation were present (as it would be for the Gedanken case of no contact: $L_c = 0$).

A comment is here due regarding possible other reasons responsible for the trend reported in Figure 5.12. Actually, one could argue that differences in τ_{br} could be due to the NWs having different diameters instead of different contacts lengths with the substrate. In fact, the NW diameter D is another parameter that may affect τ_{br} through the extrinsic damping time, τ_{ext}. The reason may be appreciated in analyzing the case of the breathing mode of a film fully adhering to a substrate, since it provides a simple analytical formula relating τ_{ext} to the film thickness, h. Specifically, the film breathing mode is damped with a $\tau_{ext} \propto h$ [99, 164]. The breathing mode may be seen as the sum of two plane waves counter-propagating across the film thickness to form a stationary wave. When the film is brought into contact with the substrate, at each period of oscillation the plane wave encounters the film-substrate interface, hence losing some energy toward the substrate. This is the essence of extrinsic damping. The thicker is the film, the longer is the oscillation period of the wave, hence the longer is the time laps between two successive arrivals of the wave to the interface. In analogy to the film case, it is hence expected that the breathing mode attenuation time of the NW, τ_{br}, should be an increasing function of D. However, if the attenuation time measured for NW1-S, NW2-S and NW4-S were due to the different NWs diameters, NW1 and NW4 should show the same τ_{br}, whereas NW2 should show the highest τ_{br}. These are certainly not the cases, the experiment showing $\tau_{br,NW1} > \tau_{br,NW2} > \tau_{br,NW4}$, as clearly reported in Table 5.2 and Figure 5.12.

5.4 Thermal behaviour

The versatility of InAs NWs in various applications, including electronics [48–53] and thermoelectricity [47, 73, 74], highlights the importance of investigating thermal energy transfer in these nanostructures. This is particularly relevant for applications that require efficient heat management.

In this study, US measurements were used to investigate the thermal relaxation behaviour of both suspended and substrate-supported NWs. The investigation of thermal behavior in InAs NWs relies here on a more qualitative methodology, as compared to the analysis of mechanical response. The technical challenges in measuring pump-probe

signals on individual NWs transfer prompted the creation of a new metric for thermal metrology. The metric was developed to recover the features that underline the thermal response in NWs also in presence of noisy signals affected by repeatability issues. Finally, the thermal boundary conductance at the NW-PMMA interface was retrieved.

5.4.1 Metric for thermal metrology

Pump-probe measurements on nanoscale systems can prove challenging. The optical signals are affected by the mutual misalignment and/or defocusing of pump and probe beams (focused close to the diffraction limit, i.e with diameters in the hundreds of nm range at the exploited wavelengths), as well as to the alignment of the beams with respect to the nano-object. These issues become critical when measuring dynamics requiring delay-time up to the ns, requiring beams alignment to be secured for iterated optical delay-line translations $\sim$ 0.45 m. The situation is further exacerbated in the case of a NW suspended over a soft polymeric trench. The NW has a small contact surface with PMMA and only lays on it as a result of drop-casting (it is not tightly anchored). Furthermore, PMMA stability is not comparable to that of a hard substrate and can be modified under protracted beam exposure. The NW position may thus slightly drift in time. All these instances imply that the time-resolved traces may vary somewhat in successive measurements, hindering repeatability over the entire time-delay range. This issue is of limited impact when investigating the mechanics, the information being retrieved from an oscillating signal, which remains robust throughout repeated measurements. On the other hand, repeatability issues severely affects the analysis of the thermics, the information on the thermal dynamics being encoded in the the relaxation background of the signal. For this reason, an analysis based on fitting the optical signal on the entire time-resolved window was not applicable to access the thermal dynamics in InAs NWs. These challenges require devising a metric, capable of identifying stable features across different signals, that provide information on the thermal transients. Recently, strategies based on unsupervised clustering techniques applied to time-resolved optical traces have been proposed [165]. These strategies though require a wide data set and are best suited for a high throughput technique such as ASOPS [166, 167], as opposed to a delay-line based pump and probe scheme, as adopted in the present thesis.

In this thesis a physics-informed metric is proposed, that can be applied on a single pump and probe trace. The time-resolved signals were first normalized against the relative transmittivity variation measured at t=100 ps, $\frac{\Delta T}{T}|_{100ps}$, see Figure 5.14. At this delay time, the faster dynamics associated with electron-hole pair generation and relaxation have completely ended, leaving the pump-probe signal associated solely with thermal

dissipation dynamics. This normalization allowed the comparison of time-resolved signals acquired on different nanostructures. Two parameters were identified to characterize the underlying thermal phenomena:

- **signal average for $t < 0$:** $\frac{\Delta T}{T}|_i$. The signal for $t < 0$ represents the tail of the dynamics triggered by the previous pump pulse excitation, see Figure 5.14. Being the repetition rate of the laser $f_{RR} = 80$ MHz, this corresponds to a maximum pump-probe delay of $T_{RR} = 1/f_{RR} = 12.5$ ns separating two successive pump pulses, hence $\frac{\Delta T}{T}|_i$ entails the system's response at a delay time of ~ 12.5 ns after its excitation by a pump pulse. For a fast enough relaxation one has to expect $\frac{\Delta T}{T}|_i$=0, indicating thermal relaxation back to the original system temperature (i.e. the temperature of the system before the arrival of the first pulse, i.e. ambient temperature). This is indicative of no average energy accumulation within the system caused by the train of pump pulses. However, $\frac{\Delta T}{T}|_i$ is often found to exceed zero in these experiments. This means that, within the first μs to ms of the experiment (in the laboratory time, not to be confused with time-delay), the nanostructure does not relax to equilibrium, leading to an accumulation of energy in the system until an equilibrium condition at a higher temperature is reached (at a laboratory time $\sim$ µs to ms after the pump beam was originally switched on). A finite value of $\frac{\Delta T}{T}|_i$ is thus indicative of a system that did not have time to thermalize to the initial ambient temperature Summarizing, a vanishing $\frac{\Delta T}{T}|_i$ is indicative of a good thermal relaxation, whereas a finite value of $\frac{\Delta T}{T}|_i$ (actually of its modulus) is indicative of a poor thermal relaxation. A similar behavior has been reported in the literature, in the case of Permalloy thin films on Si substrates [97] and gold nanoparticles in contact with substrates of nanometric thicknesses [168].

- **difference between signal levels at short ($t = 100$ ps) and long ($t = 2.5$ ns) time scales:** $\frac{\Delta T}{T}|_{100\ \mathrm{ps}} - \frac{\Delta T}{T}|_f$. The signal value at a time delay $t \simeq 100$ ps, $\frac{\Delta T}{T}|_{100\ \mathrm{ps}}$, is compared to the signal at the end of the spanned time-delay, $\frac{\Delta T}{T}|_f$. $\frac{\Delta T}{T}|_f$ is taken as the average value of $\frac{\Delta T}{T}$ calculated between 2.4 ns and 2.6 ns. The parameter $\frac{\Delta T}{T}|_{100\ \mathrm{ps}} - \frac{\Delta T}{T}|_f$, visualized in Figure 5.14, is indicative of the thermalization effectiveness. A minute value of $\frac{\Delta T}{T}|_{100\ \mathrm{ps}} - \frac{\Delta T}{T}|_f$ is indicative of a slow thermalization (the signal at 100 ps and at the end of the probed delay-windows are similar), whereas an high value of $\frac{\Delta T}{T}|_{100\ \mathrm{ps}} - \frac{\Delta T}{T}|_f$ is representative of a fast thermal relaxation of the system, see Figure 5.14.

Summarizing, both $\frac{\Delta T}{T}|_i$ and $\frac{\Delta T}{T}|_{100\ \mathrm{ps}} - \frac{\Delta T}{T}|_f$ are indicative of the thermal relaxation. The former decreases and the latter increases as heat relaxation time shortens. The above

parameters are conveniently encapsulated in the ratio $r = \frac{\frac{\Delta T}{T}|_{100\ \mathrm{ps}} - \frac{\Delta T}{T}|_f}{\frac{\Delta T}{T}|_i}$. Notably, the ratio increases with increasingly efficient thermal dissipation (i.e. fast thermal relaxation). The ratio proved to be a reliable indicator of thermal relaxation efficiency and of the quality of thermal contact.

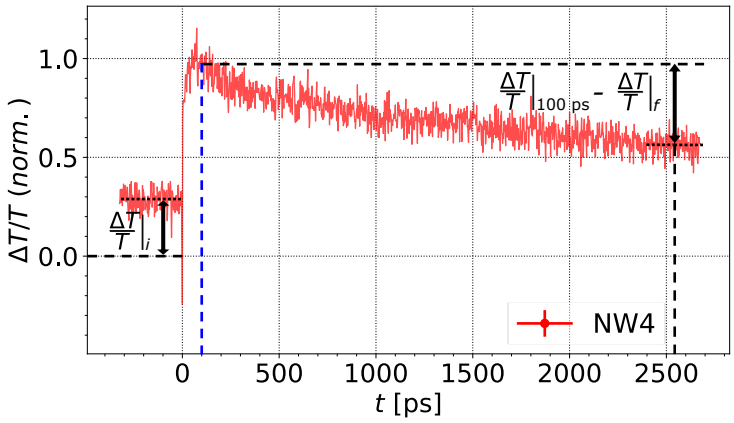

Figure 5.14: Parameters defining the metric of relevance to the investigation of heat transfer. Time-resolved optical signal acquired on NW4: relative transmittivity variation versus delay-time. The signal is normalized against the value obtained at $t \simeq 100$ ps (dashed blue line). The two parameters characterizing the thermal signal are shown (double arrows).

5.4.2 Experimental results

Figure 5.15 summarizes the analysis of the thermal relaxation of individual NWs-S based on the ratio r. Measurements were performed at a pump power of 6 µW, at wavelengths $\lambda_{pump} = 410$ nm and $\lambda_{probe} = 650$ nm, with spot sizes approximately at the diffraction limit, thus of the same order as the NWs' length. Figure 5.15a displays the pump-probe signals obtained for the four NWs-S (see Figure 5.3, Table 5.1), normalized as described in the previous section. Multiple measurements were taken on each NW, and the procedure described in Subsection 5.4.1 was applied to each dataset. The resulting r values were then averaged and are presented in Figure 5.15b. This panel illustrates the parameter r analyzed as a function of the increasing NW-substrate contact length, L_c (see Figure 5.4) relative to the total NW length, L. The case $L/L_c = 100\%$ corresponds to the case of a NW completely supported on PMMA (i.e. NW4). Suspended NWs exhibit low r values, characterized by small $\frac{\Delta T}{T}|_{100\ \mathrm{ps}} - \frac{\Delta T}{T}|_f$ values (indicating slow thermal dissipation) and high $\frac{\Delta T}{T}|_i$ values (indicating significant heat accumulation). In contrast, NWs fully supported on PMMA show high r, with large $\frac{\Delta T}{T}|_{100\ \mathrm{ps}} - \frac{\Delta T}{T}|_f$ and small $\frac{\Delta T}{T}|_i$, indicating rapid thermal dissipation and minimal heat accumulation.

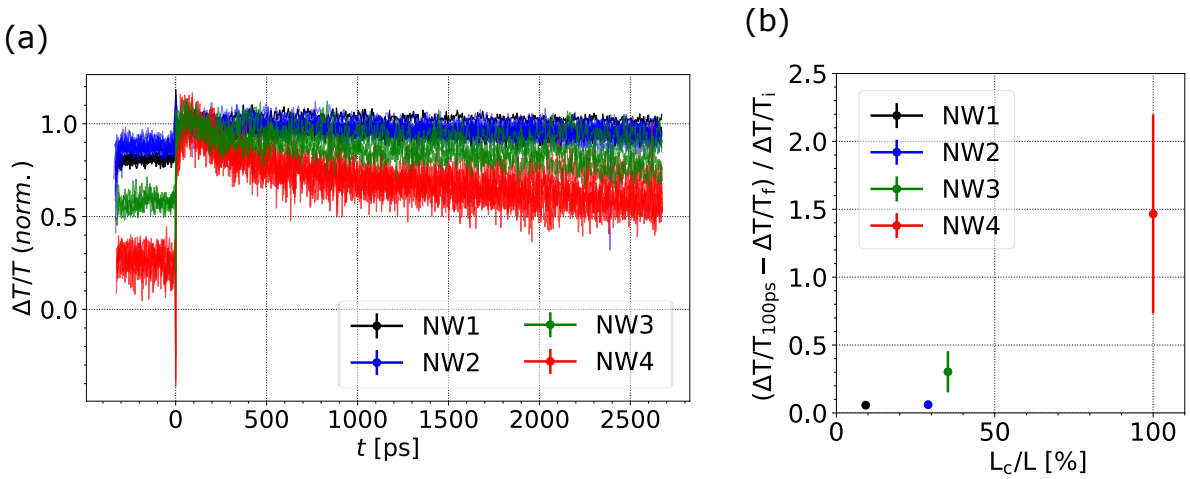

Figure 5.15: Thermal relaxation analysis of individual NWs-S. (a): Pump-probe optical signals normalized at 100 ps (see main text). Pump power 6 μW, $\lambda_{pump} = 410$ nm and $\lambda_{probe} = 650$ nm, light polarization parallel to the NWs axis and beams size of the same order of the NW length. (b) NWs thermal dissipation efficiency is a function of increasing contact ratio: r versus L_c/L .

These results show that **thermal relaxation is strongly influenced by the NW-PMMA substrate contact**. This aligns with the system's geometry: NWs with larger contact areas display more efficient heat dissipation to the substrate. As represented in the schematics in Figure 5.16, neglecting heat transfer to the air, the only dissipation pathway in these systems is provided by the substrate. In particular, for fully supported NWs (i.e. NW4), heat flow perpendicular to the NW-substrate interface, $\mathbf{q}_{perp}$, occurs along the full length of the NW at the interface with the PMMA (panel (a)). In the case of NW3, where the NW is suspended but the contact length L_c remains consistent, heat out of the NW occurs at the extremities, creating a temperature gradient along the NW and an axial heat flow (panel (b)). Thermal transfer in NW1 and NW2 is similar to NW3, nevertheless, the contact at the extremities is reduced and perpendicular heat flow is less efficient (i.e. longer dissipation times), leading to a less efficient thermal relaxation.

To gain further insight, time-resolved traces are displayed in semi-logarithmic scale. This allows to visually compare the decay time among the different signals and to inspect for the onset of multiple decay times. In order to do so, the signals for each NW-S are averaged, after removing the initial offsets, $\frac{\Delta T}{T}|_i$, and then are normalized to their value at $\frac{\Delta T}{T}|_{100\ \mathrm{ps}}$. These averaged signals are displayed in Figure 5.17. NW1 (black line), which is suspended and has the smallest L_c/L, exhibits a linear decay in a semi-logarithmic scale, indicating a mono-exponential behavior of the signal. This is expected when heat transfer is limited by the interface (see Section 1.2.2). Specifically, this occurs when

the NW temperature remains spatially homogeneous (Biot number $Bi < 1$) during the cooling process and the substrate remains isothermal. The decay time in NW1 anyway far exceeds the experimental time-delay window, coherently with a slow relaxation through the small contact area, along with the previous illustrated mechanism (Figure 5.16b, with small L_c values).

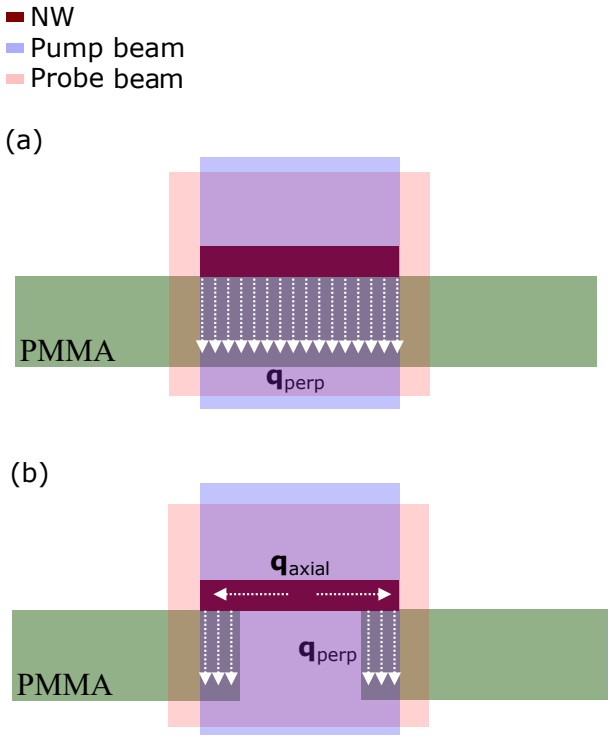

Figure 5.16: Schematics illustrating heat flow pathways for NWs with dimensions matching the pump beam size, in supported (a) and suspended (b) configurations. In the supported case (a), the primary dissipation pathway is provided by the substrate, and axial heat flow is inhibited due to the uniform excitation, leading to a uniform temperature distribution across the NW. In the suspended case (b), heat dissipation occurs at the extremities in contact with the PMMA, resulting in a temperature gradient along the nanostructure, which induces axial heat flow.

When L_c/L increases, the signal deviates from a mono-exponential. The signal can be approximatively described by two decaying time constants (NW3). The onset of two decay times is clearly noticeable for the case of NW4, which is fully supported on PMMA. Assuming the time-resolved signal to be proportional to the NW temperature, as is often the case for a solid nano-object in contact with a solid substrate [105, 107], the deviation from a mono-exponential is ascribed [169] to an increasing temperature of the substrate portion proximal to the nano-object [2]. The short decay time is ascribed to heat transfer

[2]The analytical form of the NW temperature evolution in time is not, mathematically speaking, a

across the interface and the longer decay time to cooling of the nanostructure-proximal substrate ensemble towards the substrate bulk. The substrate peak temperature increase is maximum in the case of NW4, since the heat flux to the substrate is 1D (perpendicular to NW along most of the NW, except beneath the NW edges). This is in contrast with the case of NW2 and NW3, where, due the limited contact size, the dissipation to the substrate is 3D (not depicted in Figure 5.16), since heat flows also sideways in the substrate, hence enhancing cooling of the substrate portion in contact with the NW. The temperature increase of the substrate is thus higher in the case of NW4, this is the reason for the clearer presence of two decay times in its pump and probe signal.

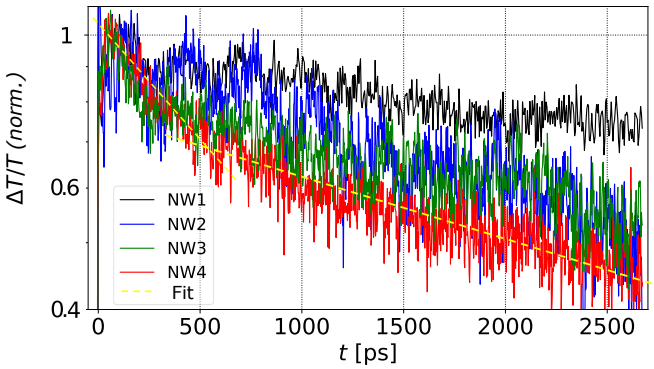

Figure 5.17: Heat dissipation timescales in NWs-S. Time-resolved signals in semi-log scale obtained from the averaged traces (refer to main text for details). Linear fits (dashed yellow lines) to the signal from NW4. The experimental conditions are the same as reported in Figure 5.15.

A similar trend for all four NWs is observed at higher pump powers, although with more scattered r values (not reported in the manuscript). This is likely due to PMMA modifications, triggered by laser energy absorption occurring at 410 nm [170, 171]. Indeed, PMMA can absorb energy under intense UV illumination, eventually yielding to PMMA modifications. While negligible at low power, at higher powers, direct absorption does impact the sample, modifying its signal behavior. After performing high-power measurements, the damage is visible under an optical microscope. These measurements have been excluded from further discussion in this work.

Furthermore, an extended study was conducted to investigate the thermal properties of NWs-L, in suspended, PMMA-supported and sapphire-supported NWs. However, this series of measurements proved inconclusive. The decay times were consistently very long

sum of exponentials. Nevertheless, what ever the correct analytical formula, it is well fitted as such. A fit in terms of multiple exponentials allows to easily inspect for the presetn of multiple relaation times.

across all configurations, potentially indicating poor-quality contact with the interfaces. These configurations require further investigation and are therefore not discussed here.

5.4.3 Thermal boundary conductance: InAs NW-PMMA

Pump-probe measurements , presented in the previous section, provide insights into the thermal conductance at the InAs-PMMA interface. In fact, the dissipation times extracted from pump-probe signals enable, under certain assumptions, an estimation of interface thermal conductance, leveraging the theoretical model described in Section 1.2.2.

In the instance of NW4, which fully adheres to PMMA, the similar sizes of the pump spot diameter and NW length allow for the investigation of energy transfer at the interface, avoiding the influence of heat diffusion along the NW's axis.

The bi-exponential decay in the relaxation behaviour yields a first decay time $\tau \sim 1.4$ ns. This value is used to estimate an interface thermal conductance $G \sim 83$ MW/m^{2}K, via Equation 1.27. The volumetric specific heat for InAs, $C = 1.4 \cdot 10^6$ J/K·m^3, is used in this estimate. The volume-to-contact-surface ratio, $\frac{V}{S_C}$, is calculated by modeling the NW as a hexagonal prism with a facet in contact with the substrate. Here, R represents the circumradius of the regular hexagonal cross-section, defined as the distance from the center to a vertex:

$$\frac{V}{S_C} = \frac{3\sqrt{3}}{2}R$$

The value of R is derived from the SEM images as half of the apparent diameter of the cylindrical shape (i.e. $R = D/2$ from Table 5.1).

The model used here relies on two assumptions: (i) the NW remains isothermal during thermal relaxation, and (ii) the substrate proximal to the interface evacuates heat to the bull substrates on time scales longer than τ. Ansatz (i) is supported by a Biot number $Bi = \frac{l/k}{R_K} = 0.4 < 1$, calculated using the radial dimension $l = R$, the bulk thermal conductivity of InAs $k_{InAs} = 27$ W/m·K, and the estimated interface thermal conductance G, being $R_K = 1/G$. This confirms that heat transfer through the interface is less efficient than radial diffusion across the NW cross-section. Ansatz (ii), besides being supported by the two dashed lines in Figure 5.17, seems reasonable for PMMA, which has low thermal conductivity ($k = 0.167 \div 0.25$ W/m·K) and thermal diffusivity ($\alpha \sim 0.11 \cdot 10^{-6}$ m^2/s).

5.5 Conclusions and Perspectives

The investigation of individual InAs NWs by US allowed to observe both radial and longitudinal modes on individual NWs suspended over a trench, identifying the breathing

and extensional modes and correlating them to the NW's morphology. This allowed to benchmark the stiffness matrix of WZ InAs NW against displacement dynamics occurring both in the radial and longitudinal directions of the NW. The investigation of suspended and substrate-supported NWs allowed to quantify the extrinsic and intrinsic attenuation times for the NW breathing modes in the hypersonic frequency range. Extrinsic damping was shown to be the dominant dissipative channel. This work sheds new light on the acoustics of InAs NWs. These aspects are relevant for engineering nanoscale nanomechanical systems based on NWs such as mechanical resonators operating in the GHz range and high-sensitivity mass sensors.

A new metric was developed to recover from pump and probe traces, affected by repeatability issues and high noise levels, the features that underline the thermal response in NWs. The thermal behaviour of suspended and PMMA-supported NWs of various types was investigated. The contact with the substrate plays a dominant role in the thermal dynamics compared to the diffusion within the NW itself. The thermal conductance at the NW-PMMA interface was estimated to be $G \sim 83$ MW/m^2 K. These findings pave the way to the exploitation of time-resolved all-optical optical nanoscopy as a tool for non-destructive testing at the nanoscale, beyond the case of model systems. Specifically, this work set the benchmark for (i) the inspection of the contact between a nano-object and its surroundings; (ii) the investigation of the cooling dynamics of the nano-object to the supporting substrate; and (iii) the assessment of the interface thermal boundary conductances.

Conclusions and outlook

This thesis presents a comprehensive optical investigation of energy transfer processes in MoS_2 NTs and InAs NWs, considering varying geometrical features (diameters and lengths) and diverse spatial configurations, including nanostructures suspended over trenches, PMMA-supported and sapphire-supported. The work systematically addresses every stage of the research, encompassing theoretical predictions, the requirements for ultrafast and spatially-resolved optical techniques, the engineering of a fabrication protocol, and the implementation of optical methods to investigate energy flow within and outside high aspect-ratio nanostructures.

In Chapter 2, the working principles underlying the optical techniques used to investigate the linear and time-resolved optical properties of high aspect-ratio semiconducting nanostructures are described. Additionally, the development and optimization of the experimental setups for these specific purposes are detailed.

In Chapter 3, the synthesis methods for growing MoS_2 NTs and InAs NWs investigated in this work are detailed, along with the fabrication protocol specifically developed to obtain high-aspect-ratio nanostructures suspended over trenches. These architectures are tailored for ultrafast optical investigations in transmission mode on individual nano-objects. This protocol provides a versatile approach for creating nanostructure-based systems optimized for optical studies in transmission mode across a wide range of wavelengths.

Chapter 4 presents the optical and mechanical properties of MoS_2 NTs with diameters in the range of hundreds of nanometers (120 nm and 225 nm) in the three configurations described earlier. The extinction cross-section per unit length, $\sigma_{L,ext}^{NT}$, was measured using extinction spectroscopy over a broad wavelength range (440–940 nm) and analyzed with respect to polarization effects, substrate influence, and NT diameter. Experimental results revealed a pronounced polarization dependence, with parallel polarization generally yielding higher extinction values. Suspended NTs with a diameter of approximately 120 nm exhibited higher extinction values and more distinct spectral features compared to larger or substrate-supported NTs. Analytical simulations using Mie theory, followed by finite element method (FEM) simulations incorporating realistic geometries, anisotropic

dielectric properties, substrate effects, and laser beam focusing, estimated the extinction cross-section per unit length across the investigated wavelength range, extracting the information on the absorption cross-section per unit length. The scattering contribution was found to dominate at longer wavelengths, while absorption became more pronounced below 700 nm, consistent with the MoS_2 bandgap. The mechanical properties of MoS_2 NTs were investigated using ultrafast time-resolved spectroscopy. Analyses focused on different time windows after the excitation and detected radial vibrational eigenmodes corresponding to the fundamental breathing and thickness modes. An approximated model for thickness vibrations enabled the estimation of the NT shell thickness, $h \simeq 16$ nm, from the measured vibrational period. This value of h was instrumental in estimating theoretical values for breathing mode periods, which were found to align well with experimental observations, thereby validating the assumptions made for the elastic coefficients used in the models. These findings provide significant insights into the structure, optical response, and mechanical properties of MoS_2 NTs, despite the challenges posed by their anisotropic nature and complex morphologies.

Chapter 5 explores the mechanical and thermal properties of InAs NWs, focusing on the mechanisms activated by impulsive excitations with short laser pulses, via Ultrafast time-resolved spectroscopy. NWs of various sizes were studied, both isolated and in contact with PMMA. On the mechanical side, the fundamental frequencies of the breathing and longitudinal vibrational modes were determined by combining experimental dispersion relations (oscillation period versus NW size) with analytical and numerical models. Experimental results validated the stiffness coefficients governing longitudinal and radial displacements in WZ InAs NWs. The mechanical attenuation of breathing modes was also explored, demonstrating that extrinsic attenuation is the dominant dissipation mechanism in InAs NWs, outweighing intrinsic losses. These findings enable precise mechanical characterization of individual NWs, overcoming the averaging limitations of ensemble measurements, and provide critical insights for applications such as nanoscale sensors and optomechanical systems.

On the thermal side, qualitative insights into InAs NWs' thermal properties were obtained. A novel method was developed to extract stable, meaningful parameters from noisy thermal signals, which are otherwise challenging to analyze using standard approaches. The key parameter, r, was introduced and employed to study thermal relaxation in various systems. Thermal relaxation through the InAs-PMMA interface yielded an estimated interface thermal conductance $G \sim 83$ MW/m$^2\cdot$ K. These results provide preliminary insights into thermal relaxation mechanisms within technologically relevant systems.

To conclude, this work demonstrates that time-resolved optical spectromicroscopy serves as a powerful, non-destructive tool for probing the thermomechanical properties and morphologies of nanomaterials. The findings presented in this thesis open new avenues for exploring the mechanisms that govern energy transfer in nanostructures and their surrounding environments.

Bibliography

[1] David G Cahill et al. "Nanoscale thermal transport". In: *Journal of applied physics* 93.2 (2003), pp. 793–818.

[2] David G Cahill et al. "Nanoscale thermal transport. II. 2003–2012". In: *Applied physics reviews* 1.1 (2014).

[3] Austin J Minnich et al. "Thermal conductivity spectroscopy technique to measure phonon mean free paths". In: *Physical review letters* 107.9 (2011), p. 095901.

[4] Herbert Gleiter. "Nanostructured materials: basic concepts and microstructure". In: *Acta materialia* 48.1 (2000), pp. 1–29.

[5] Eric Pop. "Energy dissipation and transport in nanoscale devices". In: *Nano Research* 3 (2010), pp. 147–169.

[6] Matthias Imboden and Pritiraj Mohanty. "Dissipation in nanoelectromechanical systems". In: *Physics Reports* 534.3 (2014), pp. 89–146.

[7] Zhong Lin Wang and Jinhui Song. "Piezoelectric nanogenerators based on zinc oxide nanowire arrays". In: *Science* 312.5771 (2006), pp. 242–246.

[8] Xiaohua Huang et al. "Plasmonic photothermal therapy (PPTT) using gold nanoparticles". In: *Lasers in medical science* 23 (2008), pp. 217–228.

[9] Gordon E Moore. "Cramming more components onto integrated circuits". In: *Proceedings of the IEEE* 86.1 (1998), pp. 82–85.

[10] R Agrawal, O Loh, and HD Espinosa. "The evolving role of experimental mechanics in 1-D nanostructure-based device development". In: *Experimental mechanics* 51 (2011), pp. 1–9.

[11] Ravi Agrawal et al. "Elasticity size effects in ZnO nanowires- a combined experimental-computational approach". In: *Nano letters* 8.11 (2008), pp. 3668–3674.

[12] KL Ekinci and ML Roukes. "Nanoelectromechanical systems". In: *Review of scientific instruments* 76.6 (2005).

[13] Minhang Bao and Heng Yang. "Squeeze film air damping in MEMS". In: *Sensors and Actuators A: Physical* 136.1 (2007), pp. 3–27.

[14] Harold G Craighead. "Nanoelectromechanical systems". In: *Science* 290.5496 (2000), pp. 1532–1535.

[15] Silvan Schmid et al. "Damping mechanisms in high-Q micro and nanomechanical string resonators". In: *Physical Review B-Condensed Matter and Materials Physics* 84.16 (2011), p. 165307.

[16] Yunhua Huang, Xuedong Bai, and Yue Zhang. "In situ mechanical properties of individual ZnO nanowires and the mass measurement of nanoparticles". In: *Journal of Physics: Condensed Matter* 18.15 (2006), p. L179.

[17] Eduardo Gil-Santos et al. "Nanomechanical mass sensing and stiffness spectrometry based on two-dimensional vibrations of resonant nanowires". In: *Nature nanotechnology* 5.9 (2010), pp. 641–645.

[18] Giulio Benetti et al. "Photoacoustic sensing of trapped fluids in nanoporous thin films: device engineering and sensing scheme". In: *ACS applied materials & interfaces* 10.33 (2018), pp. 27947–27954.

[19] Marco Travagliati et al. "Interface nano-confined acoustic waves in polymeric surface phononic crystals". In: *Applied Physics Letters* 106.2 (2015).

[20] Kostya S Novoselov et al. "Two-dimensional atomic crystals". In: *Proceedings of the National Academy of Sciences* 102.30 (2005), pp. 10451–10453.

[21] Khairul Alam and Roger K Lake. "Monolayer MoS_2 Transistors Beyond the Technology Road Map". In: *IEEE transactions on electron devices* 59.12 (2012), pp. 3250–3254.

[22] La Li, Chuqiao Hu, and Guozhen Shen. "Low-dimensional nanostructure based flexible photodetectors: device configuration, functional design, integration, and applications". In: *Accounts of Materials Research* 2.10 (2021), pp. 954–965.

[23] J Theerthagiri et al. "Recent advances in MoS_2 nanostructured materials for energy and environmental applications–a review". In: *Journal of Solid State Chemistry* 252 (2017), pp. 43–71.

[24] Intek Song, Chibeom Park, and Hee Cheul Choi. "Synthesis and properties of molybdenum disulphide: from bulk to atomic layers". In: *Rsc Advances* 5.10 (2015), pp. 7495–7514.

[25] Y Feldman et al. "High-rate, gas-phase growth of MoS_2 nested inorganic fullerenes and nanotubes". In: *Science* 267.5195 (1995), pp. 222–225.

[26] Maja Remškar. "Inorganic nanotubes". In: *Advanced Materials* 16.17 (2004), pp. 1497–1504.

[27] Pallellappa Chithaiah et al. "Solving the "MoS_2 nanotubes" synthetic enigma and elucidating the route for their catalyst-free and scalable production". In: *ACS nano* 14.3 (2020), pp. 3004–3016.

[28] Sudarson S Sinha et al. "MoS_2 and WS_2 nanotubes: Synthesis, structural elucidation, and optical characterization". In: *The Journal of Physical Chemistry C* 125.11 (2021), pp. 6324–6340.

[29] Lena Yadgarov and Reshef Tenne. "Nanotubes from Transition Metal Dichalcogenides: Recent Progress in the Synthesis, Characterization and Electrooptical Properties". In: *Small* (2024), p. 2400503.

[30] AI Galimov et al. "Direct observation of split-mode exciton-polaritons in a single MoS 2 nanotube". In: *Nanoscale Horizons* (2024).

[31] M Strojnik et al. "MoS_2 nanotube field effect transistors". In: *AIP Advances* 4.9 (2014).

[32] Sara Fathipour et al. "Synthesized multiwall MoS_2 nanotube and nanoribbon field-effect transistors". In: *Applied Physics Letters* 106.2 (2015).

[33] Naoya Shiraiwa et al. "Fabrication and characterization of field-effect transistors based on MoS_2 nanotubes prepared in anodic aluminum oxide templates". In: *Micro and Nano Engineering* 19 (2023), p. 100200.

[34] DR Kazanov et al. "Multiwall MoS_2 tubes as optical resonators". In: *Applied Physics Letters* 113.10 (2018).

[35] Dmitrii Kazanov et al. "Towards exciton-polaritons in an individual MoS_2 nanotube". In: *Nanomaterials* 10.2 (2020), p. 373.

[36] Ilya A Eliseyev et al. "Twisted nanotubes of transition metal dichalcogenides with split optical modes for tunable radiated light resonators". In: *Advanced Optical Materials* 11.15 (2023), p. 2202782.

[37] Qingkai Qian et al. "Chirality-dependent second harmonic generation of MoS_2 nanoscroll with enhanced efficiency". In: *ACS nano* 14.10 (2020), pp. 13333–13342.

[38] Aniello Pelella et al. "WS_2 Nanotube Transistor for Photodetection and Optoelectronic Memory Applications". In: *Small* (2024), p. 2403965.

[39] Sikandar Aftab, Muhammad Zahir Iqbal, and You Seung Rim. "Recent advances in rolling 2D TMDs nanosheets into 1D TMDs nanotubes/nanoscrolls". In: *Small* 19.1 (2023), p. 2205418.

[40] Chaoying Zhang et al. "High-performance photodetectors for visible and near-infrared lights based on individual WS_2 nanotubes". In: *Applied physics letters* 100.24 (2012).

[41] Rudooh S Wagner and W Chadwick Ellis. "Vapor-liquid-solid mechanism of single crystal growth". In: *Applied physics letters* 4.5 (1964), pp. 89–90.

[42] Enrique Barrigón et al. "Synthesis and applications of III–V nanowires". In: *Chemical reviews* 119.15 (2019), pp. 9170–9220.

[43] Xiangfeng Duan et al. "Indium phosphide nanowires as building blocks for nanoscale electronic and optoelectronic devices". In: *nature* 409.6816 (2001), pp. 66–69.

[44] Miquel Royo et al. "A review on III–V core–multishell nanowires: growth, properties, and applications". In: *Journal of Physics D: Applied Physics* 50.14 (2017), p. 143001.

[45] Ruoxue Yan, Daniel Gargas, and Peidong Yang. "Nanowire photonics". In: *Nature photonics* 3.10 (2009), pp. 569–576.

[46] Milo Yaro Swinkels and Ilaria Zardo. "Nanowires for heat conversion". In: *Journal of Physics D: Applied Physics* 51.35 (2018), p. 353001.

[47] Domenic Prete et al. "Thermoelectric conversion at 30 K in InAs/InP nanowire quantum dots". In: *Nano letters* 19.5 (2019), pp. 3033–3039.

[48] Shadi A Dayeh et al. "High electron mobility InAs nanowire field-effect transistors". In: *small* 3.2 (2007), pp. 326–332.

[49] Anil W Dey et al. "High-performance inas nanowire mosfets". In: *IEEE Electron Device Letters* 33.6 (2012), pp. 791–793.

[50] Miriam S Vitiello et al. "Room-temperature terahertz detectors based on semiconductor nanowire field-effect transistors". In: *Nano letters* 12.1 (2012), pp. 96–101.

[51] Sofia Johansson et al. "RF characterization of vertical InAs nanowire wrap-gate transistors integrated on Si substrates". In: *Sensor Transactions on Microwave Theory and Techniques* 59.10 (2011), pp. 2733–2738.

[52] Tomotaka Tanaka et al. "Vertical surrounding gate transistors using single InAs nanowires grown on Si substrates". In: *Applied physics express* 3.2 (2010), p. 025003.

[53] Domenic Prete et al. "Impact of electrostatic doping on carrier concentration and mobility in InAs nanowires". In: *Nanotechnology* 32.14 (2021), p. 145204.

[54] Toshitake Takahashi et al. “Parallel array InAs nanowire transistors for mechanically bendable, ultrahigh frequency electronics”. In: *ACS nano* 4.10 (2010), pp. 5855–5860.

[55] Wei Lu, Ping Xie, and Charles M Lieber. “Nanowire transistor performance limits and applications”. In: *IEEE transactions on Electron Devices* 55.11 (2008), pp. 2859–2876.

[56] Daya S Dhungana et al. “Insight of surface treatments for CMOS compatibility of InAs nanowires”. In: *Nano Research* 12 (2019), pp. 581–586.

[57] Francesco Conzatti et al. “Strain-induced performance improvements in InAs nanowire tunnel FETs”. In: *IEEE transactions on electron devices* 59.8 (2012), pp. 2085–2092.

[58] Khairul Alam. “Uniaxial stress-modulated electronic properties of a free-standing InAs nanowire”. In: *IEEE transactions on electron devices* 59.3 (2011), pp. 661–665.

[59] Lunjie Zeng et al. “Correlation between electrical transport and nanoscale strain in InAs/In0. 6Ga0. 4As core–shell nanowires”. In: *Nano Letters* 18.8 (2018), pp. 4949–4956.

[60] Juan Du et al. “InAs nanowire transistors as gas sensor and the response mechanism”. In: *Nano letters* 9.12 (2009), pp. 4348–4351.

[61] Peter Offermans, Mercedes Crego-Calama, and Sywert H Brongersma. “Gas detection with vertical InAs nanowire arrays”. In: *Nano letters* 10.7 (2010), pp. 2412–2415.

[62] Valeria Demontis et al. “Conductometric sensing with individual InAs nanowires”. In: *Sensors* 19.13 (2019), p. 2994.

[63] Dong Liang, Mohammed R Sakr, and Xuan PA Gao. “One-dimensional weak localization of electrons in a single InAs nanowire”. In: *Nano Letters* 9.4 (2009), pp. 1709–1712.

[64] Ch Blömers et al. “Electronic phase coherence in InAs nanowires”. In: *Nano letters* 11.9 (2011), pp. 3550–3556.

[65] Simon Abay et al. “High critical-current superconductor-InAs nanowire-superconductor junctions”. In: *Nano letters* 12.11 (2012), pp. 5622–5625.

[66] Eva AA Pogna et al. “Unveiling the detection dynamics of semiconductor nanowire photodetectors by terahertz near-field nanoscopy”. In: *Light: Science & Applications* 9.1 (2020), p. 189.

[67] Wei Wei et al. "Direct heteroepitaxy of vertical InAs nanowires on Si substrates for broad band photovoltaics and photodetection". In: *Nano letters* 9.8 (2009), pp. 2926–2934.

[68] VJ Logeeswaran et al. "A perspective on nanowire photodetectors: current status, future challenges, and opportunities". In: *IEEE Journal of selected topics in quantum electronics* 17.4 (2011), pp. 1002–1032.

[69] Jinshui Miao et al. "Single InAs nanowire room-temperature near-infrared photodetectors". In: *ACS nano* 8.4 (2014), pp. 3628–3635.

[70] Johanna Lieb et al. "Ionic-Liquid Gating of InAs Nanowire-Based Field-Effect Transistors". In: *Advanced Functional Materials* 29.3 (2019), p. 1804378.

[71] Domenic Prete et al. "Heat-Driven Iontronic Nanotransistors". In: *Advanced Science* 10.7 (2023), p. 2204120.

[72] Domenic Prete et al. "Electrostatic control of the thermoelectric figure of merit in ion-gated nanotransistors". In: *Advanced Functional Materials* 31.37 (2021), p. 2104175.

[73] Mirko Rocci et al. "Suspended InAs Nanowire-Based Devices for Thermal Conductivity Measurement Using the 3 ω Method". In: *Journal of Materials Engineering and Performance* 27.12 (2018), pp. 6299–6305.

[74] Lorenzo Peri et al. "Giant reduction of thermal conductivity and enhancement of thermoelectric performance in twinning superlattice InAsSb nanowires". In: *Nano Energy* 103 (2022), p. 107700.

[75] Shiliang Wang, Zhiwei Shan, and Han Huang. "The mechanical properties of nanowires". In: *Advanced Science* 4.4 (2017), p. 1600332.

[76] Yong Zhu. "Mechanics of crystalline nanowires: an experimental perspective". In: *Applied Mechanics Reviews* 69.1 (2017), p. 010802.

[77] Mohammad Nasr Esfahani and Burhanettin Erdem Alaca. "A review on size-dependent mechanical properties of nanowires". In: *Advanced Engineering Materials* 21.8 (2019), p. 1900192.

[78] Yujie Chen, Xianghai An, and Xiaozhou Liao. "Mechanical behaviors of nanowires". In: *Applied Physics Reviews* 4.3 (2017).

[79] Monica Lexholm et al. "Optical determination of Young's modulus of InAs nanowires". In: *Applied Physics Letters* 95.11 (2009).

[80] Róbert Erdélyi et al. "In-situ mechanical characterization of wurtzite InAs nanowires". In: *Solid state communications* 152.19 (2012), pp. 1829–1833.

[81] X Li et al. “Mechanical properties of individual InAs nanowires studied by tensile tests”. In: *Applied Physics Letters* 104.10 (2014).

[82] Cláudia L Dos Santos and Paulo Piquini. “Diameter dependence of mechanical, electronic, and structural properties of InAs and InP nanowires: A first-principles study”. In: *Physical Review B—Condensed Matter and Materials Physics* 81.7 (2010), p. 075408.

[83] Luana Campagnolo Bassotto, Ivana Zanella da Silva, and Cláudia Lange dos Santos. “The role of the surface passivation in the mechanical properties of wurtzite InAs and InP nanowires: first-principles calculations”. In: *The European Physical Journal Plus* 137.10 (2022), p. 1113.

[84] Nupur Gupta et al. “Temperature-dependent electron mobility in InAs nanowires”. In: *Nanotechnology* 24.22 (2013), p. 225202.

[85] Volker Schmidt et al. “Using the Seebeck coefficient to determine charge carrier concentration, mobility, and relaxation time in InAs nanowires”. In: *Applied Physics Letters* 104.1 (2014).

[86] Feng Zhou et al. “Thermal conductivity of indium arsenide nanowires with wurtzite and zinc blende phases”. In: *Physical Review B—Condensed Matter and Materials Physics* 83.20 (2011), p. 205416.

[87] Pinyun Ren et al. “Synthesis and diameter-dependent thermal conductivity of InAs nanowires”. In: *Nano-Micro Letters* 6 (2014), pp. 301–306.

[88] Wu-Xing Zhou et al. “Phonon thermal transport in InAs nanowires with different size and growth directions”. In: *Physics Letters A* 377.43 (2013), pp. 3144–3147.

[89] Carsten Weber et al. “Probing confined phonon modes by transport through a nanowire double quantum dot”. In: *Physical review letters* 104.3 (2010), p. 036801.

[90] Ann I Persson et al. “Thermal conductance of InAs nanowire composites”. In: *Nano letters* 9.12 (2009), pp. 4484–4488.

[91] Eric Thomas Swartz. *Solid-solid thermal boundary resistance*. Cornell University, 1987.

[92] Damiano Nardi et al. “Probing thermomechanics at the nanoscale: impulsively excited pseudosurface acoustic waves in hypersonic phononic crystals”. In: *Nano letters* 11.10 (2011), pp. 4126–4133.

[93] Pierre-Adrien Mante, Laurent Belliard, and Bernard Perrin. “Acoustic phonons in nanowires probed by ultrafast pump-probe spectroscopy”. In: *Nanophotonics* 7.11 (2018), pp. 1759–1780.

[94] Alexandre A Kolomenskii et al. "Observation of coherent acoustic and optical phonons in bismuth nanowires by a femtosecond pump-probe technique". In: *Journal of Applied Physics* 104.10 (2008).

[95] Vincent Juvé et al. "Probing elasticity at the nanoscale: terahertz acoustic vibration of small metal nanoparticles". In: *Nano letters* 10.5 (2010), pp. 1853–1858.

[96] Damiano Nardi et al. "Impulsively excited surface phononic crystals: a route toward novel sensing schemes". In: *IEEE Sensors Journal* 15.9 (2015), pp. 5142–5150.

[97] Claudio Giannetti et al. "Thermomechanical behavior of surface acoustic waves in ordered arrays of nanodisks studied by near-infrared pump-probe diffraction experiments". In: *Physical Review B—Condensed Matter and Materials Physics* 76.12 (2007), p. 125413.

[98] Claudio Giannetti et al. "Ultrafast laser pulses to detect and generate fast thermomechanical transients in matter". In: *IEEE Photonics Journal* 1.1 (2009), pp. 21–32.

[99] Simone Peli et al. "Mechanical properties of Ag nanoparticle thin films synthesized by supersonic cluster beam deposition". In: *The Journal of Physical Chemistry C* 120.8 (2016), pp. 4673–4681.

[100] Simone Peli et al. "Simplifying asynchronous optical sampling: an experimental approach toward industrial integration exploiting lock-in acquisition". In: *Applied Optics* 63.23 (2024), pp. 6086–6096.

[101] Emma EM Cating et al. "Imaging spatial variations in the dissipation and transport of thermal energy within individual silicon nanowires using ultrafast microscopy". In: *Nano Letters* 16.1 (2016), pp. 434–439.

[102] Erika M Van Goethem et al. "Observation of phonon propagation in germanium nanowires using femtosecond pump–probe microscopy". In: *ACS Photonics* 6.9 (2019), pp. 2213–2222.

[103] Vincent Juvé et al. "Cooling dynamics and thermal interface resistance of glass-embedded metal nanoparticles". In: *Physical Review B—Condensed Matter and Materials Physics* 80.19 (2009), p. 195406.

[104] Francesco Banfi et al. "Temperature dependence of the thermal boundary resistivity of glass-embedded metal nanoparticles". In: *Applied Physics Letters* 100.1 (2012).

[105] Tatjana Stoll et al. “Time-resolved investigations of the cooling dynamics of metal nanoparticles: impact of environment”. In: *The Journal of Physical Chemistry C* 119.22 (2015), pp. 12757–12764.

[106] Jie Zhu et al. “The ultrafast laser pump-probe technique for thermal characterization of materials with micro/nanostructures”. In: *Nanoscale and Microscale Thermophysical Engineering* 21.3 (2017), pp. 177–198.

[107] Marco Gandolfi et al. “Ultrafast thermo-optical dynamics of plasmonic nanoparticles”. In: *The Journal of Physical Chemistry C* 122.15 (2018), pp. 8655–8666.

[108] Lukas Wittenbecher et al. “Unraveling the ultrafast hot electron dynamics in semiconductor nanowires”. In: *ACS nano* 15.1 (2021), pp. 1133–1144.

[109] Tatjana Stoll et al. “Advances in femto-nano-optics: ultrafast nonlinearity of metal nanoparticles”. In: *The European Physical Journal B* 87 (2014), pp. 1–19.

[110] Christophe Voisin et al. *Ultrafast electron dynamics and optical nonlinearities in metal nanoparticles*. 2001.

[111] Alessandro Casto et al. “Experimental optical retrieval of the Thermal Boundary Resistance of carbon nanotubes in water”. In: *Carbon* 229 (2024), p. 119445.

[112] Arnaud Arbouet et al. “Direct measurement of the single-metal-cluster optical absorption”. In: *Physical review letters* 93.12 (2004), p. 127401.

[113] Jean-Christophe Blancon et al. “Direct measurement of the absolute absorption spectrum of individual semiconducting single-wall carbon nanotubes”. In: *Nature communications* 4.1 (2013), p. 2542.

[114] Aurélien Crut et al. “Optical absorption and scattering spectroscopies of single nano-objects”. In: *Chemical Society Reviews* 43.11 (2014), pp. 3921–3956.

[115] Aurélien Crut et al. “Linear and ultrafast nonlinear plasmonics of single nano-objects”. In: *Journal of Physics: Condensed Matter* 29.12 (2017), p. 123002.

[116] H Baida et al. “Ultrafast Nonlinear Optical Response of a Single Gold Nanorod near Its Surface Plasmon Resonance”. In: *Physical review letters* 107.5 (2011), p. 057402.

[117] Ferran Pujol-Vila et al. “Soft optomechanical systems for sensing, modulation, and actuation”. In: *Advanced Functional Materials* 33.14 (2023), p. 2213109.

[118] Tomi Koskinen et al. “Thermoelectric characteristics of InAs nanowire networks directly grown on flexible plastic substrates”. In: *ACS Applied Energy Materials* 4.12 (2021), pp. 14727–14734.

[119] PeterY Yu. *Fundamentals of semiconductors*. Springer, 2005.

[120] Giuseppe Grosso and Giuseppe Pastori Parravicini. *Solid state physics*. Academic press, 2013.

[121] Allen E Fuhs. "Absorption and Scattering of Light by Small Particles, by Craig F. Bohren and Donald R. Huffman". In: *Optics & Photonics News* 9.11 (1998), p. 43.

[122] Etienne Pertreux. "Spectroscopie optique de nano-objets individuels: effets d'environnement, de forme et d'orientation". PhD thesis. Université Claude Bernard-Lyon I, 2015.

[123] Pascal Ruello and Vitalyi E Gusev. "Physical mechanisms of coherent acoustic phonons generation by ultrafast laser action". In: *Ultrasonics* 56 (2015), pp. 21–35.

[124] NW Aschroft and ND Mermin. *Solid state physics; 1976, Forth Worth*.

[125] Andrew C Tam. "Applications of photoacoustic sensing techniques". In: *Reviews of Modern Physics* 58.2 (1986), p. 381.

[126] Bertram Alexander Auld. *Acoustic fields and waves in solids*. Ripol Klassik, 1973.

[127] Gregory V Hartland. "Coherent excitation of vibrational modes in metallic nanoparticles". In: *Annu. Rev. Phys. Chem.* 57.1 (2006), pp. 403–430.

[128] Min Hu et al. "Vibrational response of nanorods to ultrafast laser induced heating: theoretical and experimental analysis". In: *Journal of the American Chemical Society* 125.48 (2003), pp. 14925–14933.

[129] Michele Diego et al. "Ultrafast nano generation of acoustic waves in water via a single carbon nanotube". In: *Photoacoustics* 28 (2022), p. 100407.

[130] Daniel Vakulov et al. "Ballistic phonons in ultrathin nanowires". In: *Nano letters* 20.4 (2020), pp. 2703–2709.

[131] Marco Gandolfi et al. "Ultrafast photoacoustic nanometrology of InAs nanowires mechanical properties". In: *The Journal of Physical Chemistry C* 126.14 (2022), pp. 6361–6372.

[132] Tanmoy Maitra, Shigang Zhang, and Manish K Tiwari. "Thermal Transport in Micro-and Nanoscale Systems". In: Springer, 2018.

[133] Eric T Swartz and Robert O Pohl. "Thermal boundary resistance". In: *Reviews of modern physics* 61.3 (1989), p. 605.

[134] J Lombard, François Detcheverry, and Samy Merabia. "Influence of the electron–phonon interfacial conductance on the thermal transport at metal/dielectric interfaces". In: *Journal of Physics: Condensed Matter* 27.1 (2014), p. 015007.

[135] PL Kapitza. "Heat transfer and superfluidity of helium II". In: *Physical Review* 60.4 (1941), p. 354.

[136] Ce-Wen Nan et al. "Effective thermal conductivity of particulate composites with interfacial thermal resistance". In: *Journal of Applied Physics* 81.10 (1997), pp. 6692–6699.

[137] Maxim Nazarenko et al. "A simplified model to estimate thermal resistance between carbon nanotube and sample in scanning thermal microscopy". In: *Journal of Physics D: Applied Physics* 50.49 (2017), p. 494004.

[138] M Necati Özışık. *Heat conduction*. John Wiley & Sons, 1993.

[139] C. R. Carey et al. "Imaging and Absolute Extinction Cross-Section Measurements of Nanorods and Nanowires through Polarization Modulation Microscopy". In: *The Journal of Physical Chemistry C* 114 (2010), pp. 16029–16036. DOI: https://pubs.acs.org/doi/10.1021/jp101891a.

[140] W. E. Moerner and L. Kador. "Optical detection and spectroscopy of single molecules in a solid". In: *Physical Review Letters* 62 (1989), pp. 2535–2538. DOI: https://doi.org/10.1103/PhysRevLett.62.2535.

[141] Romain Rouxel. *Ultrafast thermo-optical dynamics of single plasmonic nanoparticles*. PhD thesis. Université Claude Bernard Lyon 1, 2020.

[142] Clément Panais. *Ultrafast energy transfers at the nanoscale: cooling and vibrational dynamics of single supported metal nano-objects*. PhD thesis. Université Claude Bernard Lyon 1, 2024.

[143] W. T. Tsang. "Chemical beam epitaxy of InP and GaAs". In: *Applied Physics Letters* 45.11 (1984), p. 1234. DOI: 10.1063/1.95075.

[144] Changgu Lee et al. "Anomalous lattice vibrations of single-and few-layer MoS_2". In: *ACS nano* 4.5 (2010), pp. 2695–2700.

[145] R Kiran Kumar Reddy et al. "Hydrothermal approached 1-D molybdenum oxide nanostructures for high-performance supercapacitor application". In: *SN Applied Sciences* 1 (2019), pp. 1–9.

[146] Jl A Wilson and AD Yoffe. "The transition metal dichalcogenides discussion and interpretation of the observed optical, electrical and structural properties". In: *Advances in Physics* 18.73 (1969), pp. 193–335.

[147] Juana Vivó Acrivos et al. “Optical studies of metal-semiconductor transmutations produced by intercalation”. In: *Journal of Physics C: Solid State Physics* 4 (1971), p. L18.

[148] Battulga Munkhbat et al. “Self-hybridized exciton-polaritons in multilayers of transition metal dichalcogenides for efficient light absorption”. In: *Acs Photonics* 6.1 (2018), pp. 139–147.

[149] Battulga Munkhbat et al. “Optical constants of several multilayer transition metal dichalcogenides measured by spectroscopic ellipsometry in the 300–1700 nm range: high index, anisotropy, and hyperbolicity”. In: *ACS photonics* 9.7 (2022), pp. 2398–2407.

[150] Georgy A Ermolaev et al. “Broadband optical properties of monolayer and bulk MoS_2”. In: *npj 2D Materials and Applications* 4.1 (2020), p. 21.

[151] GA Ermolaev et al. “Giant optical anisotropy in transition metal dichalcogenides for next-generation photonics”. In: *Nature communications* 12.1 (2021), p. 854.

[152] Chanyoung Yim et al. “Investigation of the optical properties of MoS_2 thin films using spectroscopic ellipsometry”. In: *Applied Physics Letters* 104.10 (2014).

[153] Dimitrios Christofilos et al. “Optical imaging and absolute absorption cross section measurement of individual nano-objects on opaque substrates: single-wall carbon nanotubes on silicon”. In: *The Journal of Physical Chemistry Letters* 3.9 (2012), pp. 1176–1181.

[154] Fabien Vialla et al. “Universal nonresonant absorption in carbon nanotubes”. In: *Physical Review B* 90.15 (2014), p. 155401.

[155] JL Feldman. “Elastic constants of 2H-MoS_2 and 2H-$NbSe_2$ extracted from measured dispersion curves and linear compressibilities”. In: *Journal of Physics and Chemistry of Solids* 37.12 (1976), pp. 1141–1144.

[156] MR Lovell, MM Khonsari, and RD Marangoni. “A finite element analysis of the frictional forces between a cylindrical bearing element and MoS_2 coated and uncoated surfaces”. In: *Wear* 194.1-2 (1996), pp. 60–70.

[157] Andres Castellanos-Gomez et al. “Elastic properties of freely suspended MoS2 nanosheets”. In: *arXiv preprint arXiv:1202.4439* (2012).

[158] Simon O Mariager et al. “Direct observation of acoustic oscillations in InAs nanowires”. In: *Nano letters* 10.7 (2010), pp. 2461–2465.

[159] Philippe Caroff et al. “Controlled polytypic and twin-plane superlattices in III–V nanowires”. In: *Nature nanotechnology* 4.1 (2009), pp. 50–55.

[160] Dominik Kriegner et al. “Unit cell structure of crystal polytypes in InAs and InSb nanowires”. In: *Nano letters* 11.4 (2011), pp. 1483–1489.

[161] Richard M Martin. “Relation between elastic tensors of wurtzite and zinc-blende structure materials”. In: *Physical Review B* 6.12 (1972), p. 4546.

[162] SQ Wang and HQ Ye. “First-principles study on elastic properties and phase stability of III–V compounds”. In: *Physica status solidi (b)* 240.1 (2003), pp. 45–54.

[163] Yanying Li et al. “Ultrafast electron and phonon response of oriented and diameter-controlled germanium nanowire arrays”. In: *Nano letters* 14.6 (2014), pp. 3427–3431.

[164] Gianluca Rizzi et al. “Analytical model of the acoustic response of nanogranular films adhering to a substrate”. In: *Physical Review B* 104.3 (2021), p. 035416.

[165] Simone Peli et al. “Discrimination of molecular thin films by surface-sensitive time-resolved optical spectroscopy”. In: *Applied Physics Letters* 107.16 (2015).

[166] Simone Peli et al. “Optical and mechanical properties of streptavidin-conjugated gold nanospheres through data mining techniques”. In: *Scientific RepoRtS* 10.1 (2020), p. 16230.

[167] Andrea Ronchi et al. “Discrimination of nano-objects via cluster analysis techniques applied to time-resolved thermo-acoustic microscopy”. In: *Ultrasonics* 114 (2021), p. 106403.

[168] Clément Panais et al. “Cooling dynamics of individual gold nanodisks deposited on thick substrates and nanometric membranes”. In: *The Journal of Physical Chemistry Letters* 14.23 (2023), pp. 5343–5352.

[169] F Banfi et al. “Ab initio thermodynamics calculation of all-optical time-resolved calorimetry of nanosize systems: Evidence of nanosecond decoupling of electron and phonon temperatures”. In: *Physical Review B—Condensed Matter and Materials Physics* 81.15 (2010), p. 155426.

[170] Ahmed Shaker Hussein, Mohammed Hadi Shinen, and Mohammed Sami Abdali. “Study the Effect of Thickness on Optical Properties of Polymer PMMA Thin Films Preparated by Spin Coating Method”. In: *Journal of University of Babylon for Pure and Applied Sciences* 27.4 (2019), pp. 169–177.

[171] Mayra Matamoros-Ambrocio et al. “Synthesis and study of the optical properties of PMMA microspheres and opals”. In: *Polymers* 13.13 (2021), p. 2171.

Acknowledgements

I would like to thank everyone who has contributed to my academic journey. Starting from my thesis supervisors: Francesco Rossella, for orienting me towards this incredible opportunity for my professional career and for his insightful advice; Francesco Banfi and Natalia Del Fatti for warmly welcoming me into their group and for their engagement in guiding me through the world of ultrafast optics, with their support and expertise. I am also grateful to Paolo Maioli for his wise support throughout my time at UCBL. Another thanks goes to Valeria Demontis for guiding me through the world of nanofabrication, and to both Valeria and Domenic Prete, for their support as colleagues and friends. The sincere and collaborative atmosphere they created in our group at SNS permitted me to start this journey in the best way. I extend my thanks to all members of the FemtoNanoOptics group, with whom I shared research time and stimulating discussions. In particular, to Aurélien Crut and Alessandro Casto, for supporting this work with numerical modelling, alongside Marco Gandolfi. To Noëlle Lascoux and Clément Panais for their training in advanced optical setups, and to Fabien Vialla for his fruitful advice.

Finally, I would like to thank the most important people in my life - my family and my love - whose unwavering support and encouragement have been my foundation. They inspire me day by day, by encouraging me to stay strong during the winters, to enjoy the springs and to give my best every day. I am immensely grateful to my parents, to Ayush, to my sisters, and to my nonna Carmela, for their unconditional love and blessing. I dedicate every achievement of my life to them, as well as to my late grandparents, who are always in my heart and thoughts.